Edward Mitchell Bannister,
Approaching Storm (1886), oil on canvas,
102.0 × 152.4 cm.
Smithsonian American Art Museum,
Gift of G. William Miller, 1983.95.62.
Public Domain / Smithsonian Open Access.

MSc Thesis

Atomistic Modelling of Thermophysical and Transport Properties in Lanthanide Chloride Simulants for Molten-Salt Reactors

Course: ME55035 ME-EFPT MSc Thesis

A thesis submitted in fulfilment of the requirements for the degree of

Master of Science

in Mechanical Engineering – Energy and Process Technology

by

Omkar Vijay Dhavale
Student ID: 6051618

Delft University of Technology
Mechanical Engineering

Graduation Committee

This thesis was prepared within the MSc programme in Mechanical Engineering, Energy and Process Technology, at Delft University of Technology.

Student	Omkar Vijay Dhavale
Student ID	6051618
Supervisors	Dr. Anna Louise Smith Reactor Physics and Nuclear Materials, TU Delft Dr. O. Moultos Process and Energy (EFPT), TU Delft
Daily supervisor	Nick ter Veer Reactor Physics and Nuclear Materials, TU Delft

Final graduation committee

Chair	Dr. Othon Moultos
Assessment Committee member	Dr. Anna Louise Smith
Assessment Committee member	Dr. Hüseyin Burak Eral
Expert member	Nick ter Veer
Thesis defence date	21/08/2026

"One of the principal objects of theoretical research … is to find the point of view from which the subject appears in its greatest simplicity."

— J. Willard Gibbs

Preface

This thesis concludes the MSc programme in Mechanical Engineering, Energy and Process Technology, at Delft University of Technology. The work was carried out within the Reactor Institute Delft and investigates molten chloride salts using polarizable-ion molecular dynamics, with particular emphasis on connecting atomistic liquid structure to thermophysical and transport behaviour and on assessing $CeCl_3$- and $NdCl_3$-containing melts as non-radioactive, property-specific analogues of selected UCl_3- and $PuCl_3$-containing systems.

The project developed from binary validation studies of NaCl – $CeCl_3$ and NaCl – $NdCl_3$ to a common analysis of the equal-Ce/Nd NaCl – $CeCl_3$ – $NdCl_3$ composition path. Particular attention was given to statistical convergence, comparison with available experimental and simulation benchmarks, and to distinguishing direct molecular-dynamics observations from fitted or model-derived quantities.

Working on this project provided an opportunity to combine atomistic simulation, thermodynamics, statistical analysis and molten-salt chemistry within a single research problem. The iterative nature of the work—from setting up and validating simulations to interpreting structural, thermophysical and transport trends—also made clear how strongly reliable conclusions depend on careful verification of both the numerical workflow and the underlying physical assumptions.

Omkar Vijay Dhavale
Delft, August 2026

Acknowledgements

I would first like to express my sincere gratitude to Dr. Anna Louise Smith for giving me the opportunity to undertake this thesis project and for welcoming me into the research group. Her initial confidence in me made this work possible, and I am very grateful for her guidance and support throughout the project.

I am deeply grateful to Dr. Othon Moultos for his supervision throughout my thesis. Beyond everything I learned from him scientifically, I particularly appreciate the support and understanding he offered whenever I encountered difficulties outside the purely academic aspects of the project. His guidance, both academic and personal, has meant a great deal to me.

I would also like to thank Nick ter Veer for his continuous day-to-day supervision. Our frequent discussions gave me the opportunity to learn something new almost every day. I especially appreciated his willingness to provide immediate feedback, discuss results as they developed, and patiently work through questions and problems with me. His involvement had a significant influence on both the development of this thesis and my understanding of molecular simulation.

I am grateful to the members of the Reactor Physics and Nuclear Materials group, the Reactor Institute Delft, and Delft University of Technology for providing a stimulating research environment. I also acknowledge the DelftBlue high-performance computing facilities, which provided the computational resources required for the molecular-dynamics simulations performed in this work.

I also acknowledge the use of AI-based tools during this project as practical support for troubleshooting code, visualising complex concepts, and improving the clarity of written drafts.

Finally, I would like to thank my family and friends for their constant encouragement, patience and support throughout my master's studies.

To everyone who contributed, directly or indirectly, to this journey: Thank you.

Summary

Reliable composition- and temperature-dependent properties of molten actinide chlorides are difficult to obtain experimentally, yet they are needed for the analysis of fast-spectrum molten-salt systems. This thesis evaluates whether non-radioactive lanthanide chlorides can provide property-specific model systems for selected U- and Pu-bearing melts and establishes an internally consistent atomistic dataset for the binaries NaCl – $CeCl_3$ and NaCl – $NdCl_3$ and for the equal-Ce/Nd path through NaCl – $CeCl_3$ – $NdCl_3$. Polarizable-ion-model molecular dynamics was performed with MetalWalls at 900, 1000, 1100 and 1200 K using 2000-ion cells. The full binary composition ranges and nine ternary compositions were investigated, giving 124 composition–temperature state points. Density, molar and excess molar volume, heat capacity, excess heat capacity, mixing enthalpy, liquid structure, structural-coherence thermal conductivity and Green–Kubo viscosity were analysed with property-specific convergence and uncertainty checks.

The simulations reproduce the principal binary volumetric trends: density increases with trichloride fraction and decreases with temperature, while molar volume increases with both composition and temperature. The calculated binary excess molar volumes also reproduce the qualitative transition from NaCl-rich expansion to trichloride-rich contraction and show close composition-dependent similarity with the corresponding NaCl – UCl_3 and NaCl – $PuCl_3$ PIM-MD benchmarks. Along the ternary path, total density and molar volume remain close to binary-derived Redlich–Kister–Muggianu representations, whereas the much smaller excess-volume residual shows stronger deviations, indicating that ternary packing cannot be inferred from total volume alone.

The interval-average isobaric heat capacity increases smoothly with trichloride content. For NaCl – $CeCl_3$, it rises from 72.46 ± 0.24 to 141.68 ± 0.53 $\mathrm{J\,mol^{-1}\,K^{-1}}$ between the pure NaCl and pure $CeCl_3$ limits; the corresponding NaCl – $NdCl_3$ range is 72.41 ± 0.25 to 140.81 ± 0.48 $\mathrm{J\,mol^{-1}\,K^{-1}}$. The root-mean-square differences from the supplied NaCl – UCl_3 and NaCl – $PuCl_3$ PIM-MD benchmarks are approximately 0.67 and 0.98 $\mathrm{J\,mol^{-1}\,K^{-1}}$, respectively. Excess heat capacity is slightly negative on the NaCl-rich side and becomes positive at larger trichloride fractions, reaching broad maxima of approximately 5.25 and 5.35 $\mathrm{J\,mol^{-1}\,K^{-1}}$ for the Ce and Nd binaries. These excess values identify where the enthalpic non-ideality is most sensitive to temperature rather than where mixing is necessarily most favourable at one temperature.

Mixing enthalpy provides the clearest limitation of the force field. Direct PIM-MD predicts exothermic mixing in all three systems, with 1100 K minima of approximately -11.24 $\mathrm{kJ\,mol^{-1}}$ for NaCl – $CeCl_3$, -11.71 $\mathrm{kJ\,mol^{-1}}$ for NaCl – $NdCl_3$, and -11.48 $\mathrm{kJ\,mol^{-1}}$ along the ternary path,

all near a total trichloride fraction of 0.4. The binary simulations reproduce the negative sign and broad intermediate-composition minimum observed calorimetrically but are substantially too exothermic. An independently parameterised PMF-informed Molecular Interaction Volume Model retains the correct sign and broad curvature but does not recover the experimental magnitude. Binary benchmark-calibrated MIVM curves reproduce calorimetry more closely because their directional interaction parameters are fitted to those data, and are therefore semi-empirical rather than independent validation. This separates a robust prediction of non-ideal mixing form from a systematic model error in its absolute energetic strength.

The structural analysis provides a common microscopic framework for these composition trends. Ce- and Nd-centred first shells remain distinct, but increasing trichloride content increases chloride sharing and merges finite coordination environments into a connected rare-earth network. Along the equal-Ce/Nd ternary path Ce and Nd form a single mixed chloride-mediated network rather than two spatially independent binary-like subnetworks, while the species-resolved linkage fractions remain close to the 25:50:25 random-pair expectation and do not indicate strong preferential Ce–Nd association. The supplied actinide data show that Nd reproduces the Pu average coordination-number trend particularly closely, while Ce and U display a closely comparable balance of shared-chloride linkage topologies. Simulant fidelity is therefore structural-scale dependent rather than universal.

Transport calculations reinforce both the value and the limits of this structure–property picture. Structural-coherence thermal conductivity shows intermediate-composition minima in both binaries and a flatter ternary response, but the available $NaCl - CeCl_3$ measurements are underpredicted by approximately 60–67% at representative intermediate compositions near 1173 K. These values are consequently treated as model-derived trend estimates, not validated absolute conductivities. The final Green–Kubo viscosity campaign uses exact 5 ns production trajectories throughout and provides broad coverage across all three melts: 40 of 44 Nd states, 42 of 44 Ce states and 34 of 36 ternary states satisfy the adopted reporting protocol. In total, 116 of 124 viscosity state points are therefore reportable after trajectory-length, shifted-window and spectral-sensitivity checks. Across all three systems, viscosity decreases with temperature and increases broadly with trichloride content.

The temporal analyses add a dynamical interpretation without reducing the transport response to one structural lifetime. In Nd-rich $NaCl - NdCl_3$ at 900 K, intermittent Nd–Cl persistence increases from 54.08 to 71.29 ps and Nd–Nd shared-chloride persistence from 79.19 to 115.49 ps between $x(\mathrm{NdCl_3}) = 0.60$ and 1.00, while the topology-switching rate increases from 4.255 to $6.079\ \mathrm{ps^{-1}\,Nd^{-1}}$. The Nd-centred network therefore becomes more recurrent at long times while remaining dynamically labile. In the Ce-rich binary, continuous Ce–Cl and Ce–Ce persistence remains within relatively narrow picosecond ranges rather than increasing monotonically with composition. The final ternary analysis at 900 and 1000 K, evaluated over five non-overlapping 1 ns blocks with a 500 ps maximum lag, likewise finds no exceptional stabilisation of mixed Ce–Cl–Nd bridges and no composition-specific persistence anomaly at $x(\mathrm{LnCl_3}) = 0.80$. Together these observations support a network-relaxation interpretation of the broad viscosity trends while preserving the distinction between structural association and direct causation.

Overall, the work demonstrates that PIM-MD can provide a coherent composition–structure–property description of these lanthanide chloride melts, but its predictive quality is property dependent. The strongest support is obtained for volumetric trends, heat capacity and several structural analogies; mixing enthalpy reveals systematic over-stabilisation, and the structural-coherence thermal-conductivity route is not quantitatively validated by the available Ce measurements. Ce/U and Nd/Pu similarity is therefore best used as a property-specific modelling tool. The ternary results constitute predictions along the investigated equal-Ce/Nd path and show that mixed-lanthanide connectivity can be analysed without assuming either ideal binary interpolation or a unique cooperative Ce–Nd mechanism.

Contents

Preface i

Acknowledgements iii

Summary v

List of Figures xiii

List of Tables xvii

List of Abbreviations and Nomenclature xix

1 Introduction 1

1.1 Background . . . 1
1.2 Research Problem and Knowledge Gap . . . 3
1.3 Research Aim and Objectives . . . 5
1.4 Research Questions . . . 5
1.5 Scope and Thesis Structure . . . 6
1.5.1 Scope of the Study . . . 6
1.5.2 Thesis Structure . . . 7

2 Literature Review 9

2.1 Introduction . . . 9
2.2 Review Scope and Evidence Strategy . . . 10
2.3 Molten Chloride Salts and the Simulant Problem . . . 10
2.3.1 Relevance to Fast-Spectrum Nuclear Systems . . . 10
2.3.2 Why Ce and Nd Are Useful but Non-Universal Analogues . . . 10
2.3.3 Relevance and Limits of the NaCl – $CeCl_3$ – $NdCl_3$ Model System . . . 11
2.4 Polarizable Molecular-Dynamics Evidence for Rare-Earth Chlorides . . . 11
2.5 Structural Evidence and Structure–Property Relationships . . . 12

2.6 Binary Experimental and Computational Evidence . . . 12
2.6.1 $NaCl-NdCl_3$: Stronger Validation Anchor . . . 12
2.6.2 $NaCl-CeCl_3$: Complementary Evidence . . . 13
2.6.3 Property-Specific Ce/U and Nd/Pu Evidence . . . 14
2.7 Evidence for the Target Ternary System . . . 15
2.8 Consolidated Research Gap and Implications for the Present Study . . . 15

3 Theory **17**
3.1 Physical Chemistry of Molten Chloride Salts . . . 17
3.2 Polarizable Ion Model . . . 18
3.2.1 From the Rigid-Ion Model to the Polarizable Ion Model . . . 19
3.2.2 Coulomb Interaction . . . 19
3.2.3 Short-Range Repulsion . . . 19
3.2.4 Dispersion Interaction . . . 20
3.2.5 Induced Dipoles and Polarisation Energy . . . 20
3.2.6 Short-Range Polarisation Damping . . . 21
3.2.7 Parameterisation and Transferability . . . 21
3.3 Thermophysical and Thermodynamic Properties . . . 22
3.3.1 Density and Molar Volume . . . 22
3.3.2 Excess Molar Volume . . . 23
3.3.3 Thermal Expansion . . . 23
3.3.4 Compressibility and Sound Speed . . . 24
3.3.5 Heat Capacity . . . 25
3.3.6 Mixing Enthalpy . . . 25
3.3.7 Excess Heat Capacity . . . 26
3.4 Structural Characterisation . . . 26
3.4.1 Radial Distribution Functions . . . 27
3.4.2 Coordination Numbers and Their Distributions . . . 27
3.4.3 Potential of Mean Force . . . 28
3.4.4 Chloride Sharing and Structural Speciation . . . 29
3.4.5 Temporal Persistence of Structural Motifs . . . 30
3.4.6 Intermediate-Range Order . . . 30
3.5 Transport Properties . . . 30
3.5.1 Shear Viscosity . . . 31
3.5.2 Thermal Conductivity . . . 32

4 Methodology **35**
4.1 Computational Workflow . . . 35

4.2 Simulated Systems and Compositions . . . 35
4.2.1 Composition Definition . . . 36
4.2.2 Composition and State-Point Grids . . . 36
4.3 Molecular-Dynamics Model and Implementation . . . 37
4.3.1 Polarizable Ion Model and Parameterisation . . . 37
4.3.2 Induced Dipoles, Electrostatics and Software . . . 38
4.4 Simulation Protocol . . . 39
4.4.1 Integration Settings and Simulation Stages . . . 39
4.4.2 NPT-to-NVT State Preparation . . . 39
4.4.3 Output Sampling and Run Acceptance . . . 40
4.5 Calculation of Molecular-Dynamics Properties . . . 40
4.5.1 Density . . . 41
4.5.2 Molar Volume . . . 41
4.5.3 Excess Molar Volume . . . 42
4.5.4 Molar Enthalpy and Direct Mixing Enthalpy . . . 43
4.5.5 Isobaric Heat Capacity . . . 44
4.5.6 Excess Isobaric Heat Capacity . . . 44
4.5.7 Radial Distribution Functions, Coordination Numbers and Rare-Earth Speciation . . . 45
4.5.8 Thermal Conductivity from the Structural-Coherence Model . . . 46
4.5.9 Shear Viscosity . . . 47
4.5.10 Temporal Persistence of Chloride-Mediated Connectivity . . . 50
4.6 Thermodynamic Modelling . . . 51
4.6.1 Binary Redlich–Kister Representation . . . 51
4.6.2 PMF-Informed and Benchmark-Calibrated Molecular Interaction Volume Models . . . 51
4.6.3 Composition-Space Representation of Excess Heat Capacity . . . 54
4.7 Statistical Analysis, Uncertainty and Validation . . . 55
4.7.1 Equilibration, Blocking and Mean Properties . . . 55
4.7.2 Derived and Regression-Based Properties . . . 56
4.7.3 Structural and Model-Based Quantities . . . 57
4.7.4 Viscosity Convergence and Uncertainty . . . 58
4.7.5 Reference-Data Matching and Validation Hierarchy . . . 58
4.7.6 Ternary and Simulant Assessment . . . 60

5 Results and Discussion **61**
5.1 Liquid Structure and Network Formation . . . 61
5.1.1 Local Order and Coordination . . . 61

5.1.2 Cluster Formation and Network Polymerisation . . . 65
5.1.3 Shared-Chloride Network Topology . . . 67
5.1.4 Integrated Lanthanide–Actinide Interpretation . . . 69
5.2 Volumetric Properties and Non-Ideal Mixing . . . 70
5.2.1 $NaCl - CeCl_3$ . . . 70
5.2.2 $NaCl - NdCl_3$ . . . 73
5.2.3 $NaCl - CeCl_3 - NdCl_3$ . . . 75
5.3 Heat Capacity and Excess Heat Capacity . . . 79
5.4 Mixing Enthalpy and MIVM Analysis . . . 82
5.5 Thermal Conductivity . . . 87
5.5.1 Binary Melts and Actinide Benchmarks . . . 87
5.5.2 Equal-Ce/Nd $NaCl - CeCl_3 - NdCl_3$ Path . . . 90
5.6 Molten Salt Viscosity . . . 93
5.6.1 Binary $NaCl - NdCl_3$ . . . 93
5.6.2 Binary $NaCl - CeCl_3$ . . . 96
5.6.3 Equal-Ce/Nd $NaCl - CeCl_3 - NdCl_3$ Path . . . 98
5.6.4 Cross-System Synthesis . . . 100

6 Conclusions and Recommendations **101**
6.1 Conclusions . . . 101
6.2 Limitations . . . 105
6.3 Recommendations . . . 106

References **109**

A Supplementary Simulation Information **117**
A.1 Supporting Structural Results . . . 117
A.2 NPT Window and Volume-Property Verification . . . 121
A.3 Heat-Capacity Window Verification . . . 122
A.4 Thermal-Conductivity Sensitivity Verification . . . 123
A.5 Supporting Viscosity Analyses . . . 124
A.5.1 Five-Nanosecond $NaCl - NdCl_3$ Convergence Diagnostics . . . 124
A.5.2 $NaCl–NdCl_3$ Temporal-Persistence Verification at 900 K . . . 125
A.5.3 Five-Nanosecond $NaCl - CeCl_3$ Convergence and Temporal-Persistence Coverage . . . 127
A.5.4 Five-Nanosecond Ternary Viscosity and Persistence Coverage . . . 129

List of Figures

1.1 Selected milestones in the historical development of molten salt reactor technology 2

2.1 Experimental evidence for non-ideal NaCl – $NdCl_3$ behaviour 13
2.2 Assessed NaCl – $NdCl_3$ phase diagram 14

5.1 Composition-dependent radial distribution functions at 1100 K for the two binary melts and the equal-Ce/Nd ternary path. For the ternary system, $x(\mathrm{LnCl_3}) = x(\mathrm{CeCl_3}) + x(\mathrm{NdCl_3})$. 63
5.2 Local coordination in the simulated lanthanide melts and comparison with the actinide PIM-MD results supplied by Ter Veer et al. [79] The binary panels show average first-shell coordination numbers at 1100 K. The ternary heatmaps show the percentage occurrence of individual coordination-number states. 66
5.3 Composition-dependent cluster-size and cluster-composition speciation along the equal-Ce/Nd NaCl – $CeCl_3$ – $NdCl_3$ path at 900–1200 K. Polymers are connected components containing four or more lanthanide ions; cluster compositions are classified as Ce-only, Nd-only or mixed Ce–Nd. 69
5.4 Composition-dependent shared-chloride linkage topology along the equal-Ce/Nd NaCl – $CeCl_3$ – $NdCl_3$ path at 900–1200 K. Corner-, edge- and face/higher-order categories correspond to one, two and three-or-more shared chloride neighbours, respectively. 69
5.5 Absolute volumetric properties of NaCl – $CeCl_3$. PIM–MD density and molar volume are shown over the complete composition and temperature ranges together with the Sato–Yamamura descriptions compiled by Iwadate [31]. 71
5.6 Excess molar volume of NaCl – $CeCl_3$ and NaCl – UCl_3 72
5.7 Absolute volumetric properties of NaCl – $NdCl_3$. PIM–MD density and molar volume are compared with the measurements and temperature-dependent descriptions of Mochinaga and Igarashi [18]. 73
5.8 Excess molar volume of NaCl – $NdCl_3$ and NaCl – $PuCl_3$ 74

5.9 Absolute volumetric properties of NaCl – $CeCl_3$ – $NdCl_3$ along the investigated equal-Ce/Nd path. Direct PIM–MD density and molar volume are compared with the corresponding binary-derived RK–Muggianu predictions. 75
5.10 Ternary excess molar volume and RK–Muggianu comparison 76
5.11 Fixed-loading volumetric comparison at 900 K 77
5.12 Interval-average isobaric heat capacities obtained from the PIM-MD simulations over approximately 900–1200 K for the binary lanthanide-chloride systems, compared with the corresponding actinide-chloride benchmark datasets. Error bars represent the propagated 95% confidence intervals. 79
5.13 Interval-average isobaric heat capacity of the NaCl – $CeCl_3$ – $NdCl_3$ system along the equimolar $CeCl_3$ – $NdCl_3$ composition path. The horizontal coordinate is the total rare-earth chloride fraction, $x(CeCl_3) + x(NdCl_3)$. Error bars represent the propagated 95% confidence intervals. 79
5.14 Excess isobaric heat capacities of the binary lanthanide-chloride systems compared with the corresponding actinide-chloride benchmark datasets. The fitted lines denote covariance-aware Redlich–Kister representations of the direct PIM-MD values. . . 80
5.15 Excess isobaric heat capacity of the NaCl – $CeCl_3$ – $NdCl_3$ system along the equimolar $CeCl_3$ – $NdCl_3$ composition path. The horizontal coordinate is $x(CeCl_3) + x(NdCl_3)$. The line represents the covariance-aware fourth-order descriptive interpolation. 81
5.16 Mixing enthalpy of NaCl – $CeCl_3$. Direct PIM–MD values at 1100 K are compared with the calorimetric description of Papatheodorou and Kleppa [26] at 1118 K, the independently parameterised PMF-informed MIVM, and the benchmark-calibrated MIVM. The calibrated curve uses the experimental mixing enthalpy during parameter estimation and therefore represents a semi-empirical reproduction rather than an independent validation. 84
5.17 Mixing enthalpy of NaCl – $NdCl_3$. Direct PIM–MD values at 1100 K are compared with the 16 calorimetric measurements of Gaune-Escard et al. [20] at 1124 K, a shape-preserving guide through the experimental values, the PMF-informed MIVM, and the MIVM curve calibrated against the complete experimental dataset. 85
5.18 Direct PIM–MD and full three-component PMF-informed MIVM mixing enthalpies for NaCl – $CeCl_3$ – $NdCl_3$ along the equal-Ce/Nd composition path. Here, $x(LnCl_3) = x(CeCl_3) + x(NdCl_3)$ and $x(CeCl_3) = x(NdCl_3)$. Solid curves span the directly simulated interval, whereas dashed portions toward the pure-component limits are model extrapolations. 86
5.19 Predicted thermal conductivity of NaCl – $CeCl_3$ 88
5.20 Experimental validation of the NaCl – $CeCl_3$ thermal-conductivity estimates 89
5.21 Predicted thermal conductivity of NaCl – $NdCl_3$ 91
5.22 Pure-NaCl reference for the equal-Ce/Nd ternary SCM analysis 92
5.23 Five-nanosecond viscosity of NaCl – $NdCl_3$ 94

5.24 Temporal persistence of the Nd-centred network at 900 K 95
5.25 Five-nanosecond viscosity of $NaCl - CeCl_3$ 96
5.26 Temporal persistence of the Ce-centred network at 900 K 98
5.27 Five-nanosecond viscosity of the equal-Ce/Nd ternary path 99

A.1 Binary metal–chloride coordination-number distributions at 1100 K. Cell values denote percentage occurrence. 117
A.2 Supporting composition-dependent RDFs at 900 K. These low- temperature results provide the structural extreme complementary to the 1100 K comparison in the main text. 118
A.3 Supporting composition-dependent RDFs at 1200 K. Together with Figure A.2, these data show the low- and high-temperature structural limits of the investigated range. 119
A.4 Supporting binary cluster-size and shared-chloride connectivity results over 900–1200 K. 120
A.5 Trajectory-length sensitivity of the non-converged $NaCl - CeCl_3$ states 129

List of Tables

2.1 Literature evidence relevant to the validation and interpretation strategy of the present thesis. "Limited" denotes narrow composition coverage, indirect/derived evidence or incomplete directly reusable data; it does not imply that the property has never been measured. . . . 16

4.1 Composition and temperature coverage. Realised mole fractions derived from the integer cation populations were used in calculations. . . . 37
4.2 Ionic properties used in the Polarizable Ion Model. . . . 37
4.3 Principal numerical settings used for the interaction model. . . . 38
4.4 Simulation stages and principal analysis roles. . . . 39
4.5 Principal output intervals used in the extended NVT simulations. . . . 40
4.6 Property-specific retained data and primary statistical treatment. . . . 55
4.7 Validation and benchmarking hierarchy used for the reported property groups. . . . 59

5.1 Near-pure first-shell coordination numbers and shared-chloride linkage populations at 1100 K for the lanthanide melts and the actinide results supplied by Ter Veer et al. [79]. The actinide coordination numbers are digitised near-pure values. The lanthanide face/higher-order category includes the negligible $C_{\geq 4}$ contribution, which remains below 0.1%. . . . 68
5.2 Experimental validation and Pu viscosity benchmark for NaCl – $NdCl_3$ 94
5.3 Experimental validation and U viscosity benchmark for NaCl – $CeCl_3$ 97

A.1 Verified production-window and uncertainty treatment for density, molar volume and excess molar volume. . . . 121
A.2 Heat-capacity production windows and the evidence supporting their use. . . . 122
A.3 Maximum relative variation of selected thermal-conductivity inputs across the tested discard fractions, measured relative to the primary 20% result. . . . 123
A.4 NaCl–$NdCl_3$ 5 ns viscosity values and reporting status over the complete 900–1200 K dataset. Pass and Caution states are reportable; Review states are retained as non-converged provisional values. . . . 124

A.5 Composition-resolved 900 K NaCl – $NdCl_3$ temporal-persistence results. Persistence values are $1/e$ times in ps. The topology-switching rate is in $\mathrm{ps}^{-1}\,\mathrm{Nd}^{-1}$. Corner, edge and face columns are percentages among linked Nd–Nd pairs. 126

A.6 NaCl–$CeCl_3$ 5 ns viscosity values and reporting status. Pass and Caution states are reportable; Review states are retained as non-converged provisional values. 127

A.7 NaCl–$CeCl_3$–$NdCl_3$ 5 ns viscosity values along the equal-Ce/Nd path. Pass and Caution states are reportable; Review states are retained as non-converged provisional values. 129

List of Abbreviations and Nomenclature

List of Abbreviations

ACF	autocorrelation function
AICc	small-sample corrected Akaike information criterion
CN	coordination number
DFT	density functional theory
FFT	fast Fourier transform
GK	Green–Kubo
GLS	generalized least squares
MCFR	molten chloride fast reactor
MCRE	Molten Chloride Reactor Experiment
MD	molecular dynamics
MIVM	Molecular Interaction Volume Model
MSR	molten salt reactor
NPT	constant particle number, pressure and temperature ensemble
NVT	constant particle number, volume and temperature ensemble
PIM	polarizable ion model
PMF	potential of mean force
RDF	radial distribution function
RIM	rigid ion model
RK	Redlich–Kister
RMSE	root-mean-square error
SCM	structural-coherence model
XAFS	X-ray absorption fine structure

Nomenclature

C_p	isobaric heat capacity
C_p^E	excess isobaric heat capacity
$C_{p,\mathrm{vol}}$	volumetric isobaric heat capacity
$g_{ij}(r)$	partial radial distribution function
ΔH_{mix}	molar enthalpy of mixing
k_{B}	Boltzmann constant
ℓ_{sc}	structural coherence length
N_{eff}	effective number of statistically independent samples
R	molar gas constant
T	absolute temperature
V_m	molar volume
V_m^E	excess molar volume
v_s	adiabatic speed of sound
$W_{ij}(r)$	pair potential of mean force
x_i	component mole fraction on a salt-formula-unit basis
α_V	volumetric thermal-expansion coefficient
η	dynamic shear viscosity
κ_S	adiabatic compressibility
κ_T	isothermal compressibility
λ	thermal conductivity
ρ	mass density

1

Introduction

1.1 Background

The transition towards a low-carbon energy system requires rapid expansion of low-emission electricity while maintaining reliable supply. Variable renewable generation is expected to provide a major share of this expansion, but deeply decarbonised systems may also require firm resources: low-emission generators that can supply electricity on demand when variable output is unavailable. Nuclear power is one such firm source and supplied approximately 9% of global electricity in 2024. In addition to electricity, nuclear systems can provide continuous heat for district heating and industrial processes, including applications requiring temperatures above those readily delivered by many conventional low-carbon heat technologies [1–3].

The molten salt reactor (MSR) is one of the advanced reactor families selected for international research and development by the Generation IV International Forum. The term encompasses concepts in which a molten salt serves as coolant, fuel carrier or both. In homogeneous liquid-fuel configurations, fissile and fertile materials are dissolved directly in a circulating salt. The salt therefore carries the nuclear fuel, transports heat from the core and provides the chemical environment in which actinides and fission products are present. Depending on salt composition, moderation and core design, MSRs may operate with thermal, intermediate or fast neutron spectra. Their elevated outlet temperatures can support efficient electricity generation and, in suitable plant configurations, direct process-heat applications [4–6].

Although molten salt reactors have not reached widespread commercial deployment, liquid-fuel reactor technology has an important experimental history. Work at Oak Ridge National Laboratory produced the Aircraft Reactor Experiment in 1954, demonstrating circulation of a uranium-bearing fluoride fuel salt at high temperature. The subsequent Molten Salt Reactor Experiment operated from 1965 to 1969 and accumulated more than 13,000 full-power hours. It used a circulating fluoride fuel salt in a graphite-moderated core and provided a substantially longer demonstration of liquid-fuel operation, reactor control and fuel-salt handling [7].

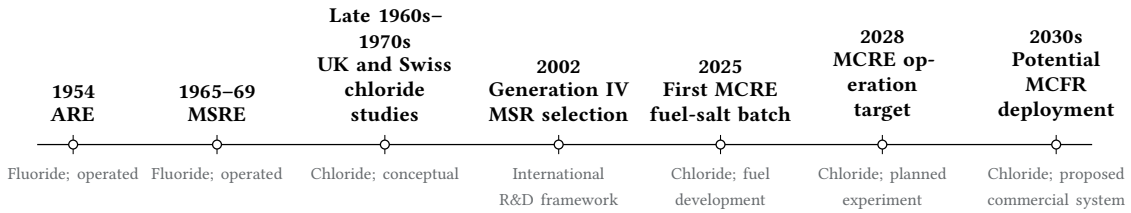

Figure 1.1. Selected milestones in the historical development of molten salt reactor technology. The timeline distinguishes the experimentally operated fluoride-based liquid-fuel reactors from conceptual and planned fast-spectrum chloride systems. UK and Swiss studies established early conceptual designs for molten chloride fast reactors, while the Molten Chloride Reactor Experiment (MCRE) represents a current experimental development programme. MCRE is anticipated to operate in 2028, whereas a subsequent commercial Molten Chloride Fast Reactor (MCFR) could potentially be deployed in the 2030s. Compiled from the Generation IV International Forum [4], Oak Ridge National Laboratory [7], Smith *et al.* [8], Taube [9] and the U.S. Department of Energy, Office of Nuclear Energy [11].

The distinction between this historical experience and molten chloride reactor development is important. Both Oak Ridge experiments used fluoride salts, whereas no fast-spectrum molten chloride reactor was constructed or operated in the same period. Chloride-fuelled fast-reactor concepts were nevertheless studied during the late 1960s and 1970s. British investigations considered mixtures containing NaCl, UCl_3 and $PuCl_3$, while Swiss work examined related plutonium-bearing chloride breeder configurations. These concepts were intended to preserve a harder neutron spectrum and support uranium–plutonium fuel cycles, but they remained analytical designs as international development priorities shifted towards water-cooled reactors and solid-fuel, liquid-metal-cooled fast reactors [8–10].

Interest in molten chloride fast reactors has since re-emerged within broader efforts to develop advanced reactors and closed fuel cycles. A prominent contemporary programme is the Molten Chloride Reactor Experiment (MCRE), a planned fast-spectrum, salt-fuelled experiment using a uranium chloride fuel salt. MCRE is intended as a short-duration experimental test whose results will provide data crucial to the development of TerraPower and Southern Company's Molten Chloride Fast Reactor, rather than as a commercial electricity-generating plant. In 2025, the United States Department of Energy reported production of the first batch of fuel salt for MCRE, marking progress towards physical demonstration. Nevertheless, molten chloride fast-reactor technology remains pre-commercial at the time of writing [6, 11, 12].

Chloride salts are of particular interest for fast-spectrum applications because they generally slow neutrons less strongly than commonly considered fluoride mixtures, thereby helping to preserve a hard neutron spectrum. This characteristic supports uranium–plutonium breeding, actinide burning and related fuel-cycle applications. Actinide trichlorides can also form liquid mixtures with alkali chlorides such as NaCl, allowing relatively high actinide concentrations to be incorporated into the fuel salt. Moreover, molten salts permit high-temperature heat transport at low primary-system pressure, avoiding the highly pressurised primary circuit required in conventional water-cooled reactors. These advantages are accompanied by unresolved challenges involving corrosion, salt purification and redox control, chlorine-isotope management, fission-product behaviour and the qualification of structural materials [6, 10].

The multifunctional nature of a liquid fuel salt makes its properties central to reactor analysis. Density influences fuel inventory, thermal expansion and buoyancy-driven circulation. Heat capacity and thermal conductivity affect the storage and transport of thermal energy, whereas viscosity influences flow, pumping requirements and convective heat transfer. These macroscopic properties are linked to microscopic features of the liquid, including cation–anion coordination, chloride sharing, short-range ordering and the association of multivalent cations. They vary with temperature and composition and may evolve as actinides are consumed and fission products accumulate. Consequently, a molten chloride fuel cannot be represented simply as an inert coolant with constant material properties.

Direct experimental characterisation of actinide-bearing chloride melts is challenging. Chloride salts are hygroscopic and must be handled under controlled atmospheres to limit oxygen- and moisture-derived impurities. Measurements are performed at elevated temperatures, the melts can be corrosive towards containment and measurement materials, and uranium- or plutonium-bearing work requires specialised radiological facilities. Available datasets are therefore incomplete, particularly for multicomponent salt compositions [6, 13].

These experimental constraints motivate a deliberate transition from direct actinide measurements to non-radioactive lanthanide model systems. Trivalent lanthanide and actinide chlorides share formal charge, broadly comparable ionic sizes and strongly polarising cation–chloride interactions, allowing selected features of actinide-bearing melts to be studied without the radiological burden of uranium- or plutonium-containing experiments. The analogy is not universal: differences in ionic radius, electronic structure and redox chemistry mean that simulant suitability must be tested separately for each property. Molecular simulation provides the required bridge by evaluating the same thermophysical, thermodynamic, structural and transport quantities over controlled temperature and composition grids. The present thesis therefore applies polarizable ion model (PIM) molecular dynamics (MD) to molten $NaCl-CeCl_3$, $NaCl-NdCl_3$ and $NaCl-CeCl_3-NdCl_3$, using Ce- and Nd-containing chlorides as property-specific model systems rather than universal replacements for uranium and plutonium salts [14–17].

1.2 Research Problem and Knowledge Gap

Reliable composition- and temperature-dependent material-property data are required for the design and analysis of molten-salt reactor systems. Density determines the relationship between salt composition, fuel inventory and reactor volume, while its temperature dependence influences thermal expansion and buoyancy-driven circulation. Heat capacity and thermal conductivity govern the storage and transport of thermal energy, whereas viscosity affects flow resistance, pumping requirements and convective heat transfer. Mixing enthalpies and excess molar volumes provide additional information on non-ideal interactions within multicomponent liquids. Uncertainty in these properties therefore propagates into reactor-physics, thermal-hydraulic and safety calculations. Despite their importance, the thermophysical-property databases available for molten salts remain incomplete, particularly for actinide-bearing chlorides and compositionally complex fuel salts [6, 13].

The limited availability of reliable measurements is partly a consequence of the experimental conditions required for molten chloride salts. Chlorides are hygroscopic and can react with mois-

ture and oxygen, meaning that salt purification, sample preparation and measurements must be performed under carefully controlled atmospheres. At operating temperatures, the melts can be corrosive towards crucibles, containment materials and measurement probes. Thermal-property measurements may additionally be affected by convection, radiative heat transfer, salt creeping and chemical contamination. These difficulties become more severe when uranium, plutonium or other radioactive elements are present because specialised facilities, materials and safety procedures are then required. Consequently, available measurements frequently cover only selected compositions, temperatures or individual properties rather than complete composition–temperature domains [6, 13].

The existing evidence is also distributed unevenly between the two binary systems investigated in this thesis. The $NaCl - NdCl_3$ system has a comparatively substantial experimental basis. Density and excess-molar-volume data have been reported as functions of composition and temperature [18, 19], while calorimetric studies provide mixing enthalpies over the full liquid composition range at selected temperatures [20, 21]. Additional studies address phase equilibria, electrical conductivity, internal mobility and thermal conductivity [22–25]. These data provide several opportunities for simulation validation, but they were obtained using different experimental techniques and generally do not cover all properties over one common set of temperatures and compositions.

The validation basis for $NaCl - CeCl_3$ is more restricted. Thermochemical measurements and phase-equilibrium studies provide evidence of non-ideal behaviour in alkali-chloride–$CeCl_3$ mixtures [26–28], and thermal-conductivity measurements have recently been reported for $CeCl_3 - MCl$ melts [29]. However, an experimental dataset equivalent in breadth to that available for $NaCl - NdCl_3$ has not been established for density, heat capacity, viscosity, diffusion, thermal conductivity and microscopic liquid structure. The binary research problem is therefore not simply an absence of literature. It is the absence of one internally consistent description of both $NaCl - CeCl_3$ and $NaCl - NdCl_3$ across their complete composition ranges and over the same temperature interval. An even larger knowledge gap concerns the ternary $NaCl - CeCl_3 - NdCl_3$ system. Recent work has clarified the phase behaviour and property-dependent suitability of $CeCl_3$ and $NdCl_3$ as non-radioactive analogues for selected uranium- and plutonium-chloride properties [16, 17]. Nevertheless, the literature surveyed for this thesis did not reveal a systematic dataset for the thermophysical, thermodynamic, structural and transport behaviour of molten $NaCl - CeCl_3 - NdCl_3$. It is therefore not known whether binary property trends extend smoothly into the ternary composition space or whether the simultaneous presence of Ce and Nd produces additional non-ideal effects. In particular, direct information is lacking on how the two trivalent cations compete for chloride coordination, whether mixed Ce–Cl–Nd linkages form, and how such local environments affect density, thermodynamic mixing and transport behaviour.

A further gap lies in the interpretation of macroscopic properties in terms of microscopic liquid structure. Experimental X-ray absorption measurements show that molten $CeCl_3$ and $NdCl_3$ possess well-defined short-range cation–chloride coordination environments [14]. Atomistic studies of related rare-earth chloride mixtures further demonstrate that alkali-chloride addition can alter cation connectivity, isolate multivalent complexes and create structural heterogeneity. However, many published investigations focus either on a limited set of bulk properties or on local structural descriptors. Few systematically connect radial distribution functions, coordination-number distri-

butions, chloride sharing and cluster formation to excess molar volume, mixing enthalpy, viscosity and thermal conductivity across complete binary composition ranges.

Molecular simulation can help address these gaps, but the reliability of its predictions depends on the interaction model and on the statistical quality of the calculated properties. The strong local electric fields associated with trivalent cations make explicit ionic polarisation important in rare-earth chloride melts. The recently developed DFT-based polarizable force-field series for molten rare-earth chlorides provides a consistent interaction framework covering both Ce and Nd [15, 30]. Nevertheless, this framework has not yet been used to establish a unified structure–property dataset for the complete NaCl – $CeCl_3$ and NaCl – $NdCl_3$ binaries together with the mixed NaCl – $CeCl_3$ – $NdCl_3$ system over a common temperature range.

The central research problem addressed in this thesis is therefore the absence of a statistically validated and internally consistent atomistic description of the composition- and temperature-dependent thermophysical, thermodynamic, structural and transport behaviour of these binary and ternary molten chloride systems. The present work addresses this problem using PIM MD, combining comparison with available binary reference data with new predictions for poorly characterised compositions. The research aim and objectives derived from this problem are presented in the following section.

1.3 Research Aim and Objectives

The aim of this thesis is to determine and physically interpret the composition- and temperature-dependent behaviour of molten NaCl – $CeCl_3$, NaCl – $NdCl_3$ and NaCl – $CeCl_3$ – $NdCl_3$ using Polarizable Ion Model molecular dynamics, and to assess the extent to which the binary lanthanide systems reproduce selected properties of actinide-bearing chloride melts.

The work pursues four linked objectives. First, a common simulation dataset is constructed for the complete binary composition ranges and for the equal-Ce/Nd ternary path $x_{CeCl_3} = x_{NdCl_3} = (1 - x_{NaCl})/2$, with $x_{NaCl} = 0.10$–0.90. Second, density, molar volume, excess molar volume, heat capacity, excess heat capacity, mixing enthalpy, viscosity and structural-coherence thermal-conductivity estimates are determined together with property-specific statistical verification. Third, partial pairwise radial distribution functions, coordination-number distributions, chloride-sharing populations and connectivity descriptors are used to explain the macroscopic trends. Finally, the binary predictions are compared with available same-system evidence and with selected NaCl – UCl_3 and NaCl – $PuCl_3$ data before the validated workflow is extended to the ternary composition line.

A common temperature grid of 900 K, 1000 K, 1100 K and 1200 K was chosen to overlap the temperature range of the available molten-chloride property literature, to provide four evenly spaced points for temperature derivatives and regressions, and to expose both lower- and higher-temperature transport behaviour. The simulations describe homogeneous liquid trajectories; where a low-temperature, rare-earth-rich state lies below the equilibrium liquidus, the result is interpreted as a metastable-liquid extension rather than as a prediction of phase stability [22, 27, 31].

1.4 Research Questions

The overarching research question is:

To what extent can Polarizable Ion Model molecular dynamics predict and explain the composition- and temperature-dependent thermophysical, thermodynamic, structural and transport behaviour of molten $NaCl-CeCl_3$, $NaCl-NdCl_3$ and $NaCl-CeCl_3-NdCl_3$, and what do these systems reveal about the property-specific use of lanthanide chlorides as simulants for actinide-bearing molten salts?

This question is addressed through the following supporting questions:

RQ1: How do the thermophysical, thermodynamic and transport properties of the two binary melts vary with composition and temperature, and which trends demonstrate non-ideal liquid behaviour?

RQ2: How do partial pairwise radial distribution functions, cation–chloride coordination, chloride sharing and multivalent-cation connectivity evolve across the binary and ternary composition ranges?

RQ3: Which microscopic mechanisms best explain the calculated trends in density, excess molar volume, heat capacity, mixing enthalpy, viscosity and structural-coherence thermal conductivity?

RQ4: How closely do the binary predictions reproduce available same-system experiments and simulations, and what do the remaining deviations reveal about uncertainty and model limitations?

RQ5: For which properties do $NaCl-CeCl_3$ and $NaCl-NdCl_3$ provide useful analogues of selected $NaCl-UCl_3$ and $NaCl-PuCl_3$ behaviour?

RQ6: Does the equimolar-Ce/Nd ternary path interpolate between the two binary systems, or do mixed Ce–Cl–Nd environments produce additional non-ideal behaviour?

1.5 Scope and Thesis Structure

1.5.1 Scope of the Study

This thesis investigates the molten binary systems $NaCl-CeCl_3$ and $NaCl-NdCl_3$, together with selected compositions of the ternary $NaCl-CeCl_3-NdCl_3$ system. The complete binary composition ranges are considered, from pure NaCl to pure $CeCl_3$ or $NdCl_3$, while the ternary calculations follow the equal-Ce/Nd pseudo-binary path $x_{CeCl_3} = x_{NdCl_3}$, with $x_{NaCl} = 0.10$–0.90. The systems are studied at 900 K, 1000 K, 1100 K and 1200 K. This common grid supports direct cross-system comparison and temperature-dependent regressions, while phase stability is interpreted separately from the homogeneous-liquid MD sampling.

The work is based on PIM MD. The calculated properties include density, molar volume, excess molar volume, heat capacity, excess heat capacity, mixing enthalpy and selected transport properties, particularly viscosity and thermal conductivity. Where sufficient trajectory information and statistical quality are available, additional dynamical quantities may be considered as supporting analyses. The microscopic liquid structure is characterised using radial distribution functions

(RDFs), coordination number (CN) distributions, chloride-sharing analysis and structural speciation. These structural quantities are used to interpret the governing physical and chemical mechanisms behind the observed macroscopic trends.

The binary systems provide the principal validation basis. Calculated properties are compared with available experimental measurements, previous molecular simulations and thermodynamic descriptions. Comparisons with chemically related actinide chloride systems are used to assess the suitability of Ce- and Nd-containing melts as non-radioactive simulants. This assessment is strictly property-dependent. Similarity between a rare-earth and an actinide system for one property is not assumed to demonstrate equivalence for all thermophysical, thermodynamic, structural or transport properties.

The ternary $NaCl - CeCl_3 - NdCl_3$ system is treated primarily as a predictive case because direct experimental data are limited. Its analysis focuses on whether the behaviour observed in the two binary systems can be extended into ternary composition space and whether mixed Ce–Cl–Nd environments introduce additional non-ideal effects.

The thesis does not include reactor-core neutronics, fuel-cycle calculations, radiation-damage modelling, corrosion experiments, materials-compatibility testing or reactor-scale thermal-hydraulic design. It also does not perform a complete CALPHAD or FactSage assessment. Phase diagrams and thermodynamic models are used only as supporting literature and comparison sources. No new experimental measurements are carried out; the original contribution of the work lies in molecular simulation, statistical post-processing and the physical interpretation of the resulting property and structural data.

1.5.2 Thesis Structure

Following this introductory chapter, Chapter 2 critically reviews the available experimental, computational and thermodynamic evidence for rare-earth and actinide chloride melts. Particular attention is given to the $NaCl - CeCl_3$ and $NaCl - NdCl_3$ binary systems, the limited knowledge available for $NaCl - CeCl_3 - NdCl_3$, and the property-dependent use of Ce and Nd compounds as simulants for uranium- and plutonium-containing chloride salts.

Chapter 3 presents the physical and statistical-mechanical foundations of the study, including the Polarizable Ion Model, solution thermodynamics, partial pairwise structural descriptors and transport-property relations.

Chapter 4 describes the molecular-simulation workflow, including system preparation, interaction potentials, equilibration and production conditions, property calculations, structural analysis and statistical convergence procedures.

Chapter 5 presents and discusses the calculated thermophysical, thermodynamic, structural and transport properties. The binary results are first validated against available reference data, after which the governing structure–property relationships, simulant behaviour and ternary predictions are examined.

Finally, Chapter 6 summarises the main findings in relation to the research questions, discusses the limitations of the simulations and provides recommendations for future experimental, computational and reactor-oriented research.

2

Literature Review

2.1 Introduction

The purpose of this chapter is to establish what is already known about the molten chloride systems relevant to this thesis, where the available evidence is strong or weak, and which questions remain unresolved. Detailed theoretical definitions of the Polarizable Ion Model (PIM), radial distribution functions, coordination numbers, excess properties and transport relations are reserved for Chapter 3. Here, those concepts are discussed only insofar as they are needed to compare published studies and to define the evidence base against which the present calculations are assessed.

The literature is unevenly distributed across the systems of interest. NaCl – $NdCl_3$ has a comparatively broad experimental record spanning volumetric properties, mixing enthalpy, phase behaviour, electrical conductivity and selected transport measurements. NaCl – $CeCl_3$ has useful phase-equilibrium, thermochemical and thermal-conductivity information but a less complete set of directly reusable liquid-property data. For NaCl – $CeCl_3$ – $NdCl_3$, the accessible literature does not provide a comparable composition- and temperature-resolved thermophysical, structural and transport dataset. The literature review therefore serves two functions: it identifies property-specific validation anchors for the binary simulations and establishes which ternary results must remain predictions rather than validated quantities.

A second theme is simulant fidelity. Ce- and Nd-containing chlorides are useful non-radioactive model systems because trivalent lanthanides and actinides share formal charge and broadly similar chloride coordination chemistry. That analogy is nevertheless property dependent. Recent work indicates that Nd is a closer analogue of Pu for several local-structure and transport observables, whereas Ce can more closely reproduce selected U-containing phase and volumetric trends [16, 17]. Consequently, the literature does not support treating either lanthanide as a universal actinide substitute.

2.2 Review Scope and Evidence Strategy

The review prioritises primary experimental papers, peer-reviewed molecular simulation studies and modern thermodynamic reassessments directly relevant to $NaCl - CeCl_3$, $NaCl - NdCl_3$, rare-earth chloride structure and lanthanide–actinide comparison. Authoritative nuclear-technology reports are used only to establish application context. Secondary compilations are used where they preserve otherwise difficult-to-access experimental correlations, but the original experimental attribution is retained whenever identifiable.

Evidence is interpreted hierarchically. A measurement or prior simulation of the same chemical system at a matched composition and temperature provides the strongest validation target. Related actinide systems provide analogue or simulant comparisons rather than direct validation. Graph-only data, limited composition coverage and derived quantities are treated as weaker constraints. Where no direct source was located, the absence is described as an evidence gap rather than proof that no measurement exists.

This distinction is particularly important for transport properties. Density and mixing enthalpy have direct experimental anchors in at least one of the binary systems, whereas broad-composition viscosity data are sparse. The quality of a PIM prediction must therefore be judged property by property, using independent experiment where possible and structural consistency, uncertainty analysis and comparison with related systems where direct data are not available.

2.3 Molten Chloride Salts and the Simulant Problem

2.3.1 Relevance to Fast-Spectrum Nuclear Systems

Molten chlorides are relevant to fast-spectrum nuclear concepts because they can dissolve substantial concentrations of actinide chlorides while maintaining a comparatively hard neutron spectrum. They are also central to pyrochemical fuel-cycle processes. In a liquid-fuel reactor, the salt is simultaneously a chemical medium for actinides and fission products and a heat-transfer fluid, so its density, heat capacity, viscosity, thermal conductivity and phase behaviour enter directly into reactor and fuel-cycle analysis [6, 10, 13].

The same characteristics that make chloride salts attractive also complicate the acquisition of reliable property data. High temperature, hygroscopicity, corrosion, impurity sensitivity and the radiological constraints associated with U- or Pu-bearing salts limit the number of systematic measurements over broad composition ranges. The result is an evidence base assembled from measurements performed with different techniques, purities, temperature intervals and uncertainty reporting conventions rather than one internally consistent database.

2.3.2 Why Ce and Nd Are Useful but Non-Universal Analogues

Lanthanide chlorides provide experimentally accessible model systems for selected features of actinide chloride chemistry. The basis of the analogy is not simply periodic-table proximity: the relevant comparison is between trivalent cations embedded in a chloride environment. Their local ionic size, polarizability and chloride interaction strength affect first-shell geometry, network

connectivity and transport. Consequently, chemically similar cations can reproduce one property closely while differing for another.

This point is demonstrated directly by recent comparative studies. Goloviznina and Salanne found Nd-containing chlorides to be closer to Pu-containing systems than Ce-containing chlorides when force matching, local structure, density and viscosity were considered [16]. Alders et al. reached a complementary phase-behaviour conclusion: $NaCl-NdCl_3$ closely tracks $NaCl-PuCl_3$ liquidus behaviour, whereas $NaCl-CeCl_3$ is more similar to $NaCl-UCl_3$ in the assessed systems [17]. The implication for the present thesis is therefore a property-specific Ce/U and Nd/Pu comparison, not a universal surrogate assignment.

2.3.3 Relevance and Limits of the $NaCl-CeCl_3-NdCl_3$ Model System

The ternary $NaCl-CeCl_3-NdCl_3$ melt is not itself a reactor fuel composition. Its value is that two chemically similar but non-identical trivalent cations can be studied in the same NaCl matrix without radiological constraints. This makes the system a controlled test of whether binary structure–property trends persist when Ce- and Nd-centred coordination environments coexist.

The comparison must nevertheless remain bounded by the investigated composition path. The present thesis follows the equal-Ce/Nd line rather than the complete ternary triangle. Literature on related systems, including $NaCl-UCl_3-CeCl_3$, confirms that multicomponent actinide/lanthanide chloride chemistry is of practical interest [32], but it does not provide direct thermophysical or transport validation for the target Ce/Nd ternary.

2.4 Polarizable Molecular-Dynamics Evidence for Rare-Earth Chlorides

The need for an explicitly polarizable description of multivalent chloride melts is well established. Reviews of ionic melts show that induced electronic polarisation modifies the effective interaction between highly charged cations and the diffuse chloride anion and can change both local structure and transport [30]. The formal theory and energy terms are developed in Section 3.2; the literature question here is whether a consistent rare-earth PIM exists and what evidence supports its use for Ce/Nd mixtures.

Goloviznina et al. developed a DFT-derived polarizable force-field series for trivalent rare-earth chlorides from La to Eu and applied it to pure salts and NaCl-containing mixtures [15]. The study reported density, heat capacity, diffusion, viscosity and local structure and captured systematic lanthanide trends in cation–chloride distance and coordination. This is important for the present work because Ce and Nd were parameterised within one internally consistent framework rather than through unrelated potentials.

The same literature also establishes an important limitation. Agreement for pure salts or dilute mixtures does not guarantee quantitative transferability to the complete $NaCl-MCl_3$ composition range or to a mixed Ce/Nd melt. Ternary predictions additionally require a Ce–Nd cross interaction for which no direct target-ternary measurement is available. Binary comparison is therefore not merely a preliminary step; it is the principal test of whether the interaction model remains credible before the mixed-lanthanide system is interpreted.

2.5 Structural Evidence and Structure–Property Relationships

Direct structural measurements provide one of the strongest checks on the microscopic realism of a force field. XAFS measurements of molten $CeCl_3$ and $NdCl_3$ report distinct first-shell structures, with Ce–Cl and Nd–Cl distances of approximately 2.81 and 2.73 Å, respectively, and average coordination numbers of about 6.52 and 6.96 under the reported conditions [14]. These values demonstrate that Ce and Nd cannot be treated as structurally identical despite sharing the same formal charge.

Polarizable simulations extend this picture from mean first-shell quantities to distributions of coordination states. The rare-earth force-field study reports broad six- to nine-fold coordination environments whose populations change across the lanthanide series and with NaCl dilution [15]. The important literature conclusion is therefore not that a melt contains one fixed $[MCl_n]$ species, but that it samples an ensemble of rapidly interconverting local environments.

Longer-range connectivity is equally important. Corradini, Madden and Salanne showed for alkali–trivalent-halide mixtures that viscosity is related to both first-shell structural relaxation and the networks that develop between trivalent cations as their concentration increases [33]. Emerson et al. subsequently described NaCl as a "spacer salt" in $LaCl_3$ – NaCl, demonstrating that alkali-chloride addition can separate multivalent coordination environments and generate substantial structural heterogeneity [34]. Together, these studies provide a literature basis for interpreting composition-dependent transport through coordination, chloride sharing and network formation rather than through one RDF peak alone.

What is not established in the existing literature is the detailed behaviour of mixed Ce–Cl–Nd connectivity across the target ternary path. In particular, the accessible studies do not determine whether hetero-cation bridges possess lifetimes distinct from Ce–Cl–Ce or Nd–Cl–Nd connections, or whether the simultaneous presence of Ce and Nd creates a unique dynamical network. These questions therefore require direct analysis of the present trajectories rather than extrapolation from binary structural trends.

2.6 Binary Experimental and Computational Evidence

2.6.1 NaCl – $NdCl_3$: Stronger Validation Anchor

Among the two target binaries, NaCl – $NdCl_3$ provides the broader validation basis. Density and molar-volume measurements have been reported as functions of composition and temperature, including evidence of non-zero excess molar volume [18, 19]. The excess-volume isotherm reported by Sato, Okamoto and Ogawa exhibits a positive NaCl-rich maximum near $x(\mathrm{NdCl_3}) \approx 0.2$, providing a direct test of whether a model reproduces volumetric non-ideality rather than only total density [19].

Calorimetry provides an independent energetic constraint. Gaune-Escard et al. measured the complete liquid composition range at 1124 K and report an enthalpy-of-mixing minimum of approximately $-5.7\ \mathrm{kJ/mol}$ near $x(\mathrm{NdCl_3}) = 0.4$, with an estimated experimental accuracy of about 6% [20]. The published dataset contains point-to-point scatter around the fitted/broad minimum, so individual tabulated points and the authors' summarized minimum should not be

treated as identical quantities. The negative sign and broad intermediate-composition minimum nevertheless provide a strong direct test of mixing energetics.

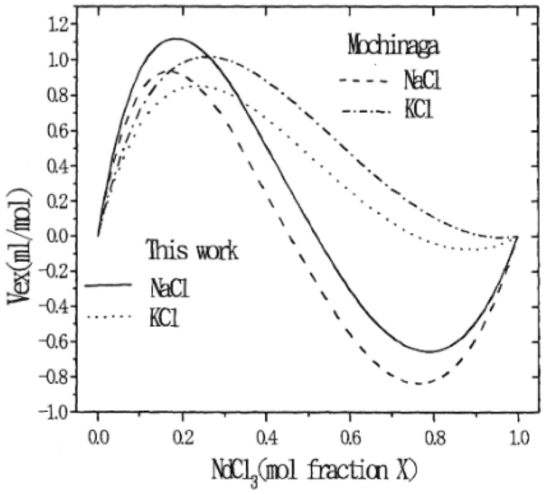

(a) Excess molar volume.

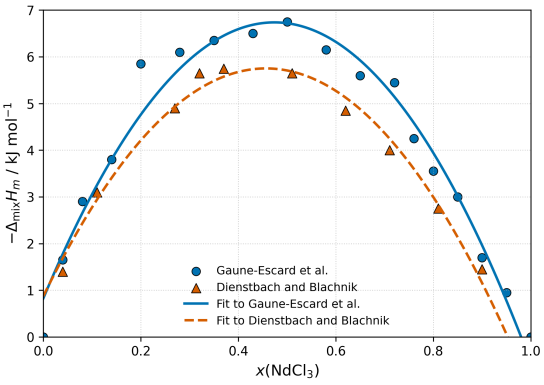

(b) Mixing enthalpy.

Figure 2.1. Experimental evidence for non-ideal behaviour in molten Nd-containing alkali-chloride mixtures: excess molar volume from Sato, Okamoto and Ogawa and molar enthalpy of mixing from Gaune-Escard et al. Adapted from Refs. [19, 20].

The phase-equilibrium literature independently confirms pronounced non-ideal chemistry. Earlier measurements identify intermediate-compound behaviour, while the modern reassessment of Alders et al. represents the intermediate region as a $Na_{3x}Nd_{2-x}Cl_6$ solid-solution field and places an assessed eutectic near $x(NdCl_3) = 0.355$ and 718 K [17, 22]. These data are not used here to construct a new phase diagram. Their role is to establish liquidus context, identify state points that may represent metastable-liquid extensions, and demonstrate that ideal mixing is not an adequate description of the binary chemistry.

Transport evidence is less complete but still useful. Potapov, Rycerz and Gaune-Escard measured electrical conductivity over broad composition and temperature ranges and found strong deviations from additivity, with conductivity decreasing as $NdCl_3$ is added to NaCl [23]. Zabłocka-Malicka and Szczepaniak used conductivity and molar-volume data to derive internal trivalent-cation mobilities [24]. Thermal-conductivity measurements are available for selected Nd-containing compositions, including an equimolar $NaCl-NdCl_3$ melt, but the coverage is insufficient for a complete composition-resolved validation [25]. No comparably broad experimental viscosity dataset was located for the finite- composition binary. Thus, $NaCl-NdCl_3$ is a strong validation anchor for volumetric and mixing-enthalpy behaviour, but only a partial anchor for transport.

2.6.2 NaCl – $CeCl_3$: Complementary Evidence

The Ce-containing binary has a more uneven evidence base. Phase-equilibrium and thermochemical studies establish non-ideal behaviour and intermediate chemistry, and the modern reassessment of Alders et al. places the $NaCl-CeCl_3$ eutectic near $x(CeCl_3) = 0.303$ and 778 K [17, 27, 28]. As for the Nd system, these data provide phase-state context rather than a thermodynamic model constructed in this thesis.

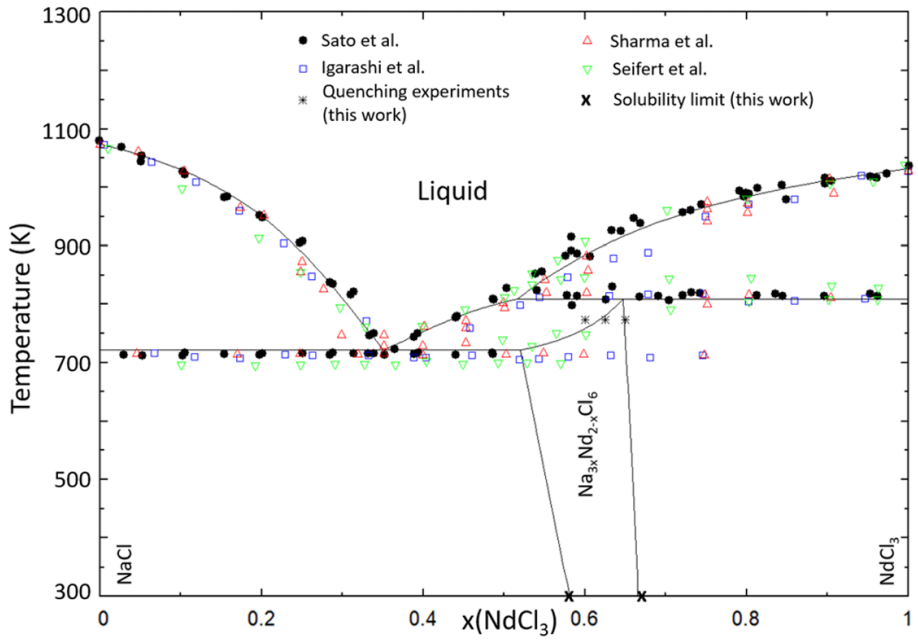

Figure 2.2. Assessed $NaCl-NdCl_3$ phase diagram showing the liquidus, eutectic behaviour and the $Na_{3x}Nd_{2-x}Cl_6$ solid-solution field. Adapted from Alders et al. [17]. The diagram is used as phase-state context for the MD temperature grid, not as a CALPHAD result of the present thesis.

Papatheodorou and Kleppa measured liquid alkali-chloride–$CeCl_3$ mixing enthalpies and found negative interaction parameters, providing direct evidence of exothermic non-ideal mixing [26]. The accessible data are less convenient for direct numerical reuse than the Nd calorimetric dataset because much of the information is graph based. Nevertheless, the experiment provides an essential same-system benchmark for the sign, scale and composition dependence of the present PIM-MD mixing enthalpies.

Thermal conductivity is the clearest directly accessible Ce transport benchmark. Bobrova and Dokutovich measured $CeCl_3-MCl$ melts and reported linear temperature correlations for several $NaCl-CeCl_3$ compositions, with an estimated relative experimental error not exceeding 5% [29]. These measurements are particularly valuable because they test the absolute structural-coherence predictions rather than only a related actinide trend. Direct finite- composition viscosity and self-diffusion measurements were not located in the reviewed accessible literature, so those quantities require more cautious interpretation.

Published density information is less straightforward. Older Ce-containing density correlations are available through compilations and are used in the present validation workflow, but the provenance and accessible tabulation are less transparent than for the Nd binary. The Ce density comparison should therefore carry less evidential weight than a directly inspected primary experimental table.

2.6.3 Property-Specific Ce/U and Nd/Pu Evidence

The literature supports a differentiated simulant picture rather than one ranking valid for every observable. Nd is particularly compelling for Pu-like local coordination and viscosity according to the comparative DFT/PIM study of Goloviznina and Salanne [16]. The phase-behaviour assess-

ment of Alders et al. likewise identifies close $NaCl-NdCl_3$/ $NaCl-PuCl_3$ correspondence, while $NaCl-CeCl_3$ more closely follows selected $NaCl-UCl_3$ behaviour [17].

These studies establish the correct standard for the present thesis: a lanthanide analogue is useful when it reproduces the composition and temperature dependence of a specified property within the accuracy relevant to that comparison. Similarity in density, coordination or viscosity cannot be promoted into evidence of universal chemical equivalence. The actinide comparisons in Chapter 5 are therefore treated as property-specific benchmarks and are kept distinct from same-system experimental validation.

2.7 Evidence for the Target Ternary System

No direct composition-resolved source was located in the reviewed accessible literature for the density, molar volume, excess molar volume, heat capacity, mixing enthalpy, viscosity or thermal conductivity of molten $NaCl-CeCl_3-NdCl_3$. Related multicomponent studies confirm the relevance of mixed actinide/lanthanide chloride chemistry but do not provide a substitute for the target system [17, 32]. The ternary results of this thesis must therefore be classified primarily as predictions constrained by binary validation and internal physical consistency.

The binary literature also shows why simple ideal interpolation is not a safe assumption. Both $NaCl-CeCl_3$ and $NaCl-NdCl_3$ exhibit non-zero excess properties, exothermic mixing and composition-dependent structural reorganisation. A binary-derived interpolation can be a useful baseline, but a difference between that baseline and a direct ternary simulation is not by itself evidence of a new compound or cooperative Ce–Nd mechanism. Such a claim requires species-resolved structural evidence and, for a dynamical mechanism, time-resolved analysis.

This distinction is central to the present research design. Direct ternary PIM-MD results are compared with binary-derived representations only to test whether additional ternary contributions are resolved along the equal-Ce/Nd path. RDFs, separate Ce–Cl and Nd–Cl coordination distributions, shared-chloride topology and temporal persistence are then used to determine whether any departure from binary-like behaviour has a physically identifiable microscopic counterpart.

2.8 Consolidated Research Gap and Implications for the Present Study

The literature establishes a clear but uneven validation landscape. It is strongest for selected binary equilibrium properties and weakest for composition-resolved transport and the target ternary system. The principal evidence and its consequence for the thesis are summarised in Table 2.1.

Four gaps follow from this evidence map. First, no single published dataset provides an internally consistent thermophysical, thermodynamic, structural and transport description of both complete binaries over one common temperature grid. Second, broad-composition viscosity validation is sparse, which makes convergence and transparent uncertainty treatment scientifically important rather than merely procedural. Third, the available literature contains little direct evidence for mixed Ce–Cl–Nd coordination and connectivity, particularly its temporal persistence. Fourth, the target $NaCl-CeCl_3-NdCl_3$ system lacks direct property data over the investigated composition path.

Table 2.1. Literature evidence relevant to the validation and interpretation strategy of the present thesis. "Limited" denotes narrow composition coverage, indirect/derived evidence or incomplete directly reusable data; it does not imply that the property has never been measured.

Property / evidence	**NaCl – $NdCl_3$**	**NaCl – $CeCl_3$**	**Implication for this thesis**
Density and molar volume	Direct experimental basis over composition and temperature	Usable correlations, but weaker primary-source accessibility	Stronger same-system volumetric validation for Nd; Ce comparison is retained with provenance caveat
Excess volume	Direct non-ideal volumetric evidence	More limited direct evidence	Binary non-ideality can be tested; ternary excess volume remains predictive
Mixing enthalpy	Full-range calorimetry at 1124 K	Direct calorimetry, much of it graph based	Both binaries provide energetic validation; ternary mixing enthalpy has no direct experimental anchor
Local structure	Pure-salt XAFS plus rare-earth PIM literature	Pure-salt XAFS plus rare-earth PIM literature	First-shell plausibility can be tested; mixed Ce–Nd network structure is a new simulation result
Viscosity	Broad finite-composition experiment not located	Broad finite-composition experiment not located	Treat primarily as converged model prediction and compare with related actinide/PIM evidence
Thermal conductivity	Selected compositions only	Direct composition-specific measurements available	Ce provides the stronger absolute thermal-conductivity test; Nd and ternary comparisons are more limited
Target ternary	No directly reusable NaCl – $CeCl_3$ – $NdCl_3$ property dataset located		Binary anchoring, uncertainty analysis and species-resolved structure are essential; conclusions are restricted to the investigated equal-Ce/Nd path

3

Theory

3.1 Physical Chemistry of Molten Chloride Salts

Molten salts are dense ionic liquids whose local organisation results from a competition among several interaction classes. Long-range Coulomb attraction between oppositely charged ions produces strong charge ordering, while like-charge repulsion and thermal motion prevent the liquid from collapsing into a static ionic lattice. At short separation, overlap of occupied electron densities produces a steep Pauli repulsion that defines the excluded-volume region and the first-shell distances. Dispersion contributes additional cohesion, and field-induced electronic polarisation becomes increasingly important for diffuse anions and highly charged cations [30, 35]. A useful classical potential must represent the balance among these terms rather than Coulomb attraction alone.

The systems considered here contain monovalent Na^+ together with trivalent lanthanide cations Ln^{3+} ($Ln = Ce, Nd$). Their relevance to nuclear salts arises from comparison with trivalent actinides An^{3+} ($An = U, Pu$), but the notation does not imply chemical identity. Relative to Na^+, a trivalent cation produces a stronger local electric field and competes more strongly for chloride neighbours. Adding $LnCl_3$ to NaCl therefore changes not only the component fractions but also cation–chloride coordination, packing, chloride sharing and intermediate-range connectivity.

Polarizability and *polarisation* describe related but distinct quantities. Polarizability, α_i, is the susceptibility of ion i's electron density to an applied field; polarisation is the induced electronic response, commonly represented by an induced dipole $\boldsymbol{\mu}_i = \alpha_i \mathbf{E}_i$ [30, 36]. Chloride has a diffuse electron density and is strongly polarizable, but the lanthanide cations used in the present PIM also possess finite polarizabilities. The instantaneous response is consequently collective: displacement of one ion changes the local fields, induced dipoles and interactions of several neighbours. This many-body mechanism is absent from a conventional rigid-ion model and is the principal reason that a PIM is preferred for these multivalent chloride melts [15, 30, 35].

Composition controls the populations of sodium-centred, lanthanide-centred and shared chloride environments. At low $LnCl_3$ content, lanthanide coordination shells are more strongly separated by the sodium-chloride-rich liquid. Increasing $LnCl_3$ raises the probability that chloride ions are shared between neighbouring trivalent cations and that connected lanthanide–chloride motifs form. In this sense, NaCl acts not only as a carrier salt but also as a structural modifier that dilutes multivalent-cation connectivity.

Ce and Nd have the same formal charge but are not microscopically identical. The lanthanide contraction gives Nd^{3+} a smaller effective ionic radius than Ce^{3+}, consistent with the shorter Nd–Cl distance measured in the corresponding molten trichloride [14, 37]. Differences in ionic size, polarizability and local field strength can therefore influence coordination and dynamics, while their chemical similarity can still permit approximately interpolative behaviour along parts of the ternary composition line.

Even when the three pure liquids are represented accurately, their mixtures need not be ideal interpolations of the pure components. Mixing changes the relative numbers of unlike neighbours, redistributes chloride between monovalent and trivalent cations and modifies the collective polarisation energy. For a generic molar property Y_{m}, the excess contribution is

$$Y_{\mathrm{m}}^{E} = Y_{\mathrm{m,mix}} - \sum_{i} x_i Y_{\mathrm{m},i}^{\mathrm{pure}}. \tag{3.1}$$

A negative excess molar volume denotes contraction relative to ideal mole-fraction interpolation, whereas a negative mixing enthalpy denotes an enthalpic stabilisation relative to separated pure liquids at the same temperature and pressure. These deviations can arise from the combined effects of packing, chloride redistribution, coordination changes, dispersion and many-body polarisation; no single structural descriptor is expected to encode all contributions.

Temperature broadens ionic-distance and coordination distributions and shortens the lifetime of many local motifs. Diffusion commonly increases and viscosity decreases, although strong lanthanide–chloride association can persist far above the melting range. The interaction hierarchy introduced here therefore provides the physical basis for the PIM, solution-thermodynamic, structural and transport theories developed below.

3.2 Polarizable Ion Model

Classical molecular dynamics represents the ions as particles whose positions evolve under Newton's equations of motion. For ion i,

$$m_i \frac{\mathrm{d}^2 \mathbf{r}_i}{\mathrm{d}t^2} = \mathbf{F}_i, \tag{3.2}$$

where m_i is the ionic mass, $\mathbf{r}_i$ is its position and $\mathbf{F}_i$ is the force acting on it. The force is obtained from the gradient of the total potential energy U,

$$\mathbf{F}_i = -\nabla_i U. \tag{3.3}$$

The predicted structure and dynamics therefore depend directly on the interionic potential used to describe U. In a classical fixed-valence description, the ionic oxidation states remain unchanged and electronic excitations, redox reactions and explicit charge transfer are not represented. Electronic response to the local ionic environment can nevertheless be included through induced dipoles.

3.2.1 From the Rigid-Ion Model to the Polarizable Ion Model

In a rigid-ion model, each ion is assigned a fixed charge and interacts through pairwise electrostatic, repulsive and dispersion contributions. Such models can reproduce some bulk properties, but they assume that the electronic charge distribution of an ion remains unchanged regardless of its local environment.

This approximation is restrictive for multivalent chloride melts. The strong electric fields generated by Ce^{3+} and Nd^{3+} distort the relatively diffuse electronic density of neighbouring Cl^- ions. The resulting induced dipoles modify the effective interaction among several ions simultaneously. Polarisation is therefore a many-body effect and cannot, in general, be represented by a single transferable pair potential [30].

The Polarizable Ion Model (PIM) explicitly includes this electronic response. Its total potential energy is commonly written as

$$U = U_{\mathrm{Coul}} + U_{\mathrm{rep}} + U_{\mathrm{disp}} + U_{\mathrm{pol}}, \tag{3.4}$$

where U_{Coul}, U_{rep}, U_{disp} and U_{pol} denote the Coulomb, short-range repulsion, dispersion and polarisation contributions, respectively.

3.2.2 Coulomb Interaction

The electrostatic interaction between the formal ionic charges is

$$U_{\mathrm{Coul}} = \sum_{i<j} \frac{q_i q_j}{4\pi\varepsilon_0 r_{ij}}, \tag{3.5}$$

where q_i and q_j are the charges of ions i and j, r_{ij} is their separation and ε_0 is the vacuum permittivity. In alternative unit systems, the factor $1/(4\pi\varepsilon_0)$ may be absorbed into the electrostatic unit conversion.

The Coulomb term is attractive for oppositely charged ions and repulsive for ions of equal sign. Because it decays as r^{-1}, it is intrinsically long-ranged and strongly influences both local coordination and collective charge ordering. The use of formal ionic charges is compatible with the PIM because the missing electronic response is represented separately through the induced-dipole contribution.

3.2.3 Short-Range Repulsion

At small interionic separations, overlap between the electronic densities of neighbouring ions produces a steep repulsive interaction associated with the Pauli exclusion principle. A Born–Mayer form is commonly used:

$$U_{\text{rep}} = \sum_{i<j} A_{ij} \exp\left(-a_{ij} r_{ij}\right), \tag{3.6}$$

where A_{ij} is the repulsive energy prefactor and a_{ij} controls the range or steepness of the interaction. The parameters depend on the identities of the interacting species.

This term prevents oppositely charged ions from collapsing under Coulomb attraction and determines the short-distance excluded-volume region. It therefore strongly influences equilibrium cation–anion distances, first-shell radial-distribution-function peaks and the effective size of each ion.

3.2.4 Dispersion Interaction

Dispersion arises from correlated fluctuations of electronic charge density. The leading contributions are commonly represented by inverse-sixth- and inverse-eighth-power terms:

$$U_{\text{disp}} = -\sum_{i<j} \left[f_6^{ij}(r_{ij}) \frac{C_6^{ij}}{r_{ij}^6} + f_8^{ij}(r_{ij}) \frac{C_8^{ij}}{r_{ij}^8} \right], \tag{3.7}$$

where C_6^{ij} and C_8^{ij} are the dipole–dipole and dipole–quadrupole dispersion coefficients, respectively. The functions $f_n^{ij}(r)$ damp the asymptotic inverse-power interactions at short separation, where overlap of the electronic densities invalidates the long-range multipole expansion.

A commonly used Tang–Toennies damping function is

$$f_n^{ij}(r) = 1 - \exp\left(-b_n^{ij} r\right) \sum_{k=0}^{n} \frac{\left(b_n^{ij} r\right)^k}{k!}, \tag{3.8}$$

where b_n^{ij} is a species-dependent damping parameter with dimensions of inverse length. Although dispersion is generally weaker than Coulomb attraction in ionic melts, it contributes to liquid cohesion, density and the transferability of the interaction model.

3.2.5 Induced Dipoles and Polarisation Energy

The local electric field acting on ion i induces a dipole moment,

$$\boldsymbol{\mu}_i = \alpha_i \mathbf{E}_i, \tag{3.9}$$

where α_i is the ionic polarisability and $\mathbf{E}_i$ is the local electric field produced by the surrounding charges and induced dipoles. Because the local field depends on the complete ionic configuration, the induced dipoles are mutually coupled.

The polarisation energy contains charge–dipole interactions, dipole–dipole interactions and the energetic cost of creating each induced dipole. In compact tensor notation,

$$U_{\mathrm{pol}} = \sum_{i<j} \left[q_i \boldsymbol{\mu}_j \cdot \mathbf{T}_{ij}^{(1)} - q_j \boldsymbol{\mu}_i \cdot \mathbf{T}_{ij}^{(1)} - \boldsymbol{\mu}_i \cdot \mathbf{T}_{ij}^{(2)} \cdot \boldsymbol{\mu}_j \right] + \sum_i \frac{|\boldsymbol{\mu}_i|^2}{2\alpha_i}, \tag{3.10}$$

where $\mathbf{T}_{ij}^{(1)}$ and $\mathbf{T}_{ij}^{(2)}$ are the charge–dipole and dipole–dipole interaction tensors. The final term is the dipole self-energy and penalises the creation of an induced dipole.

The induced dipoles correspond to the minimum of the polarisation energy for a fixed ionic configuration,

$$\frac{\partial U_{\mathrm{pol}}}{\partial \boldsymbol{\mu}_i} = \mathbf{0}. \tag{3.11}$$

This condition expresses the adiabatic response of the electronic degrees of freedom to the instantaneous ionic positions. The induced dipoles therefore adjust to changes in coordination and local electric field much faster than the nuclei move.

The many-body character of U_{pol} is important. Moving one ion changes the field acting on several neighbouring ions, alters their dipoles and consequently modifies their interactions with the rest of the system. Polarisation can therefore change coordination geometry, chloride sharing, structural connectivity and ionic mobility even when the formal ionic charges remain fixed.

3.2.6 Short-Range Polarisation Damping

The point-charge expression for the electric field becomes unphysical when ions approach sufficiently closely for their electronic densities to overlap. Without correction, the induced dipole can become excessively large, producing an unphysical over-polarisation or polarisation catastrophe.

Short-range damping is therefore applied to the charge–dipole interaction. The damping accounts approximately for charge penetration and electronic-density overlap, effects that are absent from the idealised point-charge description. A Tang–Toennies-type function may be used to gradually reduce the induction interaction at short distance while recovering the correct asymptotic form at large separation [30].

The damping parameters are species dependent because the degree of electronic overlap differs among Na–Cl, Ce–Cl, Nd–Cl and Cl–Cl pairs. Their physical role is to stabilise realistic first-shell structures without suppressing the long-range response of the induced dipoles.

3.2.7 Parameterisation and Transferability

The parameters of a PIM determine the balance among electrostatics, repulsion, dispersion and induction. Modern polarizable models are commonly developed using electronic-structure calculations, from which forces, dipoles and stresses can be used as reference information. Experimental properties may then provide additional validation of the resulting model.

A distinction must be maintained between parameterisation and validation. Agreement with the data used to determine the parameters does not by itself demonstrate predictive capability. Transferability must be assessed using independent properties, temperatures and compositions.

The rare-earth chloride model used as the theoretical basis for the present systems was developed consistently across several trivalent lanthanide chlorides and their mixtures with NaCl [15]. Such a systematic parameterisation is important for the ternary NaCl-$CeCl_3$-$NdCl_3$ system because Ce and Nd interactions must be represented on a mutually consistent energetic basis.

Nevertheless, transferability is not guaranteed. A model fitted predominantly to pure salts may perform differently when applied to strongly non-ideal mixtures, and a fixed-valence PIM cannot represent oxidation-state changes, chemical reactions or explicit charge transfer. Its validity must therefore be judged for the specific equilibrium, structural and transport properties examined.

For the melts considered in this thesis, the principal advantage of the PIM is that it connects the strong local electric fields of the trivalent cations to the electronic response of chloride. This provides a physically grounded route from ionic interactions to coordination, chloride sharing and collective dynamics, forming the basis for the thermophysical, structural and transport theories introduced in the following sections.

3.3 Thermophysical and Thermodynamic Properties

Thermophysical and energetic properties describe how a molten salt responds to changes in temperature, pressure and composition. They provide complementary information about the packing, mechanical response, thermal storage capacity and energetic stability of the liquid. In molecular systems, these properties may be expressed either as thermodynamic derivatives or, where appropriate, as equilibrium fluctuation relations.

3.3.1 Density and Molar Volume

The mass density of a liquid is defined as

$$\rho = \frac{m}{V}, \tag{3.12}$$

where m is the total mass and V is the volume. For a fluctuating equilibrium volume, the mean density may be expressed using the average volume,

$$\rho = \frac{m}{\langle V \rangle}. \tag{3.13}$$

For a fluctuating NPT trajectory, however, the direct time average $\langle m/V(t) \rangle$ is not algebraically identical to $m/\langle V \rangle$. Equation (3.13) is therefore used here as the thermodynamic mean-volume expression; the exact trajectory estimator adopted for each simulation family is stated explicitly in Section 4.5.1.

Density depends on both the mass of the constituent ions and the volume occupied by the liquid. Consequently, an increase in density with increasing $CeCl_3$ or $NdCl_3$ content does not necessarily indicate more efficient ionic packing, because Ce and Nd are substantially heavier than Na.

The molar volume is

$$V_{\mathrm{m}} = \frac{V}{n}, \tag{3.14}$$

where n is the amount of substance. It may also be written as

$$V_{\mathrm{m}} = \frac{M_{\mathrm{mix}}}{\rho}, \tag{3.15}$$

where M_{mix} is the molar mass of the mixture. Molar volume is particularly useful for analysing compositional changes because it separates the effect of molecular mass from contraction or expansion of the liquid.

3.3.2 Excess Molar Volume

The excess molar volume measures the departure of a mixture from an ideal mole-fraction-weighted interpolation of the pure-component molar volumes. For a binary mixture,

$$V_{\mathrm{m}}^{E} = V_{\mathrm{m,mix}} - \left[x_1 V_{\mathrm{m},1}^{\mathrm{pure}} + x_2 V_{\mathrm{m},2}^{\mathrm{pure}}\right], \tag{3.16}$$

where x_1 and x_2 are the component mole fractions. For a multicomponent mixture,

$$V_{\mathrm{m}}^{E} = V_{\mathrm{m,mix}} - \sum_i x_i V_{\mathrm{m},i}^{\mathrm{pure}}. \tag{3.17}$$

The pure-component quantities must refer to the same temperature and pressure as the mixture. A negative excess molar volume indicates contraction relative to ideal interpolation, whereas a positive value indicates expansion. Contraction may arise from electrostriction, coordination rearrangement or more efficient occupation of the available volume. It should not be interpreted solely as improved packing without corresponding structural evidence.

3.3.3 Thermal Expansion

The volumetric thermal-expansion coefficient is defined as

$$\alpha_V = \frac{1}{V}\left(\frac{\partial V}{\partial T}\right)_P. \tag{3.18}$$

An equivalent expression in terms of density is

$$\alpha_V = -\frac{1}{\rho}\left(\frac{\partial \rho}{\partial T}\right)_P. \tag{3.19}$$

The coefficient α_V has units of K^{-1} and represents the fractional change in volume per unit increase in temperature at constant pressure. In molten salts, thermal expansion reflects the anharmonicity of the effective ionic interactions and the increased configurational space accessed at higher temperature.

Within the isothermal–isobaric ensemble, thermal expansion may also be related to the covariance of volume and enthalpy:

$$\alpha_V = \frac{\langle VH \rangle - \langle V \rangle \langle H \rangle}{k_{\mathrm{B}} T^2 \langle V \rangle}, \tag{3.20}$$

where H is the enthalpy and k_{B} is the Boltzmann constant. This relation shows that thermal expansion is connected to correlated fluctuations of volume and enthalpy.

3.3.4 Compressibility and Sound Speed

The isothermal compressibility is

$$\kappa_T = -\frac{1}{V}\left(\frac{\partial V}{\partial P}\right)_T. \tag{3.21}$$

It measures the fractional volume change produced by a pressure change at constant temperature and has units of Pa^{-1}. The inverse of the isothermal compressibility is the isothermal bulk modulus,

$$K_T = \frac{1}{\kappa_T}. \tag{3.22}$$

In the isothermal–isobaric ensemble, κ_T is related to equilibrium volume fluctuations:

$$\kappa_T = \frac{\langle V^2 \rangle - \langle V \rangle^2}{k_{\mathrm{B}} T \langle V \rangle}. \tag{3.23}$$

A more compressible liquid exhibits larger equilibrium volume fluctuations, whereas a mechanically stiffer liquid exhibits smaller fluctuations.

The adiabatic compressibility is defined as

$$\kappa_S = -\frac{1}{V}\left(\frac{\partial V}{\partial P}\right)_S, \tag{3.24}$$

where the derivative is evaluated at constant entropy. The isothermal and adiabatic compressibilities are related through

$$\frac{\kappa_S}{\kappa_T} = \frac{C_V}{C_P}. \tag{3.25}$$

Because heat exchange is absent during an adiabatic compression, κ_S is generally smaller than κ_T.

The adiabatic speed of sound is

$$v_s = \frac{1}{\sqrt{\rho \kappa_S}}, \tag{3.26}$$

where v_s is expressed in $\mathrm{m\,s}^{-1}$. The sound speed characterises the propagation of small adiabatic pressure disturbances through the liquid and links the mechanical response of the melt to its density. It is also used later in the structural-coherence description of thermal conductivity.

3.3.5 Heat Capacity

Heat capacity quantifies the amount of energy required to increase the temperature of a system. The constant-volume heat capacity is defined as

$$C_V = \left(\frac{\partial U}{\partial T} \right)_V , \tag{3.27}$$

where U is the internal energy. The constant-pressure heat capacity is

$$C_P = \left(\frac{\partial H}{\partial T} \right)_P , \tag{3.28}$$

where

$$H = U + PV. \tag{3.29}$$

In the canonical ensemble, the constant-volume heat capacity is related to internal-energy fluctuations:

$$C_V = \frac{\langle U^2 \rangle - \langle U \rangle^2}{k_\mathrm{B} T^2}. \tag{3.30}$$

Similarly, in the isothermal–isobaric ensemble, the constant-pressure heat capacity is related to enthalpy fluctuations:

$$C_P = \frac{\langle H^2 \rangle - \langle H \rangle^2}{k_\mathrm{B} T^2}. \tag{3.31}$$

These expressions refer to the total heat capacity of the simulated system. Division by the amount of substance gives the molar heat capacity, while division by the total mass gives the mass-specific heat capacity.

The molar heat capacity is commonly expressed in $\mathrm{J\,mol^{-1}\,K^{-1}}$, whereas the mass-specific heat capacity is expressed in $\mathrm{J\,kg^{-1}\,K^{-1}}$. The volumetric heat capacity may be obtained from

$$C_{P,\mathrm{vol}} = \rho c_P, \tag{3.32}$$

where c_P is the mass-specific heat capacity. Equivalently,

$$C_{P,\mathrm{vol}} = \frac{C_{P,\mathrm{m}}}{V_\mathrm{m}}, \tag{3.33}$$

where $C_{P,\mathrm{m}}$ is the molar heat capacity. Volumetric heat capacity represents the amount of thermal energy stored per unit volume and is therefore important in thermal-transport analysis.

3.3.6 Mixing Enthalpy

The enthalpy of mixing measures the energetic change associated with forming a mixture from its pure components at the same temperature and pressure. For a binary system,

$$\Delta H_{\text{mix}} = H_{\text{mix}} - [x_1 H_1^{\text{pure}} + x_2 H_2^{\text{pure}}]\,. \tag{3.34}$$

For a multicomponent system,

$$\Delta H_{\text{mix}} = H_{\text{mix}} - \sum_i x_i H_i^{\text{pure}}. \tag{3.35}$$

A negative mixing enthalpy indicates that the mixed liquid is energetically more stable than the ideal pure-component reference. In molten NaCl – MCl_3 systems, such stabilisation may arise from favourable unlike-ion interactions, chloride redistribution, polarisation and changes in local coordination. A positive value indicates energetically unfavourable mixing.

The composition at which the minimum occurs need not be equimolar because the strength of non-ideality depends on the balance among chloride availability, cation charge asymmetry, packing and structural connectivity. Mixing enthalpy is a bulk thermodynamic difference between the mixture and pure-component reference states. It contains the net change in Coulomb, repulsive, dispersion and polarisation energies over all ionic environments, together with the pressure–volume contribution. By contrast, one RDF peak reports only one pairwise spatial correlation over a limited radial interval. A change in its height or position can therefore support a structural interpretation, but it cannot uniquely determine either the sign or magnitude of ΔH_{mix} [30, 38].

3.3.7 Excess Heat Capacity

The excess constant-pressure heat capacity is defined as

$$C_P^E = C_{P,\text{mix}} - \sum_i x_i C_{P,i}^{\text{pure}}. \tag{3.36}$$

It quantifies the deviation of the mixture heat capacity from ideal mole-fraction-weighted interpolation. The excess heat capacity may be related to the temperature dependence of the excess enthalpy:

$$C_P^E = \left(\frac{\partial H^E}{\partial T}\right)_P. \tag{3.37}$$

A non-zero excess heat capacity therefore indicates that the enthalpic non-ideality of the mixture changes with temperature. When $C_P^E > 0$, H^E increases with temperature: a negative excess enthalpy becomes less negative, or a positive excess enthalpy becomes more positive. When $C_P^E < 0$, H^E decreases with temperature: a positive excess enthalpy becomes less positive, or a negative excess enthalpy becomes more negative. The sign of C_P^E thus describes the temperature derivative of mixing non-ideality and does not, by itself, establish whether mixing is favourable at a selected temperature [39, 40].

3.4 Structural Characterisation

The properties of molten salts depend not only on their overall composition, but also on how the constituent ions are organised at local and intermediate length scales. In multivalent chloride

melts, particularly important features include rare-earth–chloride coordination, the distribution of coordination states and the formation of chloride-mediated connections between neighbouring rare-earth cations. These structural features may be described using radial distribution functions, coordination numbers, free-energy-like pair correlations and connectivity-based measures.

3.4.1 Radial Distribution Functions

The partial radial distribution function $g_{ij}(r)$ describes the spatial correlation between ions of species i and j. It is defined as the probability of finding an ion of species j at a distance r from a reference ion of species i, relative to the probability expected for a spatially uniform distribution at the same bulk number density. For an isotropic multicomponent liquid, it may be written schematically as

$$g_{ij}(r) = \frac{1}{4\pi r^2 \rho_j} \left\langle \frac{1}{N_i} \sum_{a \in i} \sum_{\substack{b \in j \\ b \neq a}} \delta\left(r - r_{ab}\right) \right\rangle, \tag{3.38}$$

where N_i is the number of ions of species i, ρ_j is the bulk number density of species j, r_{ab} is the separation between ions a and b, and δ is the Dirac delta function. The angular brackets denote an equilibrium average.

For an ideal spatially uncorrelated distribution,

$$g_{ij}(r) = 1. \tag{3.39}$$

Values greater than unity indicate an enhanced probability of finding the pair at separation r, whereas values below unity indicate depletion. At very short separation, $g_{ij}(r)$ approaches zero because overlap repulsion prevents the ions from occupying the same region of space.

The position of the first maximum identifies the most probable nearest-neighbour separation. Its height indicates the degree of spatial ordering, while its width reflects the distribution of instantaneous interionic distances. The first minimum separates the first coordination shell approximately from the surrounding liquid. Subsequent peaks describe ordering at larger distances, including packing effects and connectivity between neighbouring coordination environments.

The interpretation of peak height requires caution. A higher first peak does not necessarily correspond to a larger number of neighbours because the coordination population also depends on the peak width, species number density and radial integration range.

3.4.2 Coordination Numbers and Their Distributions

The cumulative coordination number of species j surrounding species i within a radius r is obtained from

$$N_{ij}(r) = 4\pi\rho_j \int_0^r g_{ij}(r')\, r'^2 \, \mathrm{d}r'. \tag{3.40}$$

When evaluated at the first minimum $r_{\min}$ of the corresponding RDF,

$$N_{ij} = 4\pi\rho_j \int_0^{r_{\min}} g_{ij}(r)\, r^2\, \mathrm{d}r, \tag{3.41}$$

the result represents the mean number of ions of species j in the first coordination shell around species i.

Because molten salts are dynamically disordered, the coordination number of an individual ion fluctuates with time. The ensemble-averaged value is therefore generally non-integer and should not be interpreted as a fixed molecular stoichiometry. Furthermore, the mean alone does not describe the complete coordination environment. Two liquids may possess the same average coordination number while having different proportions of six-, seven-, eight- or higher-coordinate cations.

The coordination-number probability distribution may be written as

$$P_i(n) = \left\langle \frac{N_i^{(n)}}{N_i} \right\rangle, \tag{3.42}$$

where $N_i^{(n)}$ is the number of ions of species i having instantaneous coordination number n. The mean coordination number is then

$$\langle \mathrm{CN}_i \rangle = \sum_n n P_i(n). \tag{3.43}$$

The breadth of $P_i(n)$ quantifies structural heterogeneity and the coexistence of different local environments. Polarizable simulations of trivalent rare-earth chlorides have shown broad coordination distributions, commonly spanning approximately six- to nine-fold environments, rather than a single rigid coordination state [15].

The numerical value of a coordination number depends on the definition of the first coordination shell. Consequently, comparisons between systems require a consistent physical definition of the coordination boundary. The exact selection applied in this work is described in the methodology chapter.

3.4.3 Potential of Mean Force

The radial distribution function may also be expressed as a pair potential of mean force,

$$W_{ij}(r) = -k_{\mathrm{B}} T \ln g_{ij}(r), \tag{3.44}$$

where $W_{ij}(r)$ has units of energy per interacting pair, k_{B} is the Boltzmann constant and T is the absolute temperature. For molar quantities, multiplication by the Avogadro constant converts the result to energy per mole.

The potential of mean force represents the reversible free-energy change associated with bringing two selected ions to separation r, while all remaining degrees of freedom are averaged over. A minimum in $W_{ij}(r)$ corresponds to a statistically preferred separation, while a maximum or barrier corresponds to a less probable region separating structural states.

The potential of mean force is not identical to the pair interaction appearing in the force field. It includes the collective influence of the surrounding liquid, including screening, packing, polarisation and many-body structural reorganisation. It is also defined only up to an additive constant. A convenient reference is therefore commonly chosen such that

$$\lim_{r\to\infty} W_{ij}(r) = 0, \tag{3.45}$$

provided that the RDF approaches unity at sufficiently large separation.

3.4.4 Chloride Sharing and Structural Speciation

The coordination shells of neighbouring rare-earth cations may become connected when they contain one or more common chloride ions. A chloride associated with only one rare-earth coordination environment may be described as terminal, whereas a chloride associated with two or more rare-earth cations acts as a bridge.

The topology of two connected coordination polyhedra can be classified by the number of shared chloride ions:

- one shared chloride corresponds to corner sharing;
- two shared chlorides correspond to edge sharing;
- three shared chlorides correspond to face sharing.

These definitions are geometric and do not imply permanent chemical bonds. The coordination shells fluctuate continuously, and chloride ions may enter, leave or move between neighbouring environments. Corner-, edge- and face-sharing configurations should therefore be interpreted as instantaneous or statistically populated structural motifs. In the operational analysis of this thesis, configurations sharing three or more chlorides are grouped into a single face/higher-order category; the exact counting rule is given in Section 4.5.7.

Connectivity also provides a basis for describing the size of rare-earth-centred aggregates. A rare-earth coordination environment that does not share chloride with another rare-earth cation may be described as monomer-like. Two connected rare-earth centres form a dimer-like motif, while three connected centres form a trimer-like motif. Larger connected components may be described as oligomeric, polymeric or network-like.

The term *speciation* must be used cautiously in a molten liquid. These motifs are not necessarily discrete molecular species with permanent stoichiometry. They represent a statistical distribution of dynamically interconverting coordination environments. Accordingly, structural speciation should be discussed together with the underlying geometric definition and, where available, information about the persistence of the identified motifs.

Recent polarizable-model calculations for molten rare-earth chlorides found that neighbouring rare-earth coordination environments are connected predominantly through corner- and edge-sharing configurations [15]. The degree of connectivity decreases upon dilution with NaCl, consistent with the role of the alkali chloride as a structural modifier separating rare-earth-centred environments.

3.4.5 Temporal Persistence of Structural Motifs

Static coordination and chloride-sharing populations describe how frequently a motif occurs, but not how long it survives or whether it reforms after a short interruption. This distinction is important for transport because two liquids can have similar time-averaged connectivity while differing substantially in the rate at which their local networks rearrange. Studies of alkali–trivalent halide mixtures have linked the relaxation of the first coordination shell and the evolving trivalent-cation network to the shear-relaxation time of the liquid [33].

Two complementary notions of persistence are useful. *Continuous* persistence requires a contact or shared-chloride linkage to remain present without interruption over the lag interval. It therefore probes the lifetime of an uninterrupted local configuration. *Intermittent* persistence asks whether the same contact or linked pair is present again after a lag time and allows temporary breakage and reformation. Intermittent persistence can therefore be much longer than continuous persistence in a liquid whose local coordination is labile but recurrent.

The comparison between these measures separates two physically different limits. Long continuous persistence indicates locally long-lived configurations. A much larger intermittent than continuous timescale indicates that configurations break readily but re-form repeatedly, so the network is recurrent without being mechanically frozen. Likewise, a high rate of changes between corner-, edge- and face-sharing states can coexist with persistent rare-earth–rare-earth connectivity if a linked pair changes the number of shared chlorides without becoming fully disconnected. These temporal descriptors are therefore interpreted together with coordination and connectivity populations rather than as independent proof of a transport mechanism. The exact indicators, time windows and finite-lag estimators used in this thesis are defined in Section 4.5.10.

3.4.6 Intermediate-Range Order

Local coordination describes the nearest-neighbour environment of an ion, whereas intermediate-range order refers to correlations extending across several coordination shells. In multivalent chloride melts, such organisation may arise from chloride-mediated connections between neighbouring rare-earth-centred coordination environments.

Rare-earth–rare-earth radial distribution functions contain information about the characteristic separation between neighbouring coordination centres. However, these functions alone do not determine whether two rare-earth cations are connected through one or more shared chloride ions. Intermediate-range organisation is therefore interpreted by combining cation–anion coordination, cation–cation correlations and chloride-sharing topology.

In diffraction experiments, intermediate-range order may appear as a prepeak or first sharp diffraction peak at a wave number below the principal nearest-neighbour peak. Such features have been reported in molten trivalent chlorides and associated with extended cation correlations and connected coordination environments [41, 42].

3.5 Transport Properties

Transport properties describe the irreversible transfer of momentum and thermal energy through the liquid. Unlike equilibrium thermodynamic properties, they depend on the temporal relaxation

of spontaneous microscopic fluctuations. Within linear-response theory, the corresponding macroscopic transport coefficients can be related to equilibrium time-correlation functions. In the present work, the principal transport properties are shear viscosity and thermal conductivity.

3.5.1 Shear Viscosity

Shear viscosity quantifies the resistance of a liquid to deformation under an applied shear stress. At the macroscopic level, a Newtonian liquid obeys

$$\tau_{\alpha\beta} = \eta \left(\frac{\partial v_\alpha}{\partial x_\beta} + \frac{\partial v_\beta}{\partial x_\alpha} \right), \qquad \alpha \neq \beta, \tag{3.46}$$

where $\tau_{\alpha\beta}$ is the off-diagonal shear stress and η is the dynamic shear viscosity. For simple shear in which the reciprocal velocity gradient vanishes, this reduces to the familiar $\tau_{\alpha\beta} = \eta\, \partial v_\alpha / \partial x_\beta$ form. The SI unit of η is $\mathrm{Pa\,s}$.

From a microscopic perspective, viscosity represents the transport and relaxation of transverse momentum. Spontaneous fluctuations of the off-diagonal components of the microscopic stress tensor occur even in an equilibrium liquid. The Green–Kubo relation connects the persistence of these fluctuations to the shear viscosity:

$$\eta = \frac{V}{k_\mathrm{B} T} \int_0^\infty \langle P_{\alpha\beta}(0) P_{\alpha\beta}(t) \rangle \, \mathrm{d}t, \qquad \alpha \neq \beta, \tag{3.47}$$

where V is the system volume, T is the absolute temperature, k_B is the Boltzmann constant and $P_{\alpha\beta}$ is an off-diagonal component of the microscopic stress tensor. The quantity

$$C_{\alpha\beta}(t) = \langle P_{\alpha\beta}(0) P_{\alpha\beta}(t) \rangle \tag{3.48}$$

is the stress autocorrelation function. It measures how long the liquid retains memory of an instantaneous shear-stress fluctuation [43].

For comparable stress-fluctuation amplitudes, more rapidly decaying stress correlations generally contribute a smaller Green–Kubo integral, whereas more persistent correlations contribute a larger one. The viscosity depends on both the magnitude and the temporal decay of the stress autocorrelation function. The formal upper integration limit in Equation (3.47) is infinite because complete loss of stress memory is assumed in the long-time limit.

In multivalent chloride melts, viscosity is influenced by more than the motion of individual ions. Rare-earth–chloride coordination, chloride sharing and the persistence of connected structural motifs can restrict independent ionic motion and increase the degree of cooperative rearrangement required for flow. More persistent or extensive connectivity may therefore slow stress relaxation. However, average coordination number alone does not determine viscosity, because the lifetimes, topology and collective dynamics of the coordination environments are also important.

Increasing temperature generally increases the rate of structural rearrangement and reduces the persistence of stress fluctuations, leading to a decrease in viscosity. Composition can produce non-linear behaviour when the addition of $CeCl_3$ or $NdCl_3$ changes the balance between isolated coordination environments and chloride-linked structures.

Because viscosity depends on an integral of a decaying correlation function, it is generally more statistically demanding than properties obtained from simple equilibrium averages. The theoretical relation is given here, whereas the treatment of stress components, convergence and the finite integration interval is described in the methodology chapter.

3.5.2 Thermal Conductivity

Thermal conductivity quantifies the ability of a material to transport thermal energy in response to a temperature gradient. At the macroscopic level, Fourier's law is

$$\mathbf{q} = -\lambda \nabla T, \tag{3.49}$$

where $\mathbf{q}$ is the heat-flux density, ∇T is the temperature gradient and λ is the thermal conductivity. The negative sign indicates that heat flows from high to low temperature. The SI unit of thermal conductivity is $\mathrm{W\,m^{-1}\,K^{-1}}$.

Within equilibrium linear-response theory, thermal conductivity is formally related to fluctuations of the microscopic heat current through the Green–Kubo relation [44]:

$$\lambda = \frac{1}{3 V k_{\mathrm{B}} T^2} \int_0^\infty \langle \mathbf{J}_Q(0) \cdot \mathbf{J}_Q(t) \rangle \, \mathrm{d}t, \tag{3.50}$$

where $\mathbf{J}_Q$ is the microscopic heat current and the factor $1/3$ accounts for averaging over the three Cartesian directions of an isotropic liquid.

A direct evaluation of Equation (3.50) was not performed in the present work because the required microscopic heat-current time series was not generated by the production simulations. Thermal conductivity was instead estimated using the structural-coherence model described below.

Structural-Coherence Model

An alternative liquid-state description relates thermal conductivity to the ability of the liquid to store thermal energy, the characteristic propagation speed of collective disturbances and the distance over which structural correlations remain coherent. The structural-coherence model is written as

$$\lambda = \frac{1}{3} C_{P,\mathrm{vol}} v_s \ell_{\mathrm{sc}}, \tag{3.51}$$

where $C_{P,\mathrm{vol}}$ is the volumetric heat capacity at constant pressure, v_s is the adiabatic speed of sound and ℓ_{sc} is the structural coherence length [45].

The volumetric heat capacity describes the quantity of thermal energy that can be stored per unit volume and temperature change. The sound speed represents a characteristic velocity for the propagation of small collective disturbances through the melt. The structural coherence length represents the effective distance over which such disturbances retain coherence before being disrupted by structural disorder.

The factor $1/3$ is analogous to the isotropic projection factor appearing in kinetic descriptions of transport. Dimensional consistency follows from

$$[C_{P,\mathrm{vol}} v_s \ell_{\mathrm{sc}}] = \frac{\mathrm{J}}{\mathrm{m}^3\,\mathrm{K}} \frac{\mathrm{m}}{\mathrm{s}} \mathrm{m} = \frac{\mathrm{W}}{\mathrm{m}\,\mathrm{K}}. \tag{3.52}$$

The structural coherence length is informed by the spatial decay of pair-correlation oscillations and is interpreted within the model as an effective mean free path for collective energy carriers. This creates a direct link between equilibrium liquid structure and thermal transport:

$$\text{pair correlations} \longrightarrow \ell_{\mathrm{sc}} \longrightarrow \lambda. \tag{3.53}$$

The structural-coherence relation is not an exact Green–Kubo identity. Instead, it is a physically interpretable liquid-state model that summarises complex microscopic energy-transfer processes through an effective heat capacity, propagation velocity and coherence length. The formal statistical-mechanical definition remains the heat-current Green–Kubo relation in Equation (3.50).

For multicomponent melts, chemical and structural disorder can modify ℓ_{sc} even when density and heat capacity are similar. Accordingly, the model provides a means of interpreting differences between the binary NaCl – $CeCl_3$ and NaCl – $NdCl_3$ systems and the ternary NaCl – $CeCl_3$ – $NdCl_3$ melt in terms of their underlying liquid structure.

4

Methodology

4.1 Computational Workflow

A shared overall workflow was applied to the binary $NaCl - CeCl_3$ and $NaCl - NdCl_3$ systems and to the selected $NaCl - CeCl_3 - NdCl_3$ ternary compositions. Here, "shared" denotes the same sequence of system construction, NPT sampling, NVT sampling and post-processing; it does not imply that every property used an identical retained window or uncertainty estimator. Charge-neutral, composition-specific PIM cells were prepared for constant-pressure equilibration. Each state point was then simulated in the NPT ensemble to establish its equilibrium volume and generate thermophysical and energetic time series. The corresponding mean NPT volume was subsequently assigned to a fixed-volume NVT production run for structural and transport analyses.

Direct trajectory-derived quantities were distinguished from fitted or model-based quantities. Density, molar volume, enthalpy, heat capacity and compressibility-related quantities were obtained principally from NPT outputs. Structural properties were obtained from NVT trajectories, and viscosity was evaluated from NVT stress-tensor fluctuations. Thermal conductivity was estimated with the structural-coherence model by combining NPT-derived thermophysical inputs with RDF-derived structural information. Redlich–Kister and Molecular Interaction Volume Model calculations were applied during post-processing and were not treated as direct MD observations.

The simulated systems, interaction model, simulation protocol, property calculations, thermodynamic models, statistical treatment and validation hierarchy are described in Sections 4.2 to 4.7.

4.2 Simulated Systems and Compositions

The complete binary $NaCl - CeCl_3$ and $NaCl - NdCl_3$ composition ranges and an equal-Ce/Nd composition line through the ternary $NaCl - CeCl_3 - NdCl_3$ system were investigated. Each state point contained 2000 ions. This size provided many independent local coordination environments while

retaining sufficiently fine integer composition resolution and making a 124-state PIM campaign computationally tractable. It was therefore a physics–cost compromise rather than the outcome of a separate finite-size scaling study; finite-size effects remain part of the model uncertainty.

The common grid $T = 900$, 1000, 1100 and 1200 K overlaps the temperature range of the available rare-earth-chloride property literature and provides four evenly spaced points for thermal slopes and regression diagnostics. The 100 K spacing is wide enough to resolve temperature trends relative to sampling noise while preserving a compact common grid across all compositions. Homogeneous liquid trajectories were analysed at every state point; low-temperature rare-earth-rich states below the equilibrium liquidus are consequently interpreted as metastable liquid extensions rather than phase-stability predictions [22, 27, 31].

4.2.1 Composition Definition

Compositions were defined on a salt-formula-unit basis. Because each component contains one cation per formula unit, the component mole fractions were obtained directly from the cation populations:

$$N_{\mathrm{cat}} = N_{\mathrm{Na}} + N_{\mathrm{Ce}} + N_{\mathrm{Nd}}, \qquad (x_{\mathrm{NaCl}}, x_{\mathrm{CeCl_3}}, x_{\mathrm{NdCl_3}}) = \frac{(N_{\mathrm{Na}}, N_{\mathrm{Ce}}, N_{\mathrm{Nd}})}{N_{\mathrm{cat}}}. \tag{4.1}$$

Species absent from a given binary system were assigned a population of zero, and charge neutrality required:

$$N_{\mathrm{Cl}} = N_{\mathrm{Na}} + 3N_{\mathrm{Ce}} + 3N_{\mathrm{Nd}}. \tag{4.2}$$

The fixed cell size and integer populations prevented some nominal compositions from being represented exactly. Realised mole fractions calculated from `runtime.inpt` and `data.inpt` were therefore used in all thermodynamic calculations, while nominal values were retained for state-point names and prescribed-grid comparisons. The exact integer populations and realised compositions are preserved in the archived input and post-processing tables.

4.2.2 Composition and State-Point Grids

Binary Systems

For both binary systems,

$$x(\mathrm{MCl_3}) = 0.0,\ 0.1,\ 0.2, \ldots, 0.9,\ 1.0, \qquad M \in \{\mathrm{Ce}, \mathrm{Nd}\}. \tag{4.3}$$

The endpoints corresponded to pure NaCl and pure MCl_3; each binary grid therefore contained 11 compositions and 44 composition–temperature state points.

Ternary Composition Line

The ternary calculations followed

$$x_{\mathrm{CeCl_3}} = x_{\mathrm{NdCl_3}} = \frac{1 - x_{\mathrm{NaCl}}}{2}, \tag{4.4}$$

with $x_{\mathrm{NaCl}} = 0.10,\ 0.20, \ldots, 0.90$. The Ce-to-Nd salt ratio was therefore unity throughout the series. This nine-point pseudo-binary line did not constitute complete sampling of the ternary composition triangle.

Table 4.1. Composition and temperature coverage. Realised mole fractions derived from the integer cation populations were used in calculations.

System	Nominal composition grid	Temperatures / K	Points	States
$NaCl - CeCl_3$	$x_{CeCl_3} = 0.0$–1.0, increment 0.1	900, 1000, 1100, 1200	11	44
$NaCl - NdCl_3$	$x_{NdCl_3} = 0.0$–1.0, increment 0.1	900, 1000, 1100, 1200	11	44
$NaCl - CeCl_3 - NdCl_3$	$x_{NaCl} = 0.10$–0.90, $x_{CeCl_3} = x_{NdCl_3}$	900, 1000, 1100, 1200	9	36
Total	—	—	**31**	**124**

4.3 Molecular-Dynamics Model and Implementation

4.3.1 Polarizable Ion Model and Parameterisation

All simulations used a fixed-valence Polarizable Ion Model comprising formal charge–charge interactions, Born–Mayer repulsion, damped dispersion and many-body polarisation through induced ionic dipoles. The governing equations and physical interpretation are given in Chapter 3.

The published single-species and $NaCl - MCl_3$ parameters were taken from the DFT-derived rare-earth-chloride parameterisation of Goloviznina et al. [15] and were retained without composition-, temperature- or ensemble-dependent refitting. The binary $NaCl - CeCl_3$ and $NaCl - NdCl_3$ subsets were combined for the ternary system; the additional Ce – Nd cross interaction described below was therefore treated as a modelling assumption.

Table 4.2. Ionic properties used in the Polarizable Ion Model.

Species	Mass / u	Charge / e	Polarizability / a.u.
Na^+	22.989	$+1$	0.900
Cl^-	35.453	-1	20.000
Ce^{3+}	140.12	$+3$	7.874
Nd^{3+}	144.24	$+3$	6.619

All species were mobile and retained their formal oxidation states. Electronic response was represented through induced dipoles, but redox reactions, explicit charge transfer and changes in oxidation state were outside the model.

For the ternary system, the Ce – Nd cross parameters supplied to MetalWalls were

$$(\alpha, B, C_6, C_8, b_6, b_8) = (3.000, 0.000, 40.928, 85.8035, 1.500, 1.000)$$

in MetalWalls atomic units. The mixed dispersion coefficients were defined by

$$C_n^{\mathrm{Ce-Nd}} = \frac{C_n^{\mathrm{Ce-Ce}} + C_n^{\mathrm{Nd-Nd}}}{2}, \qquad n \in \{6, 8\}. \tag{4.5}$$

The remaining cross parameters were assigned exactly as listed in the ternary input files and were not fitted to ternary measurements. Equation (4.5) is an arithmetic average; it is therefore reported explicitly rather than being labelled generically as a geometric Lorentz–Berthelot rule. Because Ce^{3+} and Nd^{3+} are chemically similar and their binary trichloride mixture is expected to be close to ideal, the assignment was treated as a controlled interpolation. Its residual effect was not propagated as a formal state-point uncertainty and was instead assessed through smooth ternary trends, physical admissibility and consistency with the binary limits. Complete pair and damping parameters remain in the archived inputs.

4.3.2 Induced Dipoles, Electrostatics and Software

Induced dipoles were minimised at every MD step using the MetalWalls conjugate-gradient solver with a tolerance of 10^{-7} in internal units. Maximum iteration limits of 100 and 1000 were used according to the archived production input. Three-dimensional periodic boundary conditions were applied, and long-range electrostatics were evaluated with the periodic Coulomb implementation in MetalWalls. The principal numerical settings are listed in Table 4.3.

Table 4.3. Principal numerical settings used for the interaction model.

Setting	Value
Boundary conditions	Three-dimensional periodic
Dipole minimisation	Conjugate gradient, tolerance 1.0×10^{-7}
Maximum dipole iterations	100 or 1000, according to the production input
Coulomb real-space cutoff	22.677 bohr $\approx$ 12.0 Å
Coulomb real-space tolerance	1.63×10^{-5}
Coulomb reciprocal-space tolerance	1.0×10^{-7}
Fumi–Tosi cutoff	22.677 bohr $\approx$ 12.0 Å

The simulations represented homogeneous bulk liquids without walls, electrodes or liquid–vacuum interfaces and were run with MetalWalls on the DelftBlue high-performance computing system. Pair coefficients, damping parameters, species properties and numerical solver settings were read directly from the archived production inputs rather than reconstructed from rounded values in the thesis tables. The tables therefore summarise the calculation, while the input archive remains the authoritative reproducibility record. MetalWalls atomic units were converted during post-processing. The interaction parameters and dipole treatment were unchanged between NPT and NVT stages; only the thermodynamic constraints and production settings changed. The complete `runtime.inpt`, `data.inpt` and restart files were retained for reproducibility.

4.4 Simulation Protocol

Composition-specific preparation inputs supplied the initial coordinates, velocities and box estimates used to initiate the NPT simulations. No data from this preparation stage entered the reported properties.

4.4.1 Integration Settings and Simulation Stages

All simulations used a timestep of 20.670687 atomic units (≈ 0.5 fs). Temperature was controlled with a thermostat chain of length five, relaxation time 20670.687 atomic units (≈ 0.5 ps), iteration tolerance 10^{-17}, and maximum iteration count 100. NPT simulations used a barostat chain of length five, target pressure 3.3988276×10^{-9} atomic units (≈ 1 bar), and relaxation time 103353.433 atomic units (≈ 2.5 ps); the barostat was disabled for NVT production.

Table 4.4. Simulation stages and principal analysis roles.

Stage	Ensemble	Length	Principal analysis role
Constant-pressure production	NPT	1,000,000 steps (500 ps)	Equilibrium volume, density, volume, enthalpy, heat capacity and compressibility inputs.
Standard fixed-volume production	NVT	1,400,000 steps (700 ps)	RDF, coordination and connectivity analyses.
Extended fixed-volume production	NVT	10,000,000 steps (5 ns)	Viscosity and long-time structural convergence checks for the corresponding production families.

Every reported value was linked to a specific system, realised composition, temperature, ensemble, trajectory file and retained interval. The 700 ps NVT series supplied the standard structural dataset, whereas the exact 5 ns NVT series supplied viscosity and selected long-time structural checks. This source mapping prevented outputs from one ensemble or production length from being substituted silently for another.

For the standard 700 ps structural trajectories, the first 400,000 MD steps (200 ps) were excluded and the final 1,000,000 steps (500 ps) were used for RDF, coordination and connectivity calculations. The extended trajectories were analysed using the property-specific retained intervals described below.

4.4.2 NPT-to-NVT State Preparation

A separate NPT simulation was performed for each composition and temperature. The final NPT restart, `restart.2.out`, was copied to `data.inpt`; its coordinates and velocities were retained. The fixed NVT volume was obtained only after the NPT volume series had reached a stable late-time region. For this state-transfer operation, `box_parameters.out` was averaged over $500{,}000 \leq n_{\mathrm{step}} \leq 1{,}000{,}000$:

$$\langle V \rangle = \frac{1}{N_{\mathrm{prod}}} \sum_{i=1}^{N_{\mathrm{prod}}} V_i, \qquad L_x = L_y = L_z = \langle V \rangle^{1/3}. \tag{4.6}$$

Only the box dimensions were replaced; the ionic coordinates were not rescaled. They were interpreted under the reassigned periodic cell, and the periodic image convention was used for coordinates outside the new primary box. The reassignment was followed by checks of the initial energy, pressure, temperature and minimum interionic separations. Any transient associated with the new fixed volume was excluded before structural or transport analysis. Thus, the fixed-volume trajectory was treated as a continuous run with post-processed equilibration removal rather than as five nanoseconds of automatically accepted data. The NVT input retained the matching timestep, thermostat, interaction and dipole settings, while the barostat was removed.

4.4.3 Output Sampling and Run Acceptance

The principal extended-NVT output intervals are given in Table 4.5.

Table 4.5. Principal output intervals used in the extended NVT simulations.

Output	$NaCl-NdCl_3$	$NaCl-CeCl_3$	Ternary	Use
Coordinate trajectory	100	100	10000	Extended structural / temporal analysis
Box parameters	100	100	100	Fixed-cell verification
Energies	100	100	100	Stability and equilibration
Temperature	1000	1000	100	Thermostat diagnostic
Pressure	100	100	100	Fixed-volume diagnostic
Stress tensor	10	10	10	Green–Kubo viscosity

The output frequencies were selected according to the observable and storage cost. In the extended binary runs, coordinates, energies, box dimensions and pressure were written every 100 steps (50 fs); temperature was written more coarsely as a thermostat diagnostic. The ternary 5 ns coordinate trajectory used for the temporal-persistence analysis contained 1001 frames, corresponding to 10000 MD steps (approximately 5 ps) between saved frames; other scalar ternary diagnostics were written more frequently as listed in Table 4.5. The stress tensor was written every 10 MD steps, corresponding to a sampling interval of 5 fs, to provide high-frequency resolution of the stress fluctuations used in the Green–Kubo and spectral analyses. Sensitivity to still finer stress-sampling intervals was not evaluated separately. The different output intervals therefore reflect analysis requirements rather than different MD timesteps.

4.5 Calculation of Molecular-Dynamics Properties

Properties were evaluated from the retained portions of the corresponding NPT or NVT trajectories. Realised compositions were defined by Equation (4.1). Because each salt component contains one cation per formula unit,

$$N_{\mathrm{salt}} = N_{\mathrm{Na}} + N_{\mathrm{Ce}} + N_{\mathrm{Nd}}, \tag{4.7}$$

with absent species assigned zero population.

4.5.1 Density

For a cell of constant mass,

$$m_{\text{cell}} = \frac{1}{N_{\text{A}}} \sum_s N_s M_s, \tag{4.8}$$

$$\rho(t) = \frac{m_{\text{cell}}}{V_{\text{cell}}(t)}, \tag{4.9}$$

where N_s and M_s are the population and molar mass of species s. An initial non-production interval was excluded before any density or volume average was evaluated. The precise stationarity treatment was family-specific because the three post-processing workflows were developed and verified at different stages of the project.

For NaCl – $NdCl_3$, the retained start was selected separately for every composition–temperature state using statistical inefficiency, effective sample size, residual-trend, alternative-cutoff and split-half diagnostics. Density was then the direct average of $\rho(t)$ over the accepted interval. For NaCl – $CeCl_3$, the first 1000 saved box records were removed uniformly and the direct average of the remaining instantaneous densities was used. For the ternary system, the first 10% of each volume series was removed and the principal density estimator was $m_{\text{cell}}/\langle V \rangle$, with the mean instantaneous density retained as a numerical check. Applying one predefined late-time rule to all Ce or ternary states avoided selecting favourable windows composition by composition. The complete family-specific verification is reported in Section A.2.

Same-system experimental correlations formed the primary density benchmark. For NaCl – $NdCl_3$, the measurements of Mochinaga and Igarashi [18], as compiled by Janz [46], were converted from t in °C to T in kelvin:

$$\rho(T) = (a - 0.27315b) + b \times 10^{-3} T. \tag{4.10}$$

For NaCl – $CeCl_3$, the composition-dependent correlations tabulated by Iwadate and attributed therein to Sato and Yamamura were written as

$$\rho(T) = A - BT, \tag{4.11}$$

with the composition-dependent coefficients and validity intervals taken from Iwadate [31].

Experimental points remained at their reported compositions in figures. For numerical deviations only, interior PIM-MD values were evaluated with a shape-preserving piecewise cubic Hermite interpolant at each temperature [47]; no composition extrapolation was performed. In-range and temperature-extrapolated reference values were identified separately. Generic deviation metrics are defined in Section 4.7.5.

4.5.2 Molar Volume

The instantaneous molar volume corresponding to a simulation cell is

$$V_m(t) = \frac{N_{\text{A}} V_{\text{cell}}(t)}{N_{\text{salt}}}. \tag{4.12}$$

When V_{cell} is expressed in $\mathrm{\AA}^3$, the conversion to $\mathrm{cm^3\,mol^{-1}}$ is

$$V_m(t) = \frac{10^{-24} N_{\mathrm{A}} V_{\mathrm{cell}}(t)}{N_{\mathrm{salt}}}. \tag{4.13}$$

The estimator followed the verified workflow for each family. For NaCl – $NdCl_3$, $V_m(t)$ was averaged directly over the same state-specific stationary interval used for density and was independently checked against

$$V_m = \frac{M_{\mathrm{mix}}}{\rho}, \qquad M_{\mathrm{mix}} = \sum_i x_i M_i. \tag{4.14}$$

The maximum discrepancy between the two Nd estimators was 0.0096%. The NaCl – $CeCl_3$ workflow calculated V_m from $M_{\mathrm{mix}}/\overline{\rho}$, whereas the ternary workflow used the retained mean cell volume and Equation (4.12). These choices are stated explicitly so that numerical agreement is not mistaken for identical post-processing.

For the correlation-aware Nd analysis, the state-point standard error s_j used in inverse-variance weighting was defined as

$$s_j = \max(s_{\mathrm{ACF},j}, s_{\mathrm{block},j}), \tag{4.15}$$

where $s_{\mathrm{ACF},j}$ is the standard error corrected using the statistical inefficiency of the retained series and $s_{\mathrm{block},j}$ is the standard error of contiguous block means. The four simulated values at each Nd composition were then fitted by

$$V_m(T) = \beta_0 + \beta_1 T, \qquad w_j = 1/s_j^2. \tag{4.16}$$

The fitted-parameter covariance was propagated to the prediction interval. A comparison at 1073.15 K was interpolative, whereas 1273.15 K was treated explicitly as extrapolative. Ce and ternary comparisons retained the uncertainty definition and fitting strategy of their documented workflows rather than being relabelled as the Nd correlation-aware estimator. Supporting definitions and checks are tabulated in Section A.2.

4.5.3 Excess Molar Volume

Excess molar volume was defined relative to pure-liquid references evaluated at the same temperature:

$$V_m^E(\boldsymbol{x}, T) = V_m(\boldsymbol{x}, T) - \sum_{i=1}^{N_c} x_i V_{m,i}^0(T). \tag{4.17}$$

For a binary NaCl – MCl_3 mixture,

$$V_m^E(x, T) = V_m(x, T) - \left[(1-x)V_{m,\mathrm{NaCl}}^0(T) + xV_{m,\mathrm{MCl_3}}^0(T)\right]. \tag{4.18}$$

Realised mole fractions were used, and pure endpoints were zero by construction.

Because the same pure-component references enter several interior compositions, excess values can share endpoint uncertainty. In matrix form,

$$\boldsymbol{V}^E = \boldsymbol{A}\boldsymbol{V}, \qquad \boldsymbol{\Sigma}_{V^E} = \boldsymbol{A}\boldsymbol{\Sigma}_V\boldsymbol{A}^{\mathsf{T}}. \tag{4.19}$$

This full covariance propagation was implemented for the Nd analysis and used in its generalized-least-squares Redlich–Kister fits. The Ce notebook used a fixed-order unweighted binary fit, and the ternary notebook used a fixed-order ordinary-least-squares/Muggianu representation. These descriptive fits were not presented as though they shared the Nd covariance or model-selection procedure. Direct state-point values remained the primary evidence, and near-zero excess values were compared in absolute rather than percentage terms. The fit-specific distinction is retained in Sections A.2 and 4.6.1.

4.5.4 Molar Enthalpy and Direct Mixing Enthalpy

Energy observations in `energies.out` were matched by MD step to `box_parameters.out`. The physical ionic energy excluded the auxiliary extended-system Hamiltonian:

$$E_{\mathrm{phys}}(t) = E_{\mathrm{kin}}(t) + E_{\mathrm{pot}}(t). \tag{4.20}$$

The instantaneous molar enthalpy was

$$H_m(t) = \frac{E_{\mathrm{phys}}(t) + P_{\mathrm{ext}} V(t)}{N_{\mathrm{salt}}} C_{\mathrm{E_h}}, \tag{4.21}$$

with

$$C_{\mathrm{E_h}} = 2.625499640 \times 10^6\,\mathrm{J\,mol^{-1}\,E_h^{-1}}. \tag{4.22}$$

The imposed external pressure was used in the PV term, and the resulting enthalpy was expressed per mole of salt formula units.

After removal of the non-stationary NPT interval, the retained observations were averaged as

$$\overline{H}_m(\boldsymbol{x}, T) = \frac{1}{N_{\mathrm{p}}} \sum_{k=1}^{N_{\mathrm{p}}} H_m(t_k). \tag{4.23}$$

Energy and volume records were aligned before averaging, and the same state-point procedure was applied to mixtures and pure-component references. Stationarity was evaluated jointly for energy, volume and the derived enthalpy, because an apparently stable energy series can still yield a drifting enthalpy if the volume has not equilibrated. The accepted interval and its alternatives were retained in the analysis report for each simulation family. Direct mixing enthalpy was then calculated as

$$\Delta H_{\mathrm{mix}}(\boldsymbol{x}, T) = \overline{H}_m(\boldsymbol{x}, T) - \sum_i x_i \overline{H}^{\,0}_{m,i}(T), \tag{4.24}$$

using pure-component simulations at the same temperature and pressure. For a binary system this becomes

$$\Delta H_{\mathrm{mix}}(x, T) = \overline{H}_m(x, T) - (1-x)\overline{H}_m^{\mathrm{NaCl}}(T) - x\overline{H}_m^{\mathrm{MCl_3}}(T). \tag{4.25}$$

The endpoints were imposed as exact zero constraints. Uncertainty propagation is given in Section 4.7.2. Same-system literature mixing-enthalpy data were used where available. The independently parameterised PMF-informed MIVM in Section 4.6.2 was treated as a structure-to-energetics

consistency test, whereas the benchmark-calibrated binary MIVM was treated as a semi-empirical reproduction of its calibration data rather than as independent experimental validation.

4.5.5 Isobaric Heat Capacity

At each composition, production-average enthalpies were obtained at 900, 1000, 1100 and 1200 K. The production fraction was selected separately for each simulation family and then applied uniformly to all of its compositions and temperatures. For NaCl – $CeCl_3$, the final 50% was retained after comparison with the final 60% and state-level trend diagnostics; all 44 state points were adequate and the largest 50–60% shift was 0.999 combined standard errors. For NaCl – $NdCl_3$, candidate retained fractions of 40, 50, 60 and 70% were compared, and the final 60% was the earliest common interval for which all 44 states passed the adopted stationarity checks. The ternary analysis likewise used the final 60%, after comparison with the final 50% and an automatic statistical-inefficiency estimate; no state exceeded a two-standard-error shift. These are property- and family-specific choices rather than universal MD discard fractions. The supporting diagnostics are given in Section A.3.

The measured production-average temperature was used in the regression. A direct temperature series was available for both binary archives. It was absent from the assembled ternary heat-capacity archive, so the ternary temperature was reconstructed from the kinetic energy as

$$T(t) = \frac{2E_{\mathrm{kin}}(t)}{(3N-3)k_{\mathrm{B}}}, \tag{4.26}$$

assuming removal of the three centre-of-mass translational degrees of freedom and no additional constraints [48]. The thermostat target was retained as a sensitivity check but was not substituted silently for the measured mean temperature.

The interval-average heat capacity was the ordinary-least-squares slope

$$\overline{H}_m(T) = a + C_p T, \tag{4.27}$$

consistent with $C_p = (\partial H_m/\partial T)_P$ [39, 40]. Inverse-variance weighted, nominal-temperature, leave-one-temperature-out and quadratic fits were all calculated as sensitivity diagnostics. With only four temperatures, the quadratic fit was not promoted to the production model merely because it reduced the residual. The reported C_p is therefore the linear 900–1200 K interval slope, with bootstrap uncertainty as defined in Section 4.7.2. Literature comparisons were made only when the reference definition and temperature interval were compatible.

4.5.6 Excess Isobaric Heat Capacity

Excess heat capacity was calculated with the same interval-average definition for mixture and pure-component values:

$$C_p^E = C_p^{\mathrm{mix}} - \sum_i x_i C_{p,i}^{\mathrm{pure}}. \tag{4.28}$$

For the binary systems,

$$C_p^E(x) = C_p^{\mathrm{mix}}(x) - (1-x)C_p^{\mathrm{NaCl}} - xC_p^{\mathrm{MCl_3}}. \tag{4.29}$$

Realised mole fractions were used. For each binary system, the same pure-component bootstrap realisations were reused for every interior composition. This preserved the covariance introduced by shared endpoints and gave $C_p^E = 0$ at the pure limits in every replicate. For the ternary path, the mixture-slope distribution was combined with the pure-component distributions defined by the validated binary means and bootstrap standard errors; common pure-component draws were reused across all ternary compositions. The complete procedure and its remaining distributional assumption are specified in Section 4.7.2.

The directly calculated C_p^E values remained the primary results. Descriptive composition-space fits are given in Section 4.6.3. Where direct experimental C_p^E data were unavailable, assessment was based on consistency with the underlying C_p values, endpoint constraints, uncertainty and smooth composition trends rather than an unsupported claim of direct validation.

4.5.7 Radial Distribution Functions, Coordination Numbers and Rare-Earth Speciation

Partial RDFs were calculated from the coordinates stored in `trajectories.xyz` using MDAnalysis [49, 50]. The cubic box dimensions read from the matching `data.inpt` file were assigned to each frame. For the standard 700 ps structural series, the first 200 ps were discarded and the final 500 ps were analysed. Binary correlations included M – Cl, M – M, Na – Cl, Na – Na, Na – M and Cl – Cl, where M = Ce or Nd; ternary analysis additionally resolved Ce – Cl, Nd – Cl, Ce – Ce, Ce – Nd and Nd – Nd. Six hundred radial bins were used over $0.1\ \text{Å} \le r \le L/2 - 1\ \text{Å}$. The first minimum after the principal metal–chloride peak defined the first-shell cutoff [33, 51].

For rare-earth ion i, the instantaneous chloride coordination number was

$$\mathrm{CN}_i^{\mathrm{M-Cl}}(t) = \sum_{j \in \mathrm{Cl}} H\left(r_c^{\mathrm{M-Cl}} - r_{ij}^{\mathrm{MI}}(t)\right), \tag{4.30}$$

where r_{ij}^{MI} is the minimum-image separation and

$$H(y) = \begin{cases} 1, & y \ge 0, \\ 0, & y < 0. \end{cases} \tag{4.31}$$

Thus each chloride inside the first-shell cutoff contributes exactly one. Mean coordination numbers and integer-state populations were averaged over the retained trajectory; separate Ce – Cl and Nd – Cl cutoffs were used in the ternary melts.

Rare-earth ions were represented as vertices of an undirected graph and were connected when they shared at least one chloride neighbour. Connected components were classified as

$$\begin{aligned} &N_M = 1 : \text{monomer}, \quad && N_M = 2 : \text{dimer}, \\ &N_M = 3 : \text{trimer}, && N_M \ge 4 : \text{larger connected cluster}. \end{aligned} \tag{4.32}$$

Ternary clusters were additionally labelled Ce-only, Nd-only or mixed. Cluster populations were normalised by the number of rare-earth ions, not the number of connected components. For compact presentation in the Results chapter, the $N_M \ge 4$ category is referred to as the polymer or polymeric

fraction. One, two or at least three shared chloride neighbours were reported as corner-, edge- or face-sharing *proxies*, respectively:

$$N_{\mathrm{Cl}}^{\mathrm{shared}} = 1,\ 2,\ \geq 3. \tag{4.33}$$

These are shared-neighbour topological descriptors and do not prove exact polyhedral geometry or permanent molecular species. For the ternary melts, shared-chloride links were additionally separated into Ce – Ce, Ce – Nd and Nd – Nd pair classes. To assess whether the equal-Ce/Nd network showed preferential association, the observed pair fractions were compared descriptively with the random-pair expectation. For cation fractions p_{Ce} and p_{Nd}, the large-population random probabilities are

$$P_{\mathrm{Ce-Ce}} = p_{\mathrm{Ce}}^2, \qquad P_{\mathrm{Ce-Nd}} = 2p_{\mathrm{Ce}}p_{\mathrm{Nd}}, \qquad P_{\mathrm{Nd-Nd}} = p_{\mathrm{Nd}}^2. \tag{4.34}$$

Thus the equal-Ce/Nd path has the reference ratio 25:50:25. This comparison was treated as a descriptive mixing diagnostic because the linkage fractions do not carry independent-replica uncertainties.

Graph analysis used NetworkX [52]; interpretation followed prior molten-salt structural studies [34, 53, 54]. Convergence and population uncertainty are described in Section 4.7.3.

4.5.8 Thermal Conductivity from the Structural-Coherence Model

A direct Green–Kubo thermal-conductivity calculation requires the microscopic heat-current time series and integration of its equilibrium autocorrelation function [55]. That observable was not generated by the MetalWalls production runs used here. Moreover, the heat-current expression requires dedicated implementation and validation for a polarizable, multicomponent interaction model rather than uncritical reuse of a simple pair-potential expression [56, 57]. Thermal conductivity was therefore estimated using the structural-coherence model of Numbers et al. [45], for which all required thermophysical and RDF inputs were available:

$$\lambda = \frac{1}{3} C_{p,\mathrm{vol}} v_s \ell_{\mathrm{sc}}. \tag{4.35}$$

Here $C_{p,\mathrm{vol}}$ is volumetric isobaric heat capacity, v_s is adiabatic sound speed and ℓ_{sc} is an RDF-informed effective coherence length. The resulting values are reported as structural-coherence model estimates, not direct Green–Kubo PIM-MD coefficients.

The workflow was initially established for NaCl – $CeCl_3$ using a uniform 20% trajectory discard. This was an operational production-window choice, applied identically to all 44 Ce states. As the analysis matured, the same 20% convention was applied to NaCl – $NdCl_3$ and the ternary system and was then subjected to a more rigorous numerical sensitivity study: the complete thermophysical calculation was repeated after discarding 10, 20, 30 and 40% of each trajectory, and the compressibility calculation was additionally repeated with 4, 5, 8 and 10 contiguous blocks. This progression—initial operational choice, evidence gained from the first application, and later systematic sensitivity verification—is documented in Section A.4.

For the primary 20% discard,

$$\kappa_T = \frac{\langle V^2 \rangle - \langle V \rangle^2}{k_{\mathrm{B}} T \langle V \rangle}, \tag{4.36}$$

$$C_{p,\mathrm{vol}} = \frac{C_{p,m}}{V_m}, \qquad \alpha_V = \frac{\partial \ln V_m}{\partial T}, \tag{4.37}$$

$$\kappa_S = \kappa_T - \frac{\alpha_V^2 T}{C_{p,\mathrm{vol}}}, \qquad v_s = (\rho \kappa_S)^{-1/2}. \tag{4.38}$$

The $C_{p,m}$ and α_V inputs are interval-average slopes over 900–1200 K, whereas density, molar volume and κ_T are state-point quantities. Sampling variability in κ_T was assessed from five contiguous blocks [58]. State points with $\kappa_S \leq 0$ were rejected because they imply a non-physical sound speed within this post-processing route.

The Na – Cl and M – Cl RDFs were smoothed with an 11-point, third-order Savitzky–Golay filter [59]. Smoothing was used only to stabilise automated identification of the first peak and following minimum. The calculation was repeated using the raw RDF and 11-, 21- and 31-point smoothing windows; the resulting coherence-length range was retained as a numerical sensitivity diagnostic in Section A.4. Following the published formalism,

$$\beta(r) = \sum_k \frac{b_k(r)}{1 - b_k(r)}, \qquad S(r) = \exp\left[- \int_0^r \beta(r')\, \mathrm{d}r' \right], \qquad \ell_{\mathrm{sc},i} = \int S_i(r)\, \mathrm{d}r. \tag{4.39}$$

The first cation–anion peak was searched within 1.5–4.0 Å, followed by its first minimum. For the binary systems, the composition-weighted coherence length used in post-processing was

$$\ell_{\mathrm{sc}} = (1 - x_{\mathrm{MCl_3}}) \ell_{\mathrm{Na-Cl}} + x_{\mathrm{MCl_3}} \ell_{\mathrm{M-Cl}}. \tag{4.40}$$

For the ternary path, the post-processing retained the separate Na – Cl, Ce – Cl and Nd – Cl coherence contributions and combined them using the realised salt-component fractions,

$$\ell_{\mathrm{sc}}^{\mathrm{tern}} = x_{\mathrm{NaCl}} \ell_{\mathrm{Na-Cl}} + x_{\mathrm{CeCl_3}} \ell_{\mathrm{Ce-Cl}} + x_{\mathrm{NdCl_3}} \ell_{\mathrm{Nd-Cl}}. \tag{4.41}$$

The effective ternary value was therefore assembled from species-resolved cation–chloride structural information rather than treating Ce and Nd as one indistinguishable cation type. This weighting step is part of the SCM construction and is not a heat-current Green–Kubo calculation. The NPT-derived $C_{p,\mathrm{vol}}$ and v_s tables and the NVT-derived ℓ_{sc} table were merged by system, temperature and realised composition after conversion to SI units. A state was retained only when all three inputs were finite and $\kappa_S > 0$. Benchmarking therefore assessed the structural-coherence route and its inputs, not an unperformed heat-current calculation.

4.5.9 Shear Viscosity

Viscosity was calculated from the 5 ns fixed-volume NVT stress series using the Green–Kubo formalism. The stress tensor was written every ten steps, giving

$$\Delta t_\sigma = 10 \times 0.5\ \mathrm{fs} = 5\ \mathrm{fs}. \tag{4.42}$$

The step sequence in `stress_tensor.out` was checked for missing, duplicated and non-monotonic records and against the requested final step. Retained intervals were selected from temperature, energy and stress stationarity rather than a universal discarded fraction.

The three off-diagonal components were mean-centred,

$$\delta P_{\alpha\beta}(t) = P_{\alpha\beta}(t) - \langle P_{\alpha\beta} \rangle, \qquad \alpha\beta \in \{xy, xz, yz\}, \tag{4.43}$$

so that a residual finite-trajectory offset could not generate a spurious non-decaying ACF contribution. Their overlapping-origin autocorrelation functions were evaluated by FFT following the standard time-correlation approach for molecular-dynamics data [60]:

$$C_{\alpha\beta}(k\Delta t_\sigma) = \frac{1}{N-k} \sum_{i=0}^{N-k-1} \delta P_{\alpha\beta}(i\Delta t_\sigma) \delta P_{\alpha\beta}[(i+k)\Delta t_\sigma]. \tag{4.44}$$

Normalized ACFs,

$$\rho_{\alpha\beta}(t) = \frac{C_{\alpha\beta}(t)}{C_{\alpha\beta}(0)}, \tag{4.45}$$

were retained only to compare relaxation rates; they were not integrated because normalization removes the stress-fluctuation magnitude. For an isotropic liquid,

$$C_\eta(t) = \frac{C_{xy}(t) + C_{xz}(t) + C_{yz}(t)}{3}, \tag{4.46}$$

and

$$\eta(t) = \frac{V}{k_\mathrm{B}\overline{T}} \int_0^t C_\eta(t')\, \mathrm{d}t'. \tag{4.47}$$

The integral was evaluated by the trapezoidal rule after SI conversion. Component-wise running integrals were also calculated. The three components were used as isotropy and sampling diagnostics, not as independent replicates. At long lag times the number of available time origins decreases, so residual noise can drive the running integral even after the physical ACF has decayed. Conversely, truncating before complete decay can underestimate viscosity. Accordingly, no visually selected point or automatic first-zero-crossing cutoff was used [61, 62].

The stress-current series was additionally analysed by cepstral spectral estimation in SporTran [63, 64], following the rare-earth-chloride PIM-MD approach of Goloviznina et al. [15]. This procedure estimates the zero-frequency spectral limit and is less sensitive than direct integration to the noisy long-time ACF tail. The complete-trajectory cepstral result was the principal estimate, while direct Green–Kubo integrals remained physical and convergence diagnostics. Convergence and uncertainty are specified in Section 4.7.4.

External viscosity assessment was separated into same-system experimental validation and lanthanide–actinide simulant benchmarking. For the pure rare-earth trichlorides, the dynamic-viscosity correlations measured by Potapov and Sato [65] were used as the same-system references. Their reported experimental ranges are 1090–1177 K for $CeCl_3$ and 1025–1151 K for $NdCl_3$. The 1100 K $CeCl_3$ comparison therefore lies inside the measured range. For $NdCl_3$, the reportable 1000 K state was compared with a short 25 K extrapolation of the published correlation; the 1100 K simulation was not promoted to primary validation evidence because that state did not satisfy the

adopted convergence criteria. Such endpoint comparisons test the absolute viscosity of the pure trichlorides and were not interpreted as experimental validation of the complete binary composition curves.

Property-specific actinide comparisons used the NaCl – UCl_3 and NaCl – $PuCl_3$ PIM-MD results supplied by Ter Veer et al. [66] at $x(\mathrm{AnCl_3}) = 0.37$. Because the present binary grids were simulated in increments of 0.10 in trichloride mole fraction, the corresponding lanthanide value was obtained locally from the two bracketing reportable states,

$$\eta_{0.37} = 0.30\,\eta_{0.30} + 0.70\,\eta_{0.40}. \tag{4.48}$$

Assuming independent simulation estimates at the two bracketing compositions, the propagated statistical uncertainty was

$$\sigma_{0.37} = \sqrt{(0.30\,\sigma_{0.30})^2 + (0.70\,\sigma_{0.40})^2}. \tag{4.49}$$

This propagation quantifies the reported statistical uncertainty of the two simulation estimates but does not include model-form uncertainty associated with the local linear interpolation. A matched-composition comparison was retained only when both bracketing lanthanide states satisfied the reporting criteria. Consequently, the primary Ce/U comparison uses 900, 1000 and 1200 K, whereas the Nd/Pu comparison uses 1000, 1100 and 1200 K. Relative differences were defined as

$$\delta_\eta = 100\,\frac{\eta_{\mathrm{Ln}} - \eta_{\mathrm{ref}}}{\eta_{\mathrm{ref}}}, \tag{4.50}$$

and the mean absolute relative difference (MARD) was used only as a compact descriptive summary across the retained temperatures. Where uncertainties for both the lanthanide and actinide estimates were available, and treating the two estimates as independent, the standard uncertainty of their difference was obtained using the law of propagation of uncertainty [67]. The benchmark difference was then normalised by this combined reported uncertainty as

$$z_\eta = \frac{\eta_{\mathrm{Ln}} - \eta_{\mathrm{An}}}{\sqrt{\sigma_{\mathrm{Ln}}^2 + \sigma_{\mathrm{An}}^2}}, \tag{4.51}$$

where the denominator is the root-sum-of-squares combined standard uncertainty for two independent estimates. Values of $|z_\eta| \geq 2$ were used only as a descriptive indication that the difference is large relative to the combined reported statistical uncertainty; no formal hypothesis test was inferred from this threshold.

As an additional published actinide check, the 63:37 mol% NaCl – UCl_3 rolling-ball measurements of Termini et al. [68] were compared with the interpolated 900 K NaCl – $CeCl_3$ result. Three reported measurements clustered summarised by their arithmetic mean and sample standard deviation for this single matched-composition comparison. Temperature and composition trends were otherwise interpreted jointly with the structural analysis rather than treated as proof of model validity.

4.5.10 Temporal Persistence of Chloride-Mediated Connectivity

Time-resolved structural analyses were used to distinguish the population of a coordination or linkage motif from its lifetime and recurrence. For a binary indicator $h(t)$ that equals one when a selected contact or shared-chloride linkage is present and zero otherwise, the intermittent persistence function was evaluated as

$$C_{\mathrm{int}}(t) = \frac{\langle h(0)h(t)\rangle}{\langle h(0)\rangle}, \tag{4.52}$$

so that temporary loss and later reformation of the same contact or linked pair were permitted. The continuous function used an uninterrupted-survival indicator $H(t)$,

$$C_{\mathrm{cont}}(t) = \frac{\langle h(0)H(t)\rangle}{\langle h(0)\rangle}, \tag{4.53}$$

where $H(t) = 1$ only when the motif remained present continuously from the time origin to lag t. The characteristic persistence time was obtained by linear interpolation at $C(t) = e^{-1}$. Continuous and intermittent quantities were interpreted together: the former measures uninterrupted survival, whereas the latter additionally captures recurrence after short-lived breakage.

For NaCl – $NdCl_3$, a dedicated 900 K analysis was performed for $x(NdCl_3) = 0.60$, 0.70, 0.80, 0.90 and 1.00. Each exact 5 ns trajectory contained 100001 saved coordinate frames at 0.05 ps spacing. The primary repeated-window interval was 0.2–4.7 ns and was partitioned into nine sequential, non-overlapping 0.5 ns windows. A composition-specific Nd–Cl cutoff from the accepted first-minimum RDF analysis was held fixed across all windows. Two Nd ions were linked when they shared at least one chloride; one, two and three-or-more shared chlorides defined corner-, edge- and face/higher-order states, respectively. Continuous and intermittent Nd–Cl contacts, any Nd–Nd shared-chloride linkage, topology-resolved linkage states and linkage transition rates were evaluated to a maximum lag of 250 ps. Formation, breaking and topology-switching rates were normalised by elapsed time and the number of Nd ions.

The nine Nd windows are sequential blocks from one trajectory and were not interpreted as independent simulation replicas. Their across-window standard deviations and standard errors are therefore descriptive measures of temporal variability. All continuous and intermittent $1/e$ crossings were reached for the reported primary metrics. Finite-lag integrals of the intermittent functions were retained only as secondary diagnostics because many remained partial at 250 ps. The accepted RDF coordination number was also audited against the window-resolved contact analysis; the observed systematic offset was retained as a limitation rather than silently reconciled.

A corresponding Ce-rich analysis was performed at 900 K for $x(CeCl_3) = 0.60$–1.00 using sequential 0.5 ns windows of the exact 5 ns trajectories. Composition-specific Ce–Cl first-shell cutoffs were retained across the windows, and continuous Ce–Cl contact and Ce–Ce shared-chloride linkage persistence were evaluated. As for the Nd analysis, the across-window variation is a within-trajectory stability measure rather than a between-replica uncertainty.

The final ternary persistence workflow used the available 900 and 1000 K 5 ns trajectories for $x(LnCl_3) = 0.40$–0.90, where $x(LnCl_3) = x(CeCl_3) + x(NdCl_3)$ and $x(CeCl_3) = x(NdCl_3)$. Each trajectory contained 1001 saved frames separated by approximately 5 ps. Temporal stability was assessed using five non-overlapping 1 ns blocks, with persistence functions evaluated to a

maximum lag of 500 ps. Continuous and intermittent Ce–Cl–Ce, Ce–Cl–Nd and Nd–Cl–Nd bridge persistence were assessed. “Continuous” therefore means continuously present at the saved-frame resolution; breakage and reformation occurring between two saved frames cannot be resolved. The five blocks belong to one trajectory, so their variation is a within-trajectory stability diagnostic and not replica-derived uncertainty. Finite-window integrals are described as integrated persistence times rather than complete infinite-time lifetimes.

These temporal analyses were used to test whether the static connectivity trends have a dynamical counterpart. They were not treated as independent proof that a particular linkage lifetime causes the macroscopic viscosity or thermal-conductivity response; causal interpretation requires consistency with the stress or energy-transport relaxation itself [33].

4.6 Thermodynamic Modelling

4.6.1 Binary Redlich–Kister Representation

At each temperature, binary excess molar volume was represented by

$$V_m^E(x,T) = x(1-x)\sum_{k=0}^{n} A_k(T)(2x-1)^k, \tag{4.54}$$

where $x = x(\mathrm{MCl_3})$, $A_k(T)$ are temperature-specific coefficients, and the $x(1-x)$ prefactor enforces the pure-component limits [69]. The statistical treatment followed the verified workflow for each dataset rather than imposing one common regression procedure retrospectively.

For NaCl – $NdCl_3$, the shared pure-component references generate covariance between the interior excess-volume values. This covariance was propagated from the molar-volume estimates and used in the generalized-least-squares fit,

$$\widehat{\boldsymbol{A}} = \left(\boldsymbol{X}^{\mathsf{T}}\boldsymbol{\Sigma}_{V^E}^{-1}\boldsymbol{X}\right)^{-1}\boldsymbol{X}^{\mathsf{T}}\boldsymbol{\Sigma}_{V^E}^{-1}\boldsymbol{V}^E. \tag{4.55}$$

Candidate orders were compared using the small-sample corrected Akaike information criterion, leave-one-composition-out prediction and numerical conditioning [70, 71].

For NaCl – $CeCl_3$, the verified notebook used a predefined three-coefficient, unweighted Redlich–Kister representation. The ternary excess-volume workflow used fixed-order ordinary least squares for its binary descriptions before symmetric Muggianu interpolation. These fits are therefore reported as descriptive composition-space representations; the original PIM-MD points and their state-point uncertainties remain the primary evidence. Fitted extrema, zero crossings and polynomial-order dependence are model features and are not interpreted as direct molecular-dynamics sampling uncertainty. The complete system-specific fitting choices are summarised in Section A.2.

4.6.2 PMF-Informed and Benchmark-Calibrated Molecular Interaction Volume Models

The Molecular Interaction Volume Model (MIVM) was used in two deliberately separate ways. First, an *PMF-informed* variant was constructed from PIM–MD structural and volumetric descriptors without fitting to mixing enthalpy. This variant tests whether information extracted from the

simulated liquid structure is sufficient to reproduce the sign, curvature and magnitude of ΔH_{mix}. Second, for the two binary systems only, a *benchmark-calibrated* variant retained the PIM–MD coordination and molar-volume inputs but adjusted the two directional interaction parameters against same-system calorimetric mixing enthalpies. The latter is therefore a semi-empirical representation and was not treated as an independent prediction. This distinction follows the hybrid simulation–calorimetry logic of Goncharov et al. [72], while the underlying MIVM formulation originates from Tao [73].

For either binary, component 1 denotes the rare-earth trichloride and component 2 denotes NaCl,

$$1 = \mathrm{MCl_3}, \qquad 2 = \mathrm{NaCl}, \qquad \mathrm{M} = \mathrm{Ce\ or\ Nd}. \tag{4.56}$$

At the selected temperature, the structural and volumetric inputs were Z_1, Z_2, $V_{m,1}$, $V_{m,2}$, B_{12} and B_{21}. The effective coordination inputs were mapped from the cation–cation RDFs as

$$Z_1 = Z_{\mathrm{M-M}}, \qquad Z_2 = Z_{\mathrm{Na-Na}}, \tag{4.57}$$

with

$$Z_{ij} = 4\pi\rho_j \int_0^{r_{\min,ij}} g_{ij}(r) r^2 \, \mathrm{d}r. \tag{4.58}$$

The pure-component molar volumes were taken from Section 4.5.2 at the corresponding temperature.

The molar potential of mean force was calculated as

$$w_{ij}(r) = -RT \ln\left[\frac{g_{ij}(r)}{g_{ij,\infty}}\right], \tag{4.59}$$

where $g_{ij,\infty}$ was the mean over the final 10% of the RDF grid. The PMF is a state-dependent free-energy descriptor and was not interpreted as a transferable bare pair potential. RDFs were smoothed with a 21-point, third-order Savitzky–Golay filter. The first physically resolved cation–cation maximum was located on the smoothed RDF, and the PMF value at that position was used as the effective interaction energy. Raw and smoothed RDF/PMF profiles were compared to ensure that smoothing did not materially shift the extracted feature.

For the binary component convention in Equation (4.56),

$$\varepsilon_{11} = w_{\mathrm{M-M}}\left(r^{\mathrm{peak}}_{\mathrm{M-M}}\right), \tag{4.60}$$

$$\varepsilon_{22} = w_{\mathrm{Na-Na}}\left(r^{\mathrm{peak}}_{\mathrm{Na-Na}}\right), \tag{4.61}$$

$$\varepsilon_{12} = \varepsilon_{21} = w_{\mathrm{Na-M}}\left(r^{\mathrm{peak}}_{\mathrm{Na-M}}\right). \tag{4.62}$$

The treatment of the unlike-pair PMF followed the verified workflow of each binary rather than imposing a common retrospective choice. For NaCl – $NdCl_3$, $x(\mathrm{NdCl_3}) = 0.20$ was the predefined operational reference and the other interior compositions were used as a sensitivity check. For NaCl – $CeCl_3$, the Na–Ce PMF minimum was extracted at every available interior composition and the mean of those mixed-composition ε_{12} values was used for the reported PMF-informed curve; the value nearest $x(\mathrm{CeCl_3}) = 0.50$ was retained as a comparison diagnostic. Thus the PMF-informed curves contain no fitted calorimetric interaction parameter.

The directional MIVM parameters were then

$$B_{12} = \exp\left[-\frac{\varepsilon_{12} - \varepsilon_{22}}{RT}\right], \tag{4.63}$$

$$B_{21} = \exp\left[-\frac{\varepsilon_{12} - \varepsilon_{11}}{RT}\right], \tag{4.64}$$

with

$$B_{11} = B_{22} = 1. \tag{4.65}$$

Because the PMF and the coordination environment vary with composition, B_{12} and B_{21} are effective model descriptors rather than universal force-field parameters.

For the binary systems, the mixing enthalpy was evaluated as

$$\begin{aligned}\frac{\Delta H_{\mathrm{mix}}^{\mathrm{MIVM}}}{RT} = \frac{1}{2}\sum_{i=1}^{2} Z_i x_i \Bigg[&\left(\frac{\sum_{j=1}^{2} x_j B_{ji} \ln B_{ji}}{\sum_{j=1}^{2} x_j B_{ji}}\right)^2 \\ &- \frac{\sum_{j=1}^{2} (1 + \ln B_{ji}) x_j B_{ji} \ln B_{ji}}{\sum_{j=1}^{2} x_j B_{ji}} \Bigg] \\ &- \sum_{i=1}^{2} x_i \left(\frac{\sum_{j=1}^{2} x_j V_{m,j} B_{ji} \ln B_{ji}}{\sum_{j=1}^{2} x_j V_{m,j} B_{ji}}\right),\end{aligned} \tag{4.66}$$

where $x_1 = x(\mathrm{MCl_3})$ and $x_2 = 1 - x_1$. The index orientation is consistent with Equations (4.63) and (4.64) and the cited MIVM formulation.

Binary benchmark calibration. For the calibrated binary calculations, Z_1, Z_2, $V_{m,1}$ and $V_{m,2}$ were held fixed and only B_{12} and B_{21} were adjusted against calorimetry. For NaCl – $CeCl_3$, the fitting target was the Papatheodorou and Kleppa [26] calorimetric description at 1118 K. The verified analysis minimised the residuals in ΔH_{mix} while optimising $\ln B_{12}$ and $\ln B_{21}$, which enforces positive B-values, and repeated the nonlinear least-squares calculation from multiple initial guesses before retaining the lowest-residual solution. For NaCl – $NdCl_3$, the calibrated curve used the complete 16-point Gaune–Escard et al. [20] calorimetric dataset at 1124 K as the fitting target, while the same PIM–MD-derived coordination and molar-volume quantities were retained. The calibration therefore changes the effective energetic interaction parameters, not the structural or volumetric inputs.

The PMF-informed and calibrated variants answer different questions. Agreement of the former with direct PIM–MD or experiment tests a structure-to-energetics mapping without enthalpy fitting.

Agreement of the latter with the calibration data is expected and measures how large an effective correction is required to reconcile the simplified MIVM representation with calorimetry; it is not an independent validation. Fit residuals were consequently treated as calibration diagnostics rather than as molecular-dynamics uncertainty.

For the PMF-informed binary calculations, smooth curves were evaluated over $0 \leq x(\mathrm{MCl_3}) \leq 1$, with exact zero pure-component endpoints. The Nd workflow additionally used one-at-a-time $\pm 10\%$ perturbations of Z_1, Z_2, B_{12} and B_{21}; the Ce workflow applied the same perturbation set to assess the relative sensitivity of the fitted MIVM curve. These calculations are deterministic sensitivity tests, not confidence intervals.

Three-component extension. The ternary result reported in Section 5.4 was generated with the implemented three-component PMF-informed MIVM along the equal-Ce/Nd composition path. No ternary calorimetric values were used to fit that model, and no benchmark-calibrated ternary curve is reported. The ternary calculation therefore remains a model-based extension of the binary structure-to-energetics workflow. In particular, the Ce–Nd contribution is not constrained by an independent $CeCl_3$ – $NdCl_3$ calorimetric dataset, so its parameterisation is a model limitation rather than an experimentally validated interaction. The reported dashed end regions are model extrapolations and are not additional MD state points. Because the Ce–Nd contribution was not independently calibrated, no separately transferable closed-form Ce–Nd parameter rule is claimed beyond the implemented three-component model.

The calibrated MIVM route is potentially useful for data-sparse actinide salts: a limited set of calorimetric measurements can, in principle, constrain the most sensitive effective interaction parameters while atomistic simulation supplies structural and volumetric inputs, as demonstrated for another molten chloride system by Goncharov et al. [72]. Such use requires an independent transferability check. No UCl_3- or $PuCl_3$-containing MIVM calculation was performed in the present work because a compatible set of structural, volumetric and calorimetric inputs was not assembled for that purpose.

4.6.3 Composition-Space Representation of Excess Heat Capacity

Binary C_p^E values were represented by

$$C_p^E(x) = x(1-x)\sum_{k=0}^{m} A_k(2x-1)^k, \tag{4.67}$$

using the Redlich–Kister form [69]. Where the verified analysis supplied shared-reference bootstrap covariance, it was retained in a generalized-least-squares fit; fixed-order ordinary-least-squares descriptions were used where covariance weighting was not part of the original workflow. The curves are descriptive and do not replace the direct C_p^E values.

Because the ternary path does not terminate at a pure rare-earth component, it was interpolated only over the simulated interval using

$$C_p^E(z) = \sum_{k=0}^{m} B_k z^k, \qquad z = \frac{x_{\mathrm{NaCl}} - x_{\mathrm{c}}}{x_{\mathrm{s}}}, \tag{4.68}$$

where x_c and x_s are the centre and half-range of the sampled $x(\mathrm{NaCl})$ interval. The displayed rare-earth coordinate was equivalently

$$x(\mathrm{CeCl_3}) + x(\mathrm{NdCl_3}) = 1 - x(\mathrm{NaCl}). \tag{4.69}$$

This construction is an interpolation along the simulated equal-Ce/Nd pseudo-binary path and is not extrapolated to unsimulated ternary limits. Model-order or weighting sensitivity, where evaluated, is reported separately from the bootstrap sampling uncertainty of the underlying heat capacities.

4.7 Statistical Analysis, Uncertainty and Validation

The statistical treatment was matched to the estimator and to the verified post-processing workflow for each simulation family. Thus, all reported properties were calculated from defined production intervals, but identical window-selection and uncertainty estimators are not claimed where they were not used. The principal choices are summarised in Table 4.6; the supporting state-level evidence is linked in the final column.

Table 4.6. Property-specific retained data and primary statistical treatment.

Quantity	Retained data	Primary assessment	Supporting evidence
Density and V_m	Nd: state-specific stationary interval; Ce: after the first 1000 saved box records; ternary: after the first 10%	Workflow-specific mean and uncertainty estimator; correlation-aware blocking for Nd	Section A.2
V_m^E	Mixture and same-temperature pure-component V_m estimates	Shared-reference covariance for Nd; verified descriptive fitting choices for Ce and ternary	Section A.2
ΔH_{mix}	Ten blocks per retained NPT series	Shared-reference block bootstrap, 10 000 replicates	Section 4.7.2
C_p, C_p^E	Final 50% (Ce) or 60% (Nd and ternary)	Bootstrap refitting of the enthalpy–temperature slope and regression sensitivity checks	Section A.3
RDF and graph descriptors	Final 500 ps after a 200 ps NVT transient	Segment convergence and blockwise populations	Section 4.7.3
Thermal-conductivity inputs	Final 80% of each NPT trajectory	Block-count, discard-fraction and RDF-smoothing sensitivity	Section A.4
Viscosity	Exact 5 ns stress series	System-specific trajectory-length, shifted-window and spectral-sensitivity tests; complete-trajectory SporTran uncertainty	Section A.5

4.7.1 Equilibration, Blocking and Mean Properties

Molecular-dynamics observations are serially correlated and may include an initial transient. Production intervals were therefore defined before the reported averages were formed, and correlation-aware diagnostics were used where they were part of the verified workflow [58, 74]. For

$NaCl-NdCl_3$ density and molar volume, the retained start was selected separately for each state using statistical inefficiency, effective sample size, residual-trend, alternative-cutoff and split-half checks. The Ce and ternary workflows instead used fixed family-wide late-time intervals. Applying one rule consistently within each family avoided composition-specific selection of favourable trajectory regions. The exact distinctions and checks are reported in Section A.2.

For analyses based on contiguous block estimates Y_b,

$$\overline{Y} = \frac{1}{B}\sum_{b=1}^{B} Y_b, \tag{4.70}$$

$$s_{\overline{Y}} = \left[\frac{1}{B(B-1)}\sum_{b=1}^{B}(Y_b - \overline{Y})^2\right]^{1/2}. \tag{4.71}$$

Where a Student-t interval was part of the analysis, the two-sided 95% interval was

$$\overline{Y} \pm t_{0.975,B-1}s_{\overline{Y}}. \tag{4.72}$$

Mean properties were averaged within each block, whereas fluctuation-derived quantities such as κ_T were recalculated from each block. For the correlation-aware Nd volume analysis, the state-point standard error s_j used in inverse-variance weighting was conservatively defined as the larger of the autocorrelation-corrected standard error and the standard error of the contiguous block means.

4.7.2 Derived and Regression-Based Properties

For V_m^E, the uncertainty treatment followed the verified system-specific workflow described in Section 4.5.3. The Nd analysis propagated the shared endpoint covariance into covariance-aware Redlich–Kister fits. The Ce and ternary analyses retained their predefined fixed-order, unweighted descriptions. This distinction is stated explicitly so that regression sophistication is not confused with the statistical quality of the underlying PIM-MD averages.

For direct mixing enthalpy, each retained enthalpy series was divided into ten approximately equal blocks. Mixture and independent pure-component block means were resampled independently for $10\,000$ non-parametric replicates [75]. When one pure-component trajectory was genuinely shared by several compositions, the same draw was reused in those calculations. For replicate b,

$$\Delta H_{\mathrm{mix}}^{(b)} = \overline{H}_m^{(b)} - \sum_i x_i \overline{H}_{m,i}^{0,(b)}. \tag{4.73}$$

The 2.5th and 97.5th percentiles defined the 95% interval, and pure endpoints remained exactly zero.

Heat-capacity uncertainty was obtained by resampling retained enthalpy blocks within each temperature. For each replicate, one mean enthalpy was reconstructed at each of the four temperatures, Equation (4.27) was refitted, and the slope was stored as a C_p realisation. Production-average temperatures were used where a temperature time series was available; for the ternary archive they were reconstructed consistently from the saved kinetic energy. Ordinary least squares provided the primary slope. Inverse-variance weighted fits, nominal thermostat temperatures, a quadratic

enthalpy–temperature relation and leave-one-temperature-out linear fits were used as sensitivity diagnostics rather than as alternative reported values. The window-specific evidence is given in Section A.3.

Binary C_p^E replicates reused the corresponding pure-component slope draws across all interior compositions, thereby preserving the dependence created by common references. The ternary calculation likewise reused common pure-component draws across its pseudo-binary path. The 2.5th and 97.5th percentiles of the resulting distributions defined the reported intervals. Polynomial order, weighting and fitted-extremum sensitivity are reported as model diagnostics; they are not interpreted as direct uncertainty in the underlying molecular-dynamics samples.

4.7.3 Structural and Model-Based Quantities

RDF convergence was assessed by comparing successive, non-overlapping trajectory segments. Peak positions, first-minimum locations and integrated coordination numbers were examined rather than relying solely on visual curve overlap. Pointwise uncertainty bands were not interpreted as necessary at every radial bin because neighbouring bins are strongly correlated.

Mean coordination numbers, integer coordination-state fractions, cluster-size fractions and linkage fractions were recalculated for contiguous trajectory blocks. Framewise fractions were first formed within each block and then summarised across blocks, avoiding a population estimate dominated by blocks containing more saved frames. The first-shell cutoff derived from the full retained RDF was used consistently for framewise population analysis, and a small cutoff perturbation was reserved as a sensitivity check for graph-derived quantities.

Temporal-persistence statistics followed the same distinction between within-trajectory variability and independent replication. Sequential windows or blocks were used to test stability of the continuous and intermittent persistence metrics, but their standard errors were not interpreted as between-replica confidence intervals. A persistence trend was considered structurally informative only when the required $1/e$ crossing occurred within the analysed lag interval and the composition dependence remained coherent across the repeated windows. Finite-lag integrals that had not reached a stable plateau were labelled partial rather than converted into apparent infinite-time lifetimes.

For the PMF-informed MIVM, no formal confidence interval was assigned because RDF, coordination-number and PMF-minimum uncertainties were not jointly propagated. The $\pm 10\%$ one-at-a-time calculations and the alternative unlike-pair constructions were treated as deterministic sensitivity tests. For the benchmark-calibrated binary MIVM, residuals measure calibration quality and were not reinterpreted as uncertainty in the underlying PIM–MD data or as out-of-sample predictive uncertainty. Likewise, uncertainty from the Ce – Nd contribution was not propagated into the ternary MIVM and remains a model limitation.

For thermal conductivity, κ_T variability was estimated from five contiguous blocks, while the $C_{p,m}$ and α_V fits were assessed with R^2, RMSE and alternative fit forms [58, 76, 77]. No formal state-point confidence interval was assigned to ℓ_{sc} or λ, because coherence-length sampling and joint propagation of all model inputs were unavailable. Conductivities were therefore reported as model estimates without formal error bars.

4.7.4 Viscosity Convergence and Uncertainty

Viscosity convergence was assessed with system-specific trajectory-length, shifted-window and spectral-sensitivity tests rather than one universal window sequence. For NaCl – $NdCl_3$, the validated 5 ns analysis compared cumulative 3, 4 and 5 ns estimates at neighbouring spectral settings and applied additional shifted-window tests to flagged states. The NaCl – $CeCl_3$ and ternary datasets were assessed with their corresponding documented trajectory-window and spectral-sensitivity protocols. In all cases, the complete-trajectory SporTran estimate was retained as the primary viscosity estimate, while direct Green–Kubo calculations and window-dependent estimates were used as convergence diagnostics. Multiple stress components and multiple windows from one trajectory were not interpreted as independent simulation replicates.

A result was accepted when the intended stress series was complete; temperature, energy and stress were stationary; component ACFs were mutually consistent; the averaged ACF decayed to zero-centred noise; cumulative estimates approached a stable value; direct Green–Kubo and cepstral estimates agreed within their stable regions; and the cepstral result was insensitive to the retained frequency range and coefficient count. The complete-trajectory SporTran uncertainty was reported as the primary uncertainty. Results failing these criteria were explicitly qualified rather than assigned artificial precision [58, 78].

4.7.5 Reference-Data Matching and Validation Hierarchy

Validation followed a hierarchy of evidence. Same-system experimental data were primary; prior same-system simulations were secondary; comparisons with uranium- or plutonium-bearing salts were analogue or simulant assessments and were not called direct validation. Reference datasets were screened for salt identity, composition convention, temperature scale, units, phase state, reported validity interval and whether a value was measured directly or generated from a fitted correlation. Where a secondary compilation was used, the original experimental attribution was retained whenever it could be identified. Direct temperature–composition matches were used wherever possible. Interpolation was restricted to the simulated domain, extrapolation was identified explicitly, and reference values outside their stated validity range received less evidential weight. Experimental uncertainty bars were shown only when the source provided an interpretable statistical quantity. Scatter, fit residuals, instrument uncertainty and between-study disagreement were not treated as interchangeable. Consequently, the absence of an experimental error bar in a figure did not imply that the reference value was exact; it indicated that a consistent uncertainty could not be reconstructed from the source.

For density and molar volume, comparisons were performed at the experimental composition or temperature using the property-specific interpolation procedures in Sections 4.5.1 and 4.5.2. For C_p, the experimental definition and temperature dependence were checked against the interval-average slope used here. For mixing enthalpy, reference states and the definition per mole of salt formula units were matched before comparison. Structural comparisons prioritised distances and coordination trends that can be related to diffraction or atomistic simulations, whereas graph-derived cluster labels were compared only qualitatively. Transport comparisons required both numerical agreement and evidence that the simulated correlation functions were converged.

Table 4.7. Validation and benchmarking hierarchy used for the reported property groups.

Property group	Primary evidence	Interpretation
ρ, V_m, V_m^E	Same-system experiment at matched T and composition	Numerical deviations and trend agreement; absolute differences near zero excess values
C_p, C_p^E	Same-system values with compatible definitions and temperature ranges	Interval-average character and regression uncertainty retained
ΔH_{mix}	Same-system thermochemical data where available	Magnitude, minimum composition and temperature dependence
RDF, CN and topology	Diffraction and previous atomistic simulations	Peak positions, shell boundaries, coordination and qualitative connectivity trends
Viscosity	Available same-system literature and previous MD, supplemented by internal convergence diagnostics	Matched comparisons where available plus trajectory and spectral convergence evidence
Thermal conductivity	Input plausibility, source-model context and available salt data	Model-route assessment, not direct Green–Kubo validation
Ternary/simulant behaviour	Internal consistency and matched actinide analogues	Property-specific analogue assessment, not universal validation

Deviation Measures

For N_{cmp} matched points and non-zero reference values,

$$\delta_{Y,j} = 100\frac{Y_{\mathrm{MD},j} - Y_{\mathrm{ref},j}}{Y_{\mathrm{ref},j}}, \tag{4.74}$$

$$\overline{\delta}_Y = \frac{1}{N_{\mathrm{cmp}}}\sum_{j=1}^{N_{\mathrm{cmp}}} \delta_{Y,j}, \tag{4.75}$$

$$\mathrm{MAPD}_Y = \frac{1}{N_{\mathrm{cmp}}}\sum_{j=1}^{N_{\mathrm{cmp}}} |\delta_{Y,j}|. \tag{4.76}$$

Positive and negative values denote overprediction and underprediction. Percentage measures were not used for zero or near-zero excess properties; absolute differences and uncertainty overlap were used instead.

Thermophysical validation considered density, V_m, V_m^E, C_p and C_p^E separately because agreement in one quantity does not establish the others. Energetic assessment considered the magnitude, composition and temperature dependence of ΔH_{mix}. Agreement between direct PIM–MD and the PMF-informed MIVM was treated as internal structure-to-energetics consistency, whereas agreement of the benchmark-calibrated MIVM with its fitted calorimetry was treated as calibration performance rather than independent validation. Structural assessment used RDF distances, coordination and topology trends against diffraction and prior simulations. Viscosity used available matched literature comparisons where possible together with internal convergence evidence. Thermal-conductivity assessment considered both input plausibility and final literature-scale agreement while retaining the structural-coherence model limitation.

4.7.6 Ternary and Simulant Assessment

The ternary system was assessed only along the equal-Ce/Nd pseudo-binary path. In the absence of complete ternary experimental coverage, checks included smooth composition dependence, consistency with the binary and pure-component trends, physical admissibility, and explicit consideration of the additional Ce – Nd cross-interaction assumption. Extrapolation from this line to the remainder of the ternary triangle was not performed. A smooth curve was not, by itself, treated as evidence that the cross interaction was quantitatively correct. Such checks establish internal consistency rather than experimental validation of the full ternary triangle.

Rare-earth chlorides were evaluated as property-specific simulants for actinide-bearing salts. Density, volume, energetic, structural and transport behaviour were compared independently at matched temperature and composition where possible. Comparisons based on different oxidation states, unmatched salt fractions or extrapolated temperatures were identified as qualitative context rather than included silently in numerical deviation metrics. Similarity in one property was not taken to imply universal simulant validity; differences in ionic size, polarizability, oxidation-state chemistry and local structure were retained in the interpretation.

5

Results and Discussion

5.1 Liquid Structure and Network Formation

The liquid structures of the binary NaCl – $CeCl_3$ and NaCl – $NdCl_3$ melts and the equal-Ce/Nd NaCl – $CeCl_3$ – $NdCl_3$ composition path were analysed using partial pairwise radial distribution functions (RDFs), coordination statistics, graph-based cluster speciation and shared-chloride linkage populations. Here, "ternary" refers to the three salt components NaCl, $CeCl_3$ and $NdCl_3$; at the ionic-species level the melt contains four species, Na^+, Ce^{3+}, Nd^{3+} and Cl^-.

The structural results were additionally compared with the polarizable-ion molecular-dynamics results of Ter Veer et al. [79] for NaCl – UCl_3, NaCl – $PuCl_3$ and NaCl – UCl_3 – $PuCl_3$. These comparisons test whether experimentally accessible, non-radioactive lanthanide systems reproduce actinide-melt behaviour at several structural levels: local coordination, coordination-number distributions, shared-chloride topology and composition-driven network formation. They are therefore used as a property-specific simulant assessment rather than as a claim of complete chemical equivalence.

These descriptors are physically interconnected. Cation size, polarising strength and local charge density determine the preferred metal–chloride coordination environment. Electrostatic attraction, chloride–chloride repulsion and geometrical packing then constrain how many chlorides can occupy the first shell. At larger length scales, the number density of trivalent centres controls the probability that neighbouring coordination shells share chloride ions. The resulting liquid structure therefore reflects an interaction between local coordination chemistry and the statistical physics of network formation.

5.1.1 Local Order and Coordination

The radial distribution functions at 1100 K are compared in Figure 5.1. Both binary melts exhibit a pronounced first metal–chloride maximum, confirming persistent short-range coordination around the trivalent cations. For example, at $x(CeCl_3) = 0.50$, the first Ce – Cl, Cl – Cl and Ce – Ce maxima

occur at approximately 2.76, 3.50 and 4.66 Å, respectively. Their distinct positions show that the RDFs resolve separate first-shell, anion–anion and intermediate-range cation correlations.

The first Ce – Cl maximum occurs at a slightly greater distance than the corresponding Nd – Cl maximum. This ordering is consistent with the lanthanide contraction: the effective ionic radius decreases from Ce^{3+} to Nd^{3+} [37]. Independent XAFS measurements of the pure molten trichlorides likewise place the mean Ce – Cl distance near 2.81 Å and the Nd – Cl distance near 2.73 Å [14]. The larger Ce-centred coordination shell can therefore accommodate chlorides over a broader radial region, whereas the smaller Nd-centred shell is more compact. Although both cations carry the same formal charge, their local coordination geometries remain chemically distinct.

Increasing the lanthanide chloride fraction broadens the first metal–chloride maximum while producing comparatively small changes in its position. The accompanying decrease in peak height does not imply a reduction in coordination. In the NaCl-rich region, the trivalent cations are dilute and occupy relatively isolated, narrowly distributed chloride environments. At higher $x(MCl_3)$, chlorides increasingly participate in the first shells of more than one lanthanide ion. The corresponding distribution of instantaneous metal–chloride distances broadens, reducing the peak maximum even as the integrated coordination number increases.

The metal–metal correlations respond more strongly to composition. At low lanthanide content, trivalent cations are separated by the NaCl-rich matrix and their mutual correlations remain weak. Increasing the lanthanide number density raises the probability of forming M – Cl – M bridges and produces a more pronounced metal–metal correlation. The simultaneous evolution of the Cl – Cl RDF reflects the changing role of chloride from predominantly completing isolated coordination shells to increasingly connecting neighbouring metal-centred environments.

The ternary RDFs retain separate Ce – Cl and Nd – Cl correlations while also developing a clear Ce – Nd correlation. The two lanthanides therefore do not become locally indistinguishable, but neither do they form two independent binary liquids. Chemically distinct Ce- and Nd-centred first shells are incorporated into a common mixed chloride-connected structure. This structural coexistence does not by itself establish thermodynamic ideality: the excess-volume, excess-heat-capacity and mixing-enthalpy results discussed later remain non-zero. Whether the Ce/Nd linkages themselves show preferential rather than statistical mixing is tested explicitly from the species-resolved linkage populations below.

Temperature produces a weaker change than composition. Heating broadens the RDF peaks and lowers their maxima by increasing the range of instantaneous ion separations and accelerating chloride exchange. Composition, in contrast, changes the number of available lanthanide neighbours and therefore changes the connectivity that the liquid can form. Temperature primarily disorders the network, whereas composition changes its underlying topology. Supporting RDFs at the low- and high-temperature limits, 900 and 1200 K, are provided in Figures A.2 and A.3; they preserve the same qualitative ordering of Ce- and Nd-centred first-shell distances while showing the expected thermal broadening.

Published atomistic studies provide an independent context for the supplied actinide benchmark. PIM–MD studies of NaCl – UCl_3 report composition-dependent uranium coordination and the development of a chloride-connected uranium network [80, 81], while recent actinide force-field studies resolve analogous local coordination in pure UCl_3 and $PuCl_3$ [82, 83].

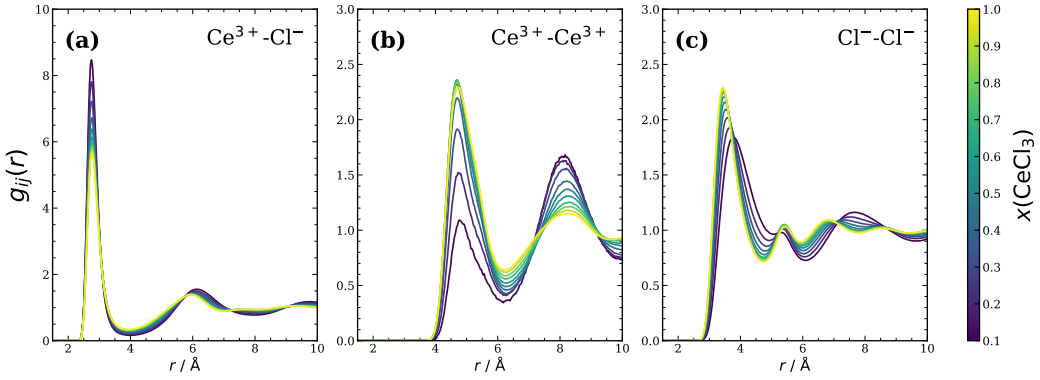

(a) $NaCl - CeCl_3$.

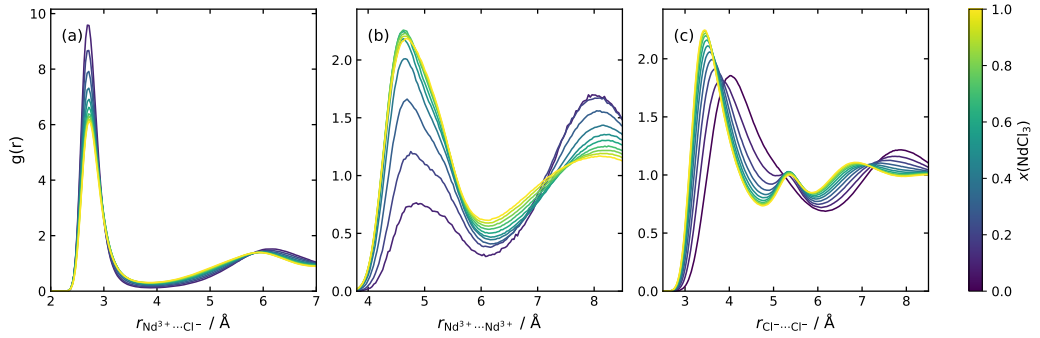

(b) $NaCl - NdCl_3$.

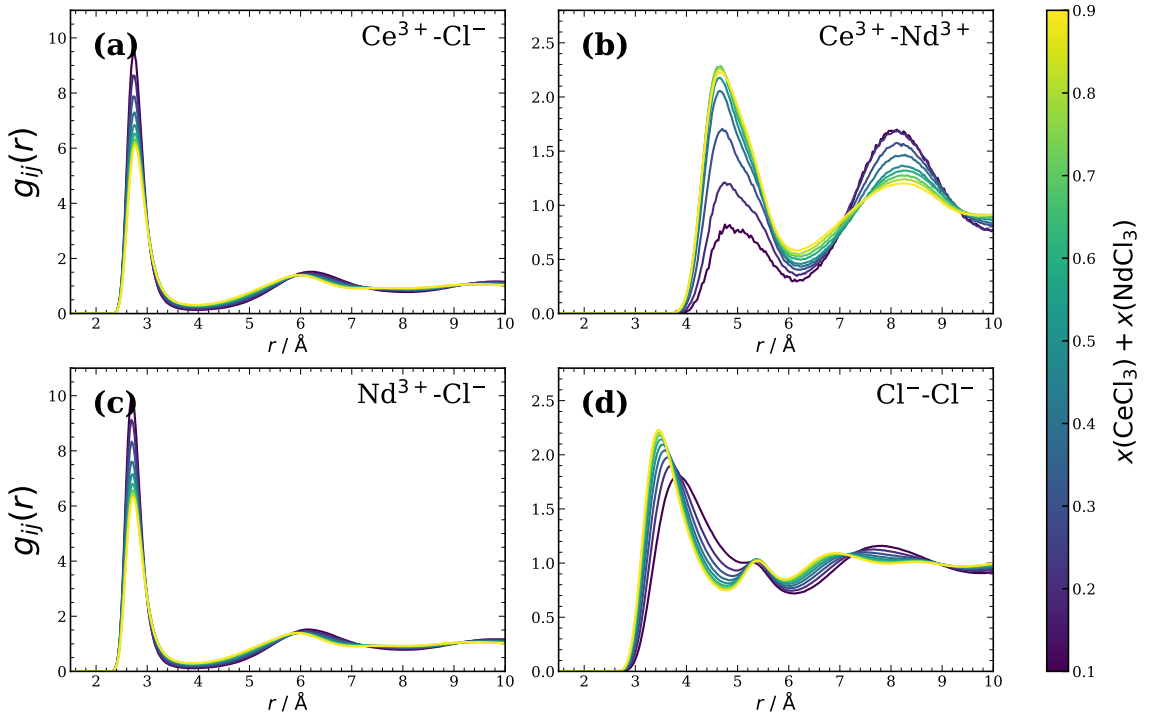

(c) $NaCl - CeCl_3 - NdCl_3$.

Figure 5.1. Composition-dependent radial distribution functions at 1100 K for the two binary melts and the equal-Ce/Nd ternary path. For the ternary system, $x(\mathrm{LnCl_3}) = x(\mathrm{CeCl_3}) + x(\mathrm{NdCl_3})$.

The independently published coordination-number distributions give a useful numerical cross-check. Using the digitised pure-salt distributions compiled for this study and normalising the resulting populations gives mean U–Cl coordination numbers of approximately 7.54 from Pireddu et al. [82] and 7.38 from Notarangelo et al. [83]. The corresponding Pu–Cl means are approximately 6.97 and 7.49, respectively. In the U distributions, CN 7–8 states dominate: Pireddu et al. give approximately 38.6% and 40.0%, while Notarangelo et al. give approximately 41.9% and 36.5%. For Pu, Notarangelo et al. likewise give approximately 38.9% CN 7 and 39.2% CN 8, whereas the Pireddu distribution is shifted towards lower coordination, with approximately 27.2% CN 6, 47.3% CN 7 and 21.8% CN 8. These independent datasets therefore confirm that the first shell is an exchanging distribution rather than one unique integer coordination state, while also showing that the absolute mean depends on the force field and simulated state point.

The published linkage analyses support the same intermediate-range picture but are not numerically interchangeable with the present classification. In particular, van Oudenaren et al. [81] report that above approximately 40 mol% UCl_3, $NaCl-UCl_3$ develops a three-dimensional network of corner- or edge-sharing uranium polyhedra, and Pireddu et al. [82] analyse anionic bridging modes across the pure actinide chlorides. Because those studies use different state points and directly comparable corner/edge/face percentages could not be established with the same counting definition used here, literature-derived percentages are not merged into the matched 1100 K comparison below. The numerical U/Pu values used in that direct comparison therefore remain the internally consistent dataset supplied by Ter Veer et al. [79].

The average first-shell coordination numbers provide a direct structural comparison with the corresponding actinide melts. As shown in Figure 5.2, the mean $Ce-Cl$ coordination number at 1100 K increases from approximately 6.8 in the NaCl-rich region to a broad plateau near 7.6. The $U-Cl$ coordination numbers reported by Ter Veer et al. [79] exhibit the same composition dependence, increasing from approximately 6.6 near $x(UCl_3) = 0.10$ to approximately 7.4 in the U-rich region.

The systematic offset between the Ce and U curves is generally of the order of 0.2–0.3 chloride neighbours. Consequently, $NaCl-CeCl_3$ reproduces the composition-driven increase and high-composition plateau of $NaCl-UCl_3$, but slightly overestimates the absolute first-shell population. This indicates trend-level structural similarity rather than exact numerical equivalence.

The $NaCl-NdCl_3$ and $NaCl-PuCl_3$ comparison is considerably closer. Their coordination-number curves nearly overlap across the complete composition range. Both increase from approximately 6.3–6.4 in the NaCl-rich region to about 7.2 in the trichloride-rich region, with differences generally below approximately 0.1. At the level of average local coordination, Nd therefore provides a particularly close structural representation of Pu in the supplied Ter Veer et al. [79] dataset.

The increase in coordination number with trichloride content reflects the redistribution of chloride between monovalent and trivalent coordination environments. In the NaCl-rich region, the trivalent centres are widely separated and many chloride ions remain associated primarily with the sodium-chloride matrix. Increasing the trichloride fraction strengthens the population of metal-centred chloride environments and increases the probability that a chloride lies within the first shells of two neighbouring trivalent cations. Chloride sharing can therefore increase the coordination population of both metals while simultaneously generating network connectivity.

The difference between Ce and Nd demonstrates that coordination cannot be interpreted from electrostatic attraction alone. The smaller Nd^{3+} ion generates a more compact local field, but the reduced first-shell volume and increased chloride–chloride crowding restrict the number of anions that can be accommodated. The larger Ce-centred shell supports a somewhat higher mean coordination number. Local coordination is therefore controlled jointly by cation–anion attraction, available shell volume, chloride polarisation and anion–anion packing.

At high trichloride content, the average coordination numbers approach plateaux because the first shells have reached their preferred population ranges. Further increases in composition then alter how the coordination shells connect more strongly than they alter the number of chlorides surrounding each individual cation. This separation between local-shell saturation and continuing network development is important for interpreting the cluster and linkage results below.

The ternary heatmaps in Figure 5.2 show that changes in the mean coordination number do not correspond to rigid transitions between integer coordination states. Several coordination populations coexist at every composition, with increasing $x(\mathrm{LnCl_3})$ transferring probability from lower-CN toward higher-CN environments. Ce remains shifted towards the more highly coordinated states relative to Nd, even though both ions participate in the same mixed network.

The pure-actinide distributions supplied by Ter Veer et al. [79] are also dominated by CN 7 and CN 8. For UCl_3, these populations account for approximately 43.70% and 35.97%, respectively, while the corresponding values for $PuCl_3$ are approximately 47.07% and 30.55%. The same dominance of seven- and eight-fold environments appears in the concentrated lanthanide melts. The complete binary coordination distributions are provided in Figure A.1.

5.1.2 Cluster Formation and Network Polymerisation

The graph-based speciation results reveal a rapid transition from isolated coordination environments to an extended shared-chloride network. At a lanthanide chloride fraction of 0.1, monomers remain the largest population in both binary systems. The dilute $NaCl-NdCl_3$ melt is more strongly monomeric than $NaCl-CeCl_3$, consistent with its more compact first shell and lower probability of multiply connected configurations.

Increasing the trichloride content strongly suppresses the finite monomer, dimer and trimer populations. At $x(\mathrm{MCl_3}) \approx 0.2$, the polymer fraction becomes a major contribution, and by approximately $x(\mathrm{MCl_3}) = 0.3$, more than 90% of the lanthanide ions belong to connected components containing four or more trivalent centres. The complete binary speciation curves are provided in Figure A.4.

This crossover is substantially sharper than the change in average coordination number. A lanthanide ion can possess a well-populated first coordination shell while remaining monomeric when no second trivalent centre is sufficiently close to share one of its chloride ions. Increasing the trivalent-cation number density reduces the separation between possible neighbours and increases the number of available bridging configurations. Once several shared-chloride links coexist, finite clusters merge rapidly into an extended network.

The same composition-driven crossover is observed in the ternary lanthanide melt and in the $NaCl-UCl_3-PuCl_3$ results supplied by Ter Veer et al. [79] At a total trivalent-chloride fraction of 0.10, the lanthanide ternary contains approximately $55–67\%$ monomeric ions and approximately

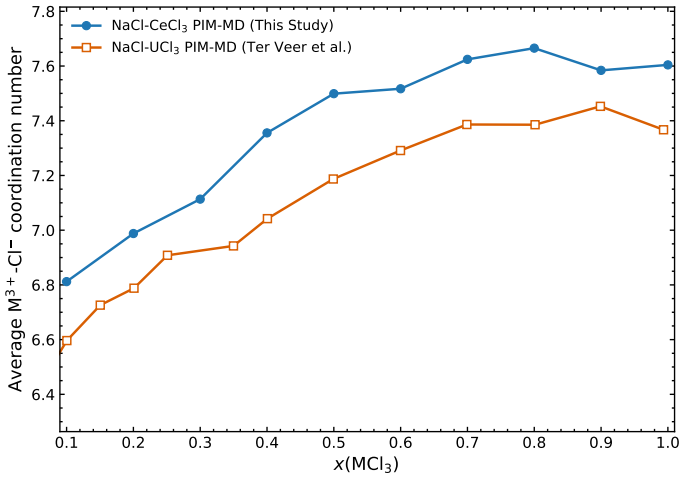

(a) NaCl – $CeCl_3$ compared with NaCl – UCl_3 from Ter Veer et al. [79]

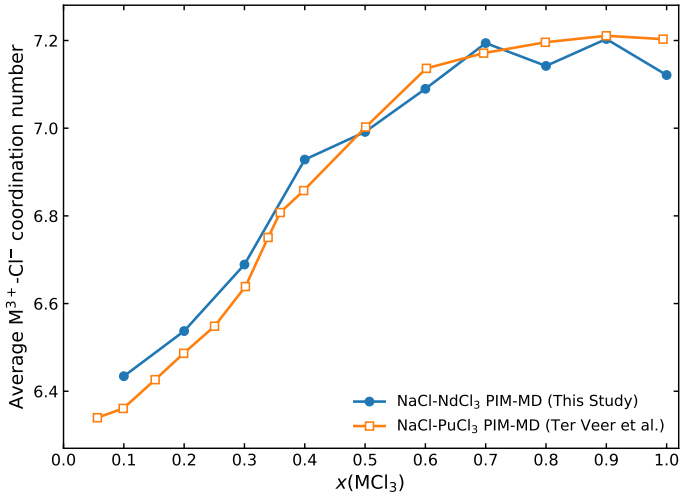

(b) NaCl – $NdCl_3$ compared with NaCl – $PuCl_3$ from Ter Veer et al. [79]

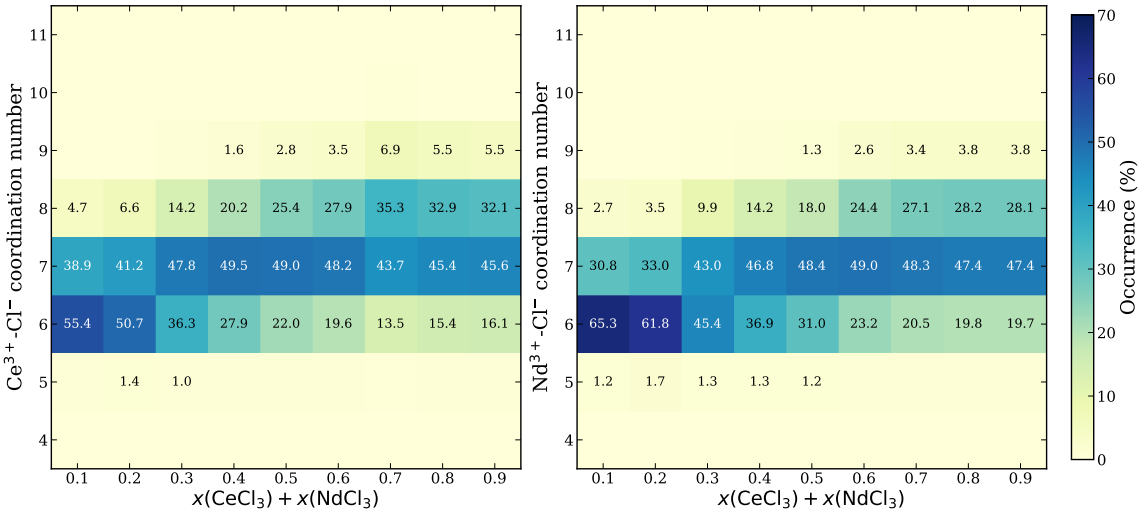

(c) Separate Ce- and Nd-centred coordination-number distributions in the equal-Ce/Nd ternary path.

Figure 5.2. Local coordination in the simulated lanthanide melts and comparison with the actinide PIM-MD results supplied by Ter Veer et al. [79] The binary panels show average first-shell coordination numbers at 1100 K. The ternary heatmaps show the percentage occurrence of individual coordination-number states.

4–10% polymeric ions, depending on temperature. Ter Veer et al. [79] report 59.53% monomers and 7.35% polymers at the corresponding composition.

At a trivalent-chloride fraction of 0.20, the lanthanide polymer fraction rises to approximately 40–50%, compared with 53.75% in the actinide system. By a fraction of 0.30, both systems contain approximately 90% or more polymeric trivalent cations: the Ter Veer et al. [79] value is 92.62%. At 0.40, the polymer fractions approach complete network formation, with Ter Veer et al. [79] reporting 99.37%.

The close correspondence in the location and sharpness of this connectivity crossover is significant. It shows that the mixed lanthanide and mixed actinide melts respond similarly to increasing trivalent-cation density, despite differences in their individual chemical identities. In both systems, a predominantly monomeric liquid at low trichloride content evolves into an almost completely polymerised chloride-connected network over the relatively narrow composition interval between approximately 0.1 and 0.4.

The present ternary analysis further shows that the lanthanide network becomes predominantly mixed Ce–Nd above $x(\mathrm{LnCl_3}) \approx 0.3$. The supplied Ter Veer et al. [79] dataset resolves actinide cluster sizes but does not separately identify U-only, Pu-only and mixed U–Pu cluster populations. The comparison therefore supports similarity in the extent and onset of polymerisation, but no conclusion regarding the detailed U–Pu cluster composition is drawn from these data.

5.1.3 Shared-Chloride Network Topology

The linkage populations resolve how the polymerised networks are assembled. Corner-sharing corresponds to one shared chloride, edge-sharing to two shared chlorides, and face/higher-order sharing to three or more shared chlorides. Corner-sharing remains the largest individual contribution in all of the lanthanide melts, while edge-sharing forms a substantial secondary population and face/higher-order configurations remain less abundant.

Corner-sharing is favoured because it connects neighbouring coordination shells while maintaining a comparatively large metal–metal separation and allowing greater orientational freedom. Edge- and face-sharing satisfy a greater fraction of the coordination requirements of two cations using the same chloride ions, but they also bring the positively charged cations closer together, increase chloride crowding and restrict the relative orientation of their coordination environments. Their populations therefore reflect a competition between the chemical benefit of shared coordination and the physical penalties of cation–cation repulsion and geometrical confinement.

Increasing the lanthanide fraction decreases the corner-sharing fraction and increases the edge- and face/higher-order populations. The network therefore develops not only by creating a larger number of connections, but also by increasing the multiplicity of the connections between neighbouring metal centres. At high composition, the linkage fractions begin to level off, consistent with saturation of the local coordination shells and near-complete cluster polymerisation.

The pure-endmember linkage populations are compared with the Ter Veer et al. [79] actinide results in Table 5.1. The $CeCl_3$ – UCl_3 pair exhibits an especially close edge-sharing fraction: 40.64% for Ce and 40.41% for U. Ce is slightly less corner-sharing and more face/higher-order sharing than U, but the overall balance among the three linkage classes remains similar.

Table 5.1. Near-pure first-shell coordination numbers and shared-chloride linkage populations at 1100 K for the lanthanide melts and the actinide results supplied by Ter Veer et al. [79]. The actinide coordination numbers are digitised near-pure values. The lanthanide face/higher-order category includes the negligible $C_{\geq 4}$ contribution, which remains below 0.1%.

System	Average CN	Corner (%)	Edge (%)	Face/$C_{\geq 3}$ (%)
$CeCl_3$, this study	7.60	47.33	40.64	12.03
UCl_3, Ter Veer et al.	7.37	50.12	40.41	9.47
$NdCl_3$, this study	≈ 7.12	53.21	38.78	8.01
$PuCl_3$, Ter Veer et al.	7.20	48.87	40.77	10.36

The $NdCl_3$ – $PuCl_3$ pair also exhibits the same topology ordering, but the differences are somewhat larger. Nd is more corner-rich and less multiply connected than Pu, with approximately 53.21% corner-sharing compared with 48.87% for Pu. Thus, NaCl – $NdCl_3$ reproduces the NaCl – $PuCl_3$ average coordination numbers exceptionally closely, whereas its endmember network remains slightly more open and corner-dominated.

This distinction demonstrates why a simulant assessment based only on average CN would be incomplete. Two melts can have almost identical first-shell populations while differing in how those shells are connected. Conversely, Ce and U show a noticeable offset in average CN while maintaining closely comparable endmember linkage topologies. Structural representativeness is therefore scale dependent.

The ternary cluster and linkage results are shown separately in Figures 5.3 and 5.4 to preserve readability. The ternary linkage fractions lie between the characteristic binary behaviours. Corner-sharing decreases from approximately 63–64% at $x(\mathrm{LnCl_3}) = 0.1$ to approximately 47–51% at intermediate and high lanthanide fractions. Over the same interval, edge-sharing rises from approximately 32–33% to approximately 40–44%, while face/higher-order sharing increases from approximately 4–5% to approximately 10–12%.

The species-resolved linkage counts also allow random versus preferential Ce/Nd association to be tested directly. Along the equal-Ce/Nd path, random pairing of equally abundant Ce and Nd cations gives the large-population expectation 25:50:25 for Ce–Ce, Ce–Nd and Nd–Nd links. At 1100 K, representative states spanning $x(\mathrm{LnCl_3}) = 0.10$, 0.50 and 0.90 give, respectively, 24.95:50.94:24.11, 26.40:49.44:24.16 and 25.64:49.82:24.54. The maximum departure from the random-pair expectation is therefore only 1.40 percentage points across these representative states. Within the resolution of the present time-averaged analysis, the Ce/Nd linkage statistics are consequently consistent with approximately stochastic mixing rather than a strong preference for either hetero-cation or homo-cation association. Because no independent-replica uncertainty was assigned to these pair fractions, this is a descriptive test rather than a formal hypothesis test.

Because the ternary clusters become overwhelmingly mixed Ce–Nd, these intermediate fractions do not represent a macroscopic average of two separate binary networks. They arise from a single heterogeneous network containing Ce–Ce, Ce–Nd and Nd–Nd connections. The species-specific first shells therefore remain locally distinct while the intermediate-range topology becomes chemically mixed. The dominance of mixed clusters at high lanthanide fraction should not itself be interpreted

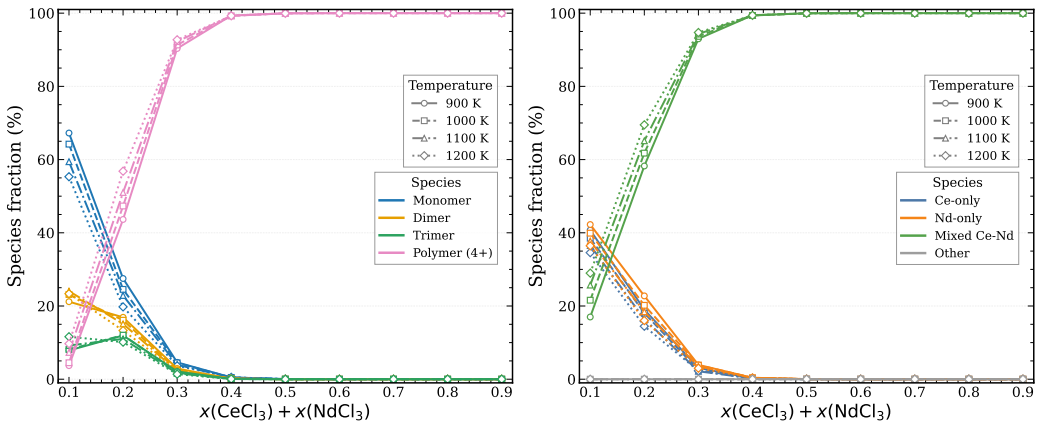

Figure 5.3. Composition-dependent cluster-size and cluster-composition speciation along the equal-Ce/Nd NaCl – $CeCl_3$ – $NdCl_3$ path at 900–1200 K. Polymers are connected components containing four or more lanthanide ions; cluster compositions are classified as Ce-only, Nd-only or mixed Ce–Nd.

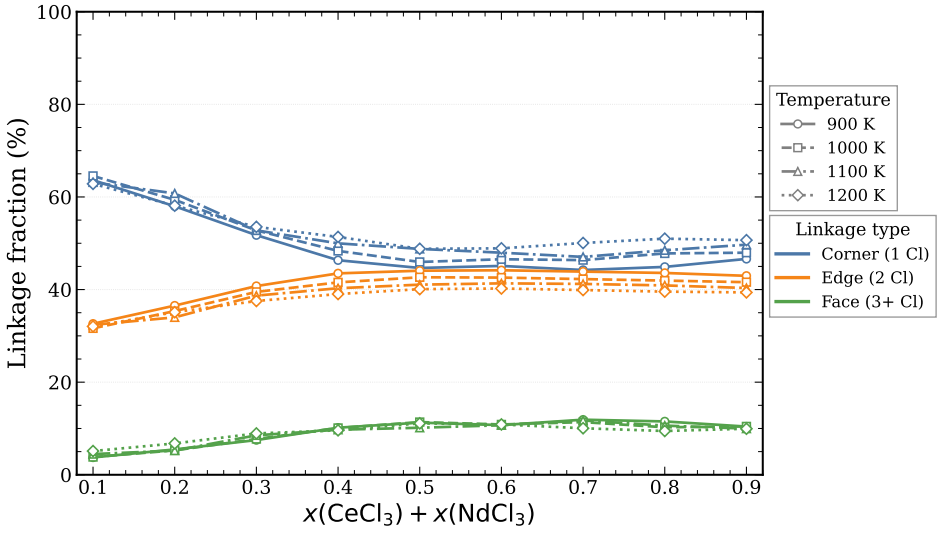

Figure 5.4. Composition-dependent shared-chloride linkage topology along the equal-Ce/Nd NaCl – $CeCl_3$ – $NdCl_3$ path at 900–1200 K. Corner-, edge- and face/higher-order categories correspond to one, two and three-or-more shared chloride neighbours, respectively.

as preferential Ce–Nd attraction: once large connected components form, a mixed cluster is expected even for statistically mixed Ce/Nd linkages.

5.1.4 Integrated Lanthanide–Actinide Interpretation

The simulated melts exhibit a common hierarchical response to increasing trivalent-chloride content. First, the local metal–chloride coordination population increases. Second, chloride sharing becomes more frequent and isolated first shells combine into finite clusters. Finally, the clusters merge into a nearly completely polymerised network containing substantial corner- and edge-sharing populations. These stages are coupled but not identical: the local CN approaches a plateau before the network topology stops evolving.

The comparison with Ter Veer et al. [79] demonstrates that the suitability of a lanthanide simulant depends on the structural scale considered. NaCl – $NdCl_3$ reproduces the average coordination-

number evolution of NaCl – $PuCl_3$ particularly closely, but the Nd-rich network is slightly more corner-dominated than the Pu-rich network. NaCl – $CeCl_3$ produces somewhat higher coordination numbers than NaCl – UCl_3, while reproducing a closely comparable balance between corner-, edge- and face-sharing configurations.

The strongest mixed-system correspondence is observed in the composition-driven polymerisation transition. Both NaCl – $CeCl_3$ – $NdCl_3$ and the NaCl – UCl_3 – $PuCl_3$ data supplied by Ter Veer et al. [79] evolve from predominantly finite species at low total trichloride content to more than 90% polymeric trivalent cations near a total fraction of 0.3 and almost complete polymerisation by approximately 0.4.

The results therefore support the use of the lanthanide systems as structural simulants at the level of composition-dependent local coordination and shared-chloride network formation. They do not imply exact structural identity. Ce provides a close representation of the U linkage topology but exhibits a higher local CN, whereas Nd closely represents the Pu coordination-number trend but forms a somewhat more open endmember network.

This multiscale structure also provides the microscopic basis for connecting chemistry with macroscopic transport. Cation size, polarisation and chloride affinity define the local coordination building blocks. Electrostatic repulsion, anion packing, configurational entropy and thermal motion determine how those building blocks connect and rearrange. Increasing network connectivity couples the motion of chloride ions to neighbouring trivalent centres and increases the collective structural rearrangement required for long-range ionic motion. The structural results therefore provide the physical and chemical framework for interpreting the composition dependence of transport properties discussed later in this chapter.

5.2 Volumetric Properties and Non-Ideal Mixing

The density, molar volume and excess molar volume were evaluated over the complete simulated composition range at 900–1200 K. The binary results are first compared with the available experimental descriptions and with the corresponding actinide-containing PIM–MD datasets. The ternary results are then compared with estimates obtained by extrapolating the binary Redlich–Kister descriptions through the Muggianu formalism.

5.2.1 NaCl – $CeCl_3$

The density of NaCl – $CeCl_3$ increases continuously with $x(\mathrm{CeCl_3})$, whereas increasing temperature reduces the density (Figure 5.5). The molar volume increases with both $CeCl_3$ fraction and temperature. These trends are consistent with $\rho = M_{\mathrm{mix}}/V_m$: replacing NaCl with the substantially heavier trichloride raises the mixture molar mass more strongly than it raises the molar volume, while thermal expansion increases the volume occupied per mole. The close correspondence with the Sato–Yamamura descriptions compiled by Iwadate [31] shows that the PIM–MD model captures the dominant composition and temperature dependence of the absolute volumetric properties.

The excess molar volume (Figure 5.6) reveals non-ideality that is difficult to distinguish from the nearly linear total molar-volume curves. Positive V_m^E in the NaCl-rich region denotes expansion relative to ideal volume additivity, whereas the negative values at larger trichloride fractions denote

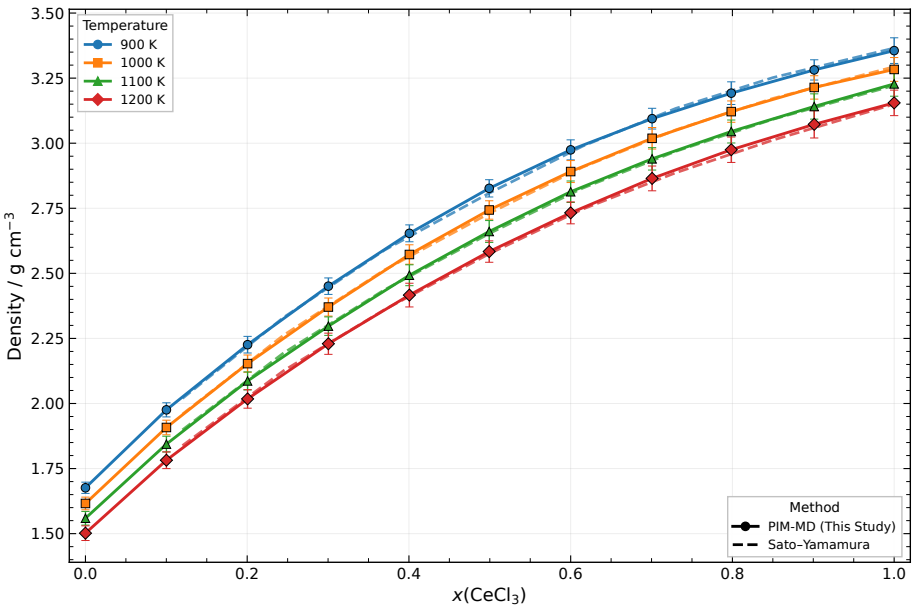

Density

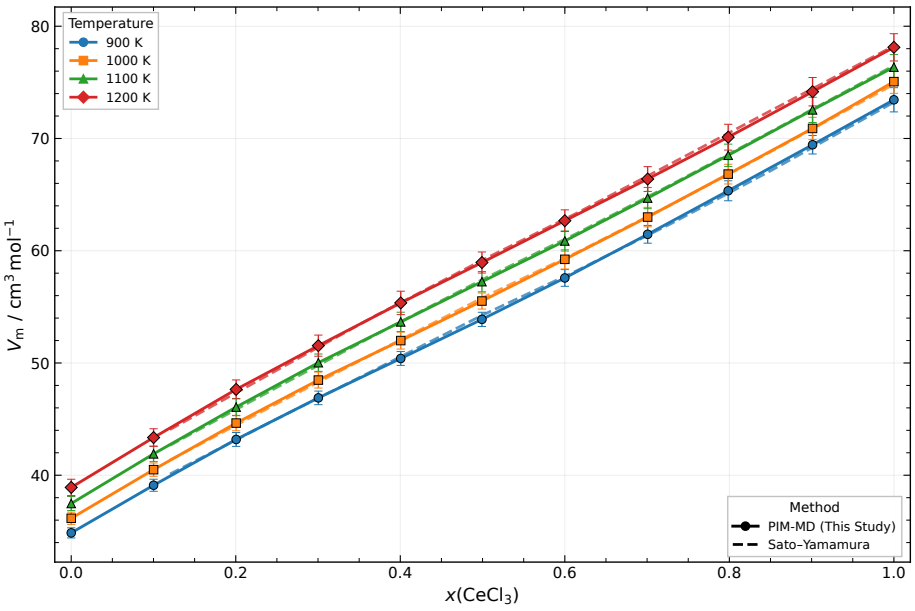

Molar volume

Figure 5.5. Absolute volumetric properties of NaCl – $CeCl_3$. PIM–MD density and molar volume are shown over the complete composition and temperature ranges together with the Sato–Yamamura descriptions compiled by Iwadate [31].

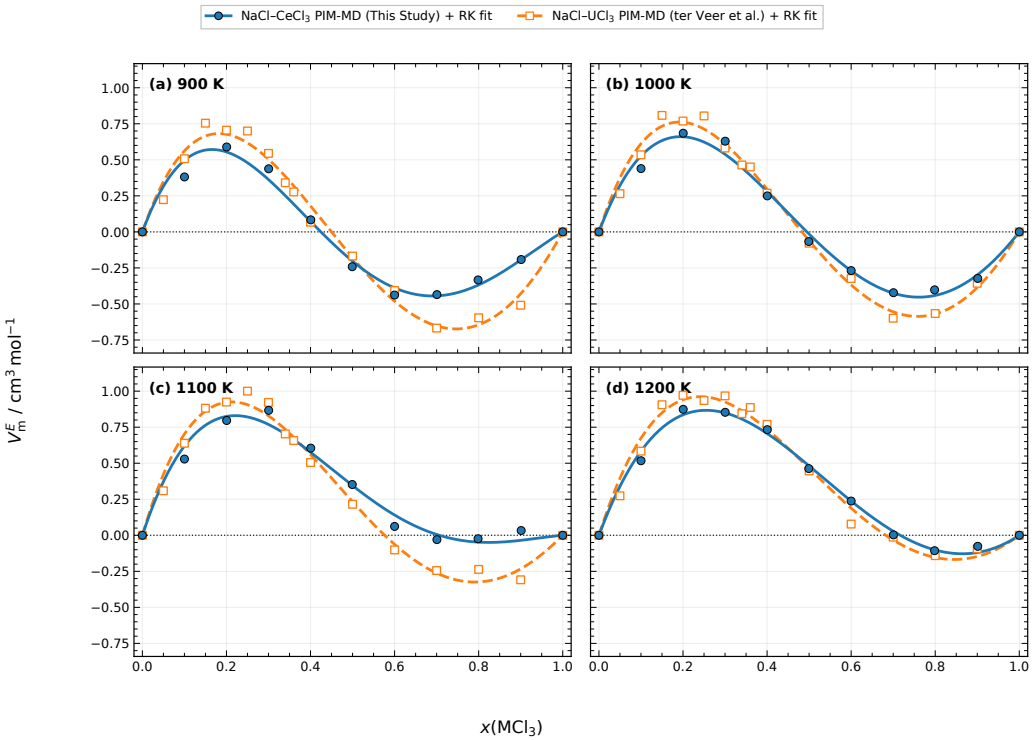

Figure 5.6. Excess molar volume of NaCl – $CeCl_3$ compared with the NaCl – UCl_3 PIM–MD reference data supplied by Ter Veer et al. [84]. Continuous and dashed curves are Redlich–Kister representations of the discrete simulation values.

net contraction. The initial expansion is consistent with the reorganisation required when highly coordinated Ce-centred chloride environments are introduced into a predominantly NaCl-like liquid. Experimental structural measurements show that molten $CeCl_3$ contains distorted, highly coordinated Ce–Cl environments [14]. Increasing the trichloride fraction allows more extensive chloride sharing and changes the connectivity and packing of these environments. The sign change in V_m^E can therefore be interpreted as a crossover between two competing structural contributions. At low $CeCl_3$ content, relatively isolated Ce-centred coordination environments disrupt the NaCl-like packing and require additional local volume, giving $V_m^E > 0$. As the $CeCl_3$ fraction increases, the mean separation between trivalent centres decreases and neighbouring coordination shells increasingly share chloride ions. This allows a more collectively connected arrangement of the chloride network and reduces the volume associated with isolated coordination environments. Once this contraction contribution outweighs the initial NaCl-rich packing disruption, V_m^E becomes negative. The crossover is therefore interpreted as a continuous composition-driven reorganisation of coordination and packing, rather than as evidence for a discrete structural transition.

The NaCl – $CeCl_3$ and NaCl – UCl_3 curves display the same principal composition-dependent form: a positive NaCl-rich maximum, an intermediate sign change and contraction on the trichloride-rich side. The broad agreement in both shape and temperature evolution supports $CeCl_3$ as a useful non-radioactive volumetric simulant for investigating trends relevant to U-bearing molten-salt fuels. The remaining differences in magnitude show, however, that Ce- and U-containing melts should not be treated as numerically interchangeable.

5.2.2 $NaCl - NdCl_3$

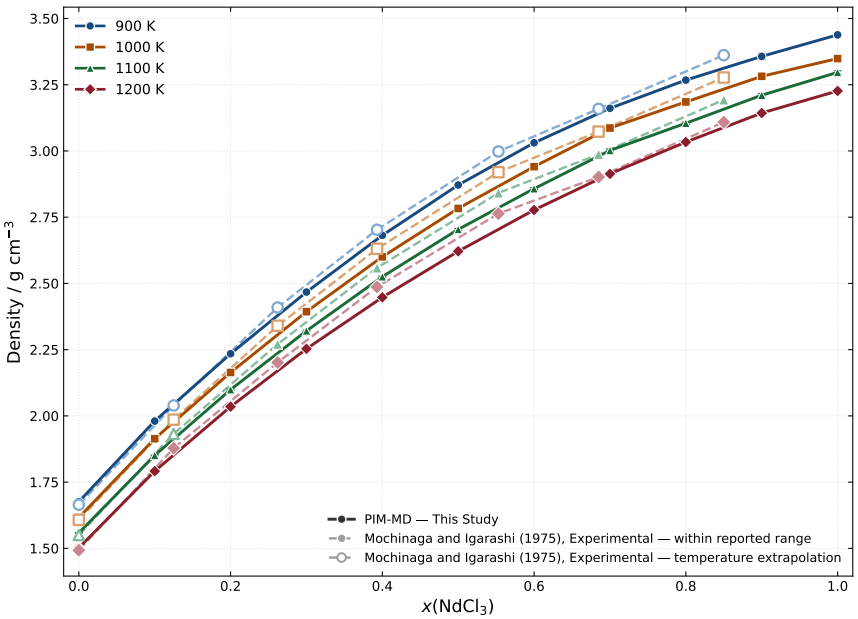

Density

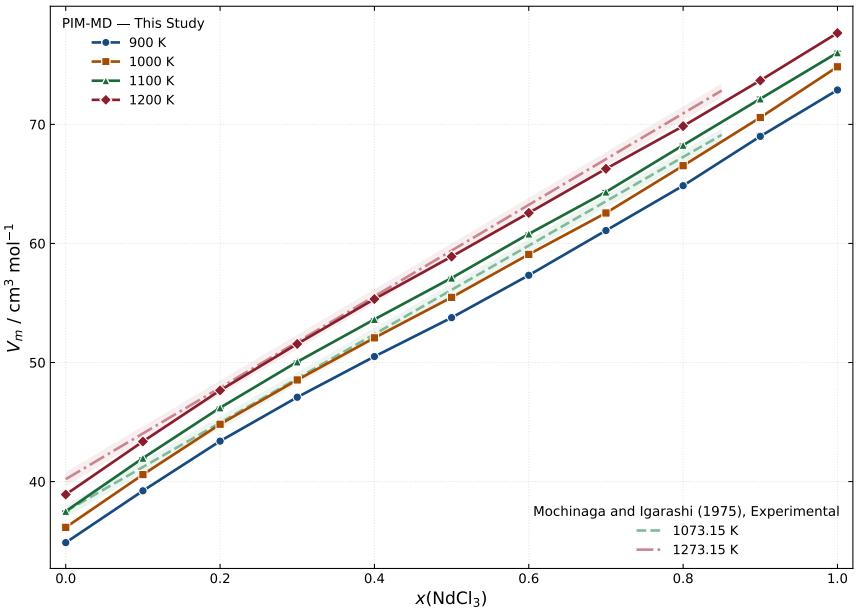

Molar volume

Figure 5.7. Absolute volumetric properties of $NaCl - NdCl_3$. PIM–MD density and molar volume are compared with the measurements and temperature-dependent descriptions of Mochinaga and Igarashi [18].

The $NaCl - NdCl_3$ system displays the same principal absolute-property trends as the Ce-containing binary. Density increases with $x(NdCl_3)$ and decreases with temperature, while molar volume increases with both composition and temperature (Figure 5.7). The PIM–MD predictions closely follow the measurements and derived molar volumes reported by Mochinaga and Igarashi [18]. In that study the molten densities were measured dilatometrically, and the molar volumes were calculated from the measured density data. This agreement indicates that the sim-

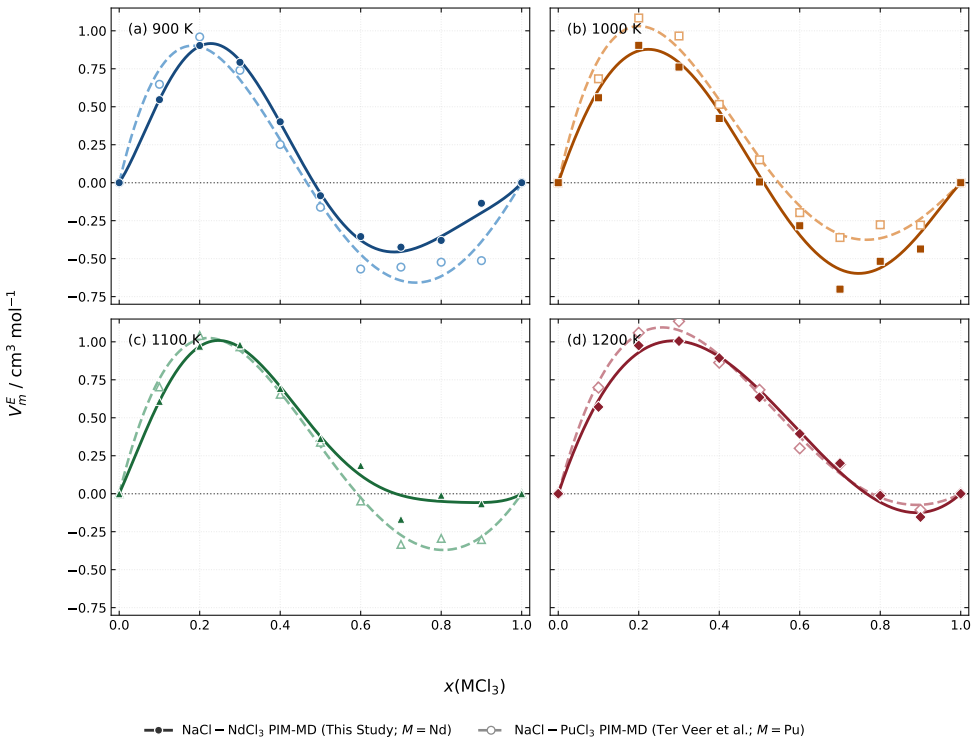

Figure 5.8. Excess molar volume of NaCl – $NdCl_3$ compared with the NaCl – $PuCl_3$ PIM–MD reference data supplied by Ter Veer et al. [84]. Curves are Redlich–Kister representations of the corresponding simulation datasets.

ulations reproduce both the composition-dependent packing of the binary liquid and its thermal expansion over the investigated temperature range.

The excess molar volume (Figure 5.8) again changes from positive values in the NaCl-rich region to negative values at larger $NdCl_3$ fractions. The sign change shows that the mixture cannot be described by a single composition-independent packing correction. At low trichloride content, formation of isolated or weakly connected Nd-centred chloride environments produces expansion relative to ideal volume additivity. As the concentration of trivalent centres rises, chloride sharing and network connectivity become increasingly important, allowing the liquid to adopt a more compact arrangement. Such an interpretation is consistent with the distorted Nd–Cl coordination environments identified experimentally [14] and with the linked-polyhedral structures observed in PIM–MD studies of actinide-bearing chloride mixtures [80].

The close correspondence between the NaCl – $NdCl_3$ and NaCl – $PuCl_3$ excess-volume profiles is particularly relevant to the use of Nd salts as accessible substitutes for Pu-containing materials. Both systems show similar positions of the positive maximum, zero crossing and trichloride-rich minimum, together with broadly comparable temperature dependence. The agreement supports $NdCl_3$ as a useful thermophysical simulant for studying composition-dependent volumetric behaviour relevant to Pu-bearing molten-salt fuels. As for the Ce–U comparison, this is evidence of property-specific similarity rather than proof of complete physicochemical equivalence.

5.2.3 $NaCl - CeCl_3 - NdCl_3$

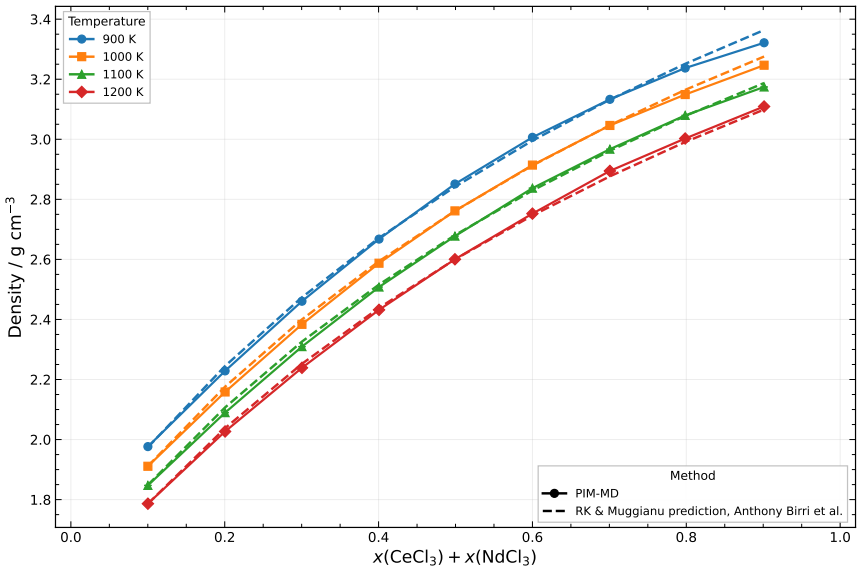

Density

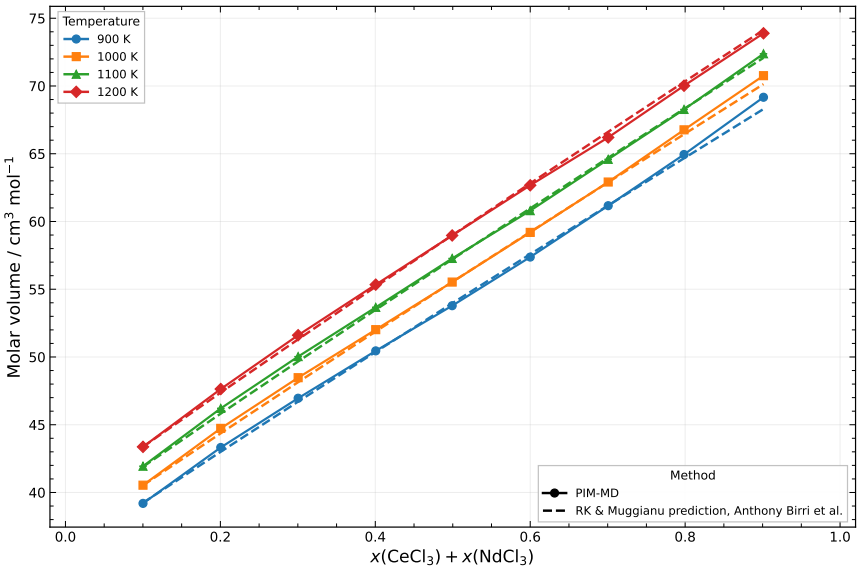

Molar volume

Figure 5.9. Absolute volumetric properties of $NaCl - CeCl_3 - NdCl_3$ along the investigated equal-Ce/Nd path. Direct PIM–MD density and molar volume are compared with the corresponding binary-derived RK–Muggianu predictions.

The ternary density increases with the total trichloride fraction and decreases with temperature, whereas the molar volume increases with both composition and temperature (Figure 5.9). The direct PIM–MD values remain close to the RK–Muggianu predictions for both absolute properties. This agreement indicates that density and total molar volume are dominated by the pure-component and binary contributions, which are retained when the binary Redlich–Kister descriptions are extrapolated into the ternary composition space.

Birri et al. [85] demonstrated the application of binary Redlich–Kister representations and symmetric Muggianu interpolation to higher-order molten-salt density estimation. In the present

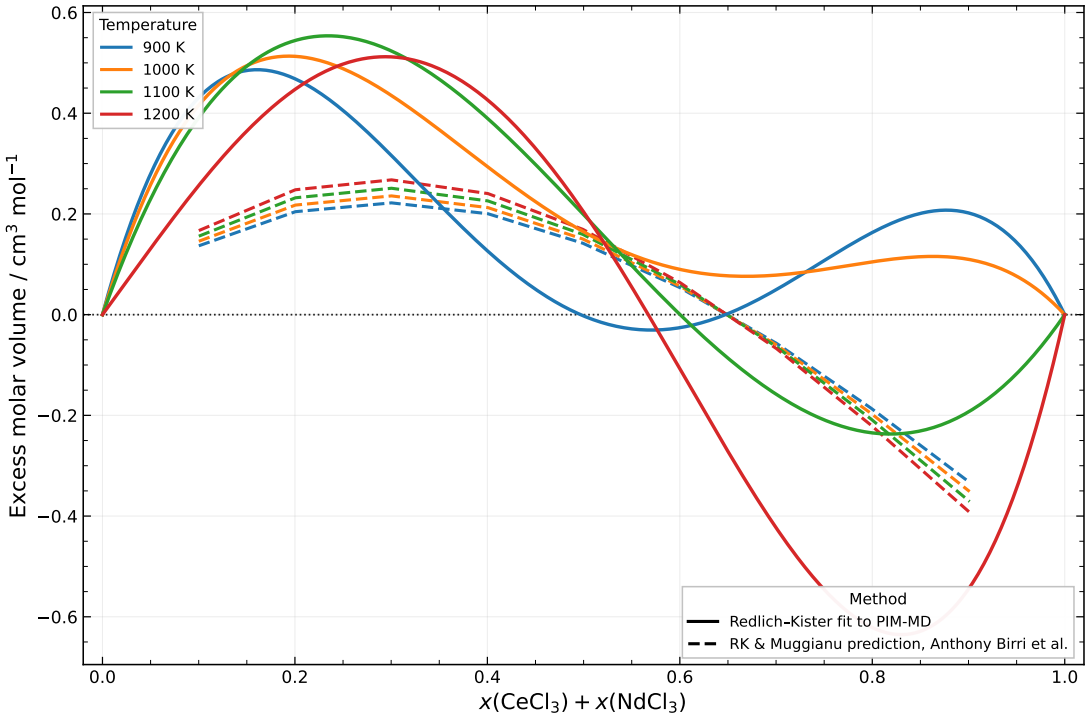

Figure 5.10. Excess molar volume of NaCl – $CeCl_3$ – $NdCl_3$ along the investigated equal-Ce/Nd path. Direct PIM–MD results are compared with predictions obtained from the binary Redlich–Kister descriptions through symmetric Muggianu interpolation following Birri et al. [85]. The RK–Muggianu curves are binary-derived model predictions, not independent experimental measurements of the present ternary system.

work, this method provides a binary-derived baseline against which the directly simulated ternary results can be assessed. It should not be interpreted as experimental validation of the chloride system.

A direct fixed-loading comparison at 900 K provides a more stringent test of whether the equal-Ce/Nd ternary state remains bracketed by the two binary half-loading states at the same total trichloride loading (Figure 5.11). The nominal compositions are $x(\mathrm{CeCl_3}) = 0.50$, $x(\mathrm{NdCl_3}) = 0.50$, and $x(\mathrm{CeCl_3}) = x(\mathrm{NdCl_3}) = 0.25$; because of the integer ion counts in the 2000-ion cells, the realised total trichloride fraction is 0.49925 in all three cases, with the ternary split $x(\mathrm{CeCl_3}) = 0.24888$ and $x(\mathrm{NdCl_3}) = 0.25037$.

The density increases from 2.8266 $\mathrm{g/cm^3}$ for the Ce binary to 2.8511 $\mathrm{g/cm^3}$ for the ternary state and 2.8714 $\mathrm{g/cm^3}$ for the Nd binary. The corresponding molar volumes are 53.885, 53.785 and 53.766 $\mathrm{cm^3/mol}$, respectively. The ternary absolute properties therefore lie close to the binary bracket at fixed total lanthanide loading. The excess molar volume is more discriminating: the Ce binary, ternary and Nd binary values are approximately -0.242, -0.032 and -0.086 $\mathrm{cm^3/mol}$, respectively. The ternary residual is therefore less negative than either binary value, showing that a nearly interpolative absolute volume can coexist with a non-additive excess residual. The Redlich–Kister functions themselves are empirical descriptions of binary non-ideality [69], while the Muggianu construction transfers those binary contributions into a multicomponent composition space.

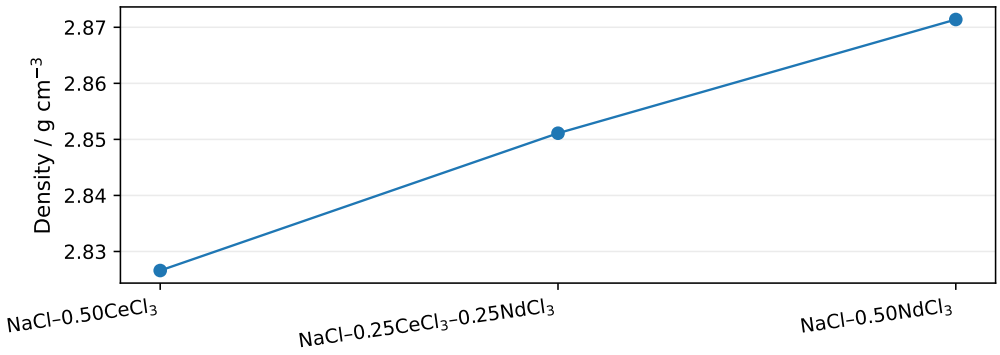

(a) Density.

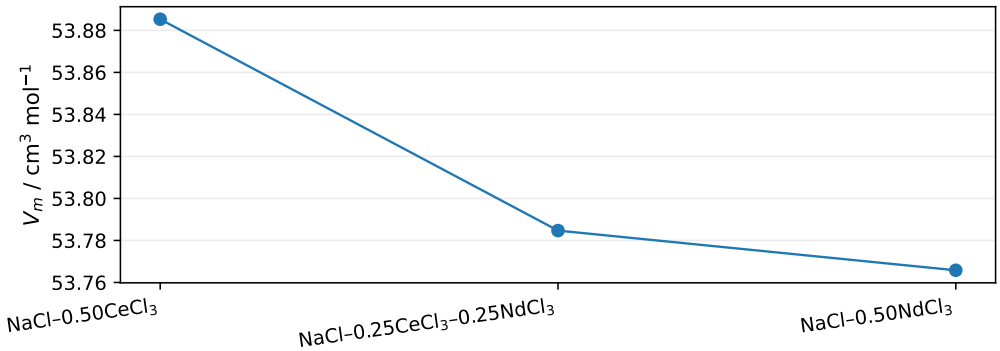

(b) Molar volume.

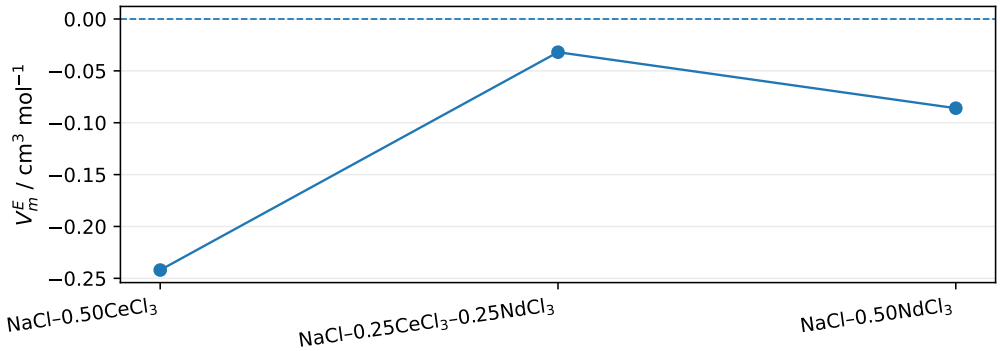

(c) Excess molar volume.

Figure 5.11. Fixed-loading 900 K comparison of the two binary half-loading states and the equal-Ce/Nd ternary state. The two binary states and the equal-Ce/Nd ternary state have the same realised total trichloride fraction, $x(\mathrm{LnCl_3}) = 0.49925$, so no composition interpolation is required. The ternary composition is $x(\mathrm{CeCl_3}) = 0.24888$ and $x(\mathrm{NdCl_3}) = 0.25037$.

The excess molar volume (Figure 5.10) provides a more sensitive comparison than either density or total molar volume. Within the present PIM–MD model, the direct curves display stronger and more temperature-dependent deviations than the binary-based interpolation. This contrast indicates that the small non-ideal volume residual is sensitive to the simultaneous presence of Na, Ce and Nd in a way that is not reproduced fully by the binary RK–Muggianu baseline. Possible microscopic origins include changes in mixed Ce–Cl–Nd coordination, competition for bridging chlorides and redistribution between different linkage environments. Because the Ce–Nd cross interaction is an interpolated modelling choice rather than an independently fitted ternary interaction, these results should be interpreted as model-predicted additional packing contributions, not as proof of an experimentally established ternary excess effect. The RDF, coordination-number and network analyses in Section 5.1 provide the structural context for this model response.

For reactor-scale calculations, the volumetric quantities have direct engineering consequences. Density sets the relation between salt mass, fissile or fertile inventory and occupied fuel volume, while its temperature dependence enters thermal-expansion, buoyancy and natural-circulation calculations. The excess molar volume quantifies the error introduced by assuming ideal volume additivity in multicomponent-property models. The present agreement for the absolute binary properties is therefore encouraging for engineering trend prediction, whereas the model-dependent ternary excess volume should retain the qualification stated above.

5.3 Heat Capacity and Excess Heat Capacity

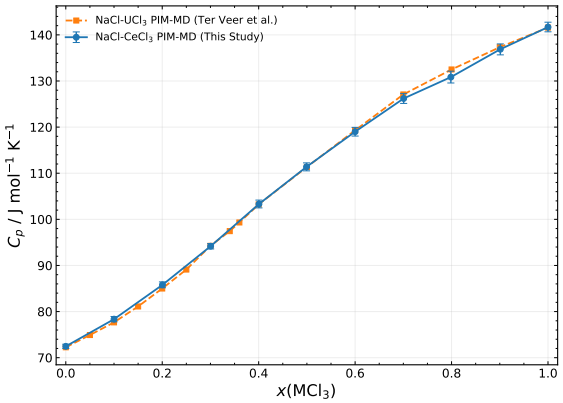

(a) NaCl – $CeCl_3$ compared with the NaCl – UCl_3 benchmark.

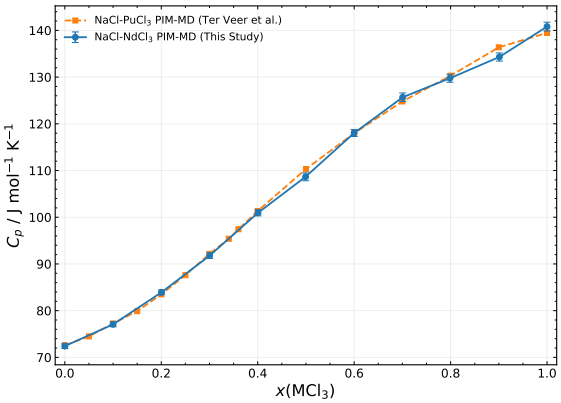

(b) NaCl – $NdCl_3$ compared with the NaCl – $PuCl_3$ benchmark.

Figure 5.12. Interval-average isobaric heat capacities obtained from the PIM-MD simulations over approximately 900–1200 K for the binary lanthanide-chloride systems, compared with the corresponding actinide-chloride benchmark datasets. Error bars represent the propagated 95% confidence intervals.

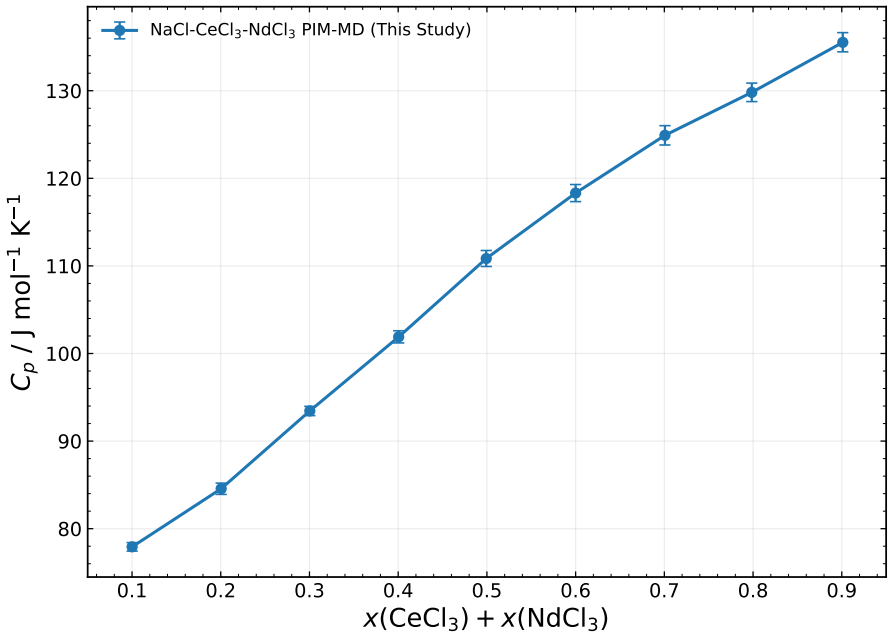

Figure 5.13. Interval-average isobaric heat capacity of the NaCl – $CeCl_3$ – $NdCl_3$ system along the equimolar $CeCl_3$ – $NdCl_3$ composition path. The horizontal coordinate is the total rare-earth chloride fraction, $x(\mathrm{CeCl_3}) + x(\mathrm{NdCl_3})$. Error bars represent the propagated 95% confidence intervals.

The interval-average isobaric heat capacities obtained over approximately 900–1200 K are shown in Figures 5.12 and 5.13. For both binary systems, C_p increases smoothly with the trivalent-chloride fraction. In NaCl – $CeCl_3$, C_p rises from 72.46 ± 0.24 J mol^{-1} K^{-1} for pure NaCl to 141.68 ± 0.53 J mol^{-1} K^{-1} for pure $CeCl_3$. The corresponding increase for NaCl – $NdCl_3$ is from 72.41 ± 0.25 to 140.81 ± 0.48 J mol^{-1} K^{-1}. Along the equimolar $CeCl_3$ – $NdCl_3$ ternary path, C_p

similarly increases from $77.93 \pm 0.25\ \mathrm{J\,mol^{-1}\,K^{-1}}$ at a total rare-earth chloride fraction of 0.10 to $135.52 \pm 0.55\ \mathrm{J\,mol^{-1}\,K^{-1}}$ at a fraction of 0.90.

The monotonic increase partly reflects the molar basis used here: one mole of MCl_3 contains four moles of ions, whereas one mole of NaCl contains two. Increasing the trichloride fraction also introduces strongly coordinated $M^{3+}-Cl^{-}$ environments and a progressively larger configurational contribution to the enthalpy. Experimental investigations of molten $CeCl_3$ and $NdCl_3$ report distorted chloride coordination environments containing approximately six to seven nearest neighbours [14]. The smooth composition dependence and small statistical uncertainties therefore indicate that the PIM-MD simulations resolve the principal energetic changes associated with increasing rare-earth-chloride content.

The calculated total heat capacities agree closely with the actinide-reference datasets. The root-mean-square difference between NaCl – $CeCl_3$ and NaCl – UCl_3 is approximately $0.67\ \mathrm{J\,mol^{-1}\,K^{-1}}$, while the corresponding difference between NaCl – $NdCl_3$ and NaCl – $PuCl_3$ is approximately $0.98\ \mathrm{J\,mol^{-1}\,K^{-1}}$. The maximum relative deviations are approximately 1.25% and 1.52%, respectively, and remain within the 2% uncertainty assigned to the reference curves in the present comparison. The agreement therefore extends beyond the pure-component values and includes the composition dependence of C_p. Independent molecular simulations comparing Ce^{3+}, Nd^{3+} and Pu^{3+} interactions also identify $NdCl_3$ as the more representative plutonium surrogate, although simulant performance remains dependent on the property and composition considered [15].

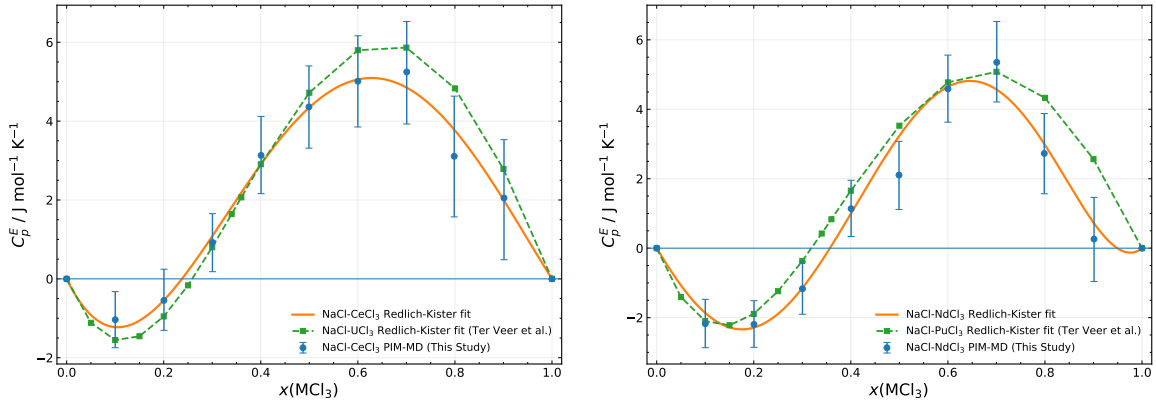

(a) NaCl – $CeCl_3$ compared with the NaCl – UCl_3 benchmark.

(b) NaCl – $NdCl_3$ compared with the NaCl – $PuCl_3$ benchmark.

Figure 5.14. Excess isobaric heat capacities of the binary lanthanide-chloride systems compared with the corresponding actinide-chloride benchmark datasets. The fitted lines denote covariance-aware Redlich–Kister representations of the direct PIM-MD values.

The non-ideal composition dependence is more clearly resolved through the excess heat capacities shown in Figures 5.14 and 5.15. For NaCl – $CeCl_3$, C_p^E is slightly negative on the NaCl-rich side, reaching $-1.04\ \mathrm{J\,mol^{-1}\,K^{-1}}$ near $x(CeCl_3) = 0.10$. It changes sign between $x = 0.20$ and 0.30 and reaches a broad maximum of $5.25\ \mathrm{J\,mol^{-1}\,K^{-1}}$ near $x = 0.70$. The NaCl – $NdCl_3$ system exhibits the same general form but has a more pronounced negative minimum of $-2.20\ \mathrm{J\,mol^{-1}\,K^{-1}}$ near $x(NdCl_3) = 0.20$, followed by a maximum of $5.35\ \mathrm{J\,mol^{-1}\,K^{-1}}$ near $x = 0.70$.

The ternary path follows the same progression. At a total rare-earth fraction of 0.20, the excess heat capacity is $-1.66\ \mathrm{J\,mol^{-1}\,K^{-1}}$. It crosses zero near 0.30 and reaches $4.60\ \mathrm{J\,mol^{-1}\,K^{-1}}$

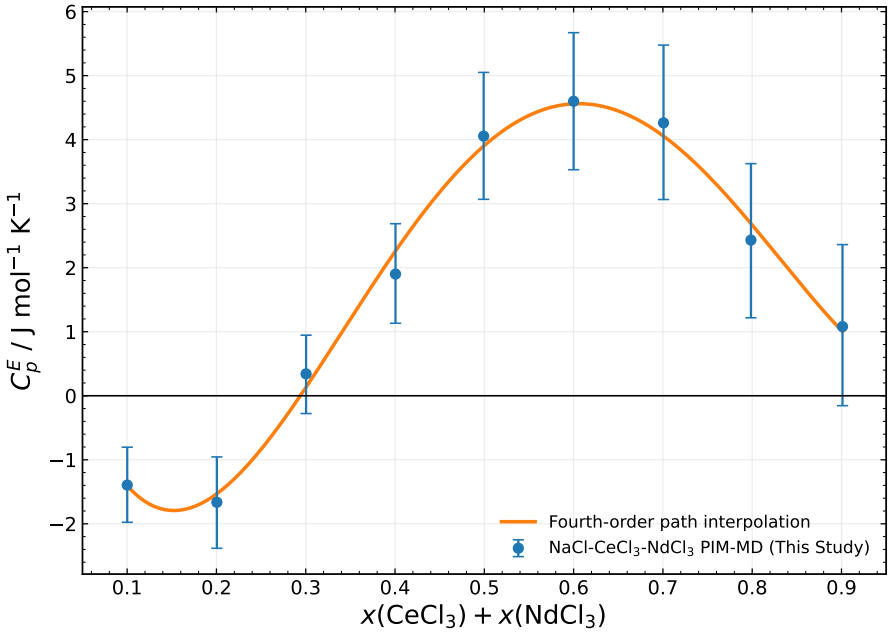

Figure 5.15. Excess isobaric heat capacity of the NaCl – $CeCl_3$ – $NdCl_3$ system along the equimolar $CeCl_3$ – $NdCl_3$ composition path. The horizontal coordinate is $x(CeCl_3) + x(NdCl_3)$. The line represents the covariance-aware fourth-order descriptive interpolation.

at 0.60. Seven of the nine ternary deviations from ideality remain statistically significant after false-discovery-rate correction.

Because

$$C_p^E = \left(\frac{\partial H^E}{\partial T}\right)_P, \tag{5.1}$$

the extrema in C_p^E identify compositions at which the non-ideal enthalpy of mixing is particularly temperature-sensitive; they do not simply locate the compositions with the strongest interionic attractions. This also explains why the sign of C_p^E need not follow that of V_m^E. The excess molar volume measures departure from ideal volume additivity and is therefore primarily sensitive to packing and volume redistribution, whereas C_p^E measures the temperature derivative of excess enthalpy. A negative V_m^E can therefore coexist with a positive C_p^E without any thermodynamic contradiction. A plausible structural interpretation is that isolated or weakly connected rare-earth chlorocomplexes dominate the NaCl-rich region, where NaCl acts as a network-disrupting spacer salt. As the trichloride fraction increases, chloride-sharing coordination polyhedra progressively aggregate into oligomeric and networked structures.

Related PIM-MD studies of NaCl – UCl_3 report the onset of substantial uranium-chloride connectivity above approximately $x(UCl_3) = 0.25$ and the development of a three-dimensional polyhedral network above approximately $x(UCl_3) = 0.40$ [81]. Comparable structural heterogeneity and network disruption by NaCl have been demonstrated in NaCl – $LaCl_3$ melts [34]. The broad positive maxima near trichloride fractions of 0.6–0.7 are therefore consistent with a composition range in which network connectivity and its thermal reorganisation are particularly sensitive to temperature. The subsequent decline towards the rare-earth-rich limit reflects the approach to an

already established trichloride network. For the binary systems, C_p^E must finally approach zero at each pure-component limit by definition. This structural explanation is evaluated further using the RDF, coordination-number and speciation results rather than being inferred from C_p^E alone.

The Redlich–Kister correlations reproduce the binary sign changes and broad maxima while satisfying the pure-component limits. Their residual root-mean-square errors are approximately $0.26\ \mathrm{J\,mol^{-1}\,K^{-1}}$ for NaCl – $CeCl_3$ and $0.45\ \mathrm{J\,mol^{-1}\,K^{-1}}$ for NaCl – $NdCl_3$, comparable to or smaller than the uncertainties of the direct points. The ternary fourth-order interpolation also provides an adequate covariance-aware fit, with a goodness-of-fit probability of 0.67, a reduced χ^2 of 0.59 and a maximum direct residual of $0.36\ \mathrm{J\,mol^{-1}\,K^{-1}}$. The fitted curves are therefore suitable for interpolation within the simulated composition ranges, although the direct PIM-MD values remain the primary evidence.

For reactor applications, neglecting C_p^E would introduce errors of up to approximately 4.3% in the mixture heat capacity around the positive maxima. Heat capacity determines the sensible-heat inventory and contributes to the volumetric thermal inertia of a fuel or coolant salt. It is therefore required in calculations of startup, normal heat removal and transient temperature response. Accurate composition-dependent values are especially important for fuel salts whose composition evolves during operation. The close agreement with the actinide benchmarks supports the use of these lanthanide systems for non-radioactive screening and model development. However, the remaining differences in C_p^E demonstrate that actinide properties should not be replaced by ideal-mixture estimates or transferred from a simulant without a composition-dependent uncertainty assessment [86, 87].

5.4 Mixing Enthalpy and MIVM Analysis

The mixing enthalpies of the two binary systems and the equal-Ce/Nd ternary composition path are shown in Figures 5.16 to 5.18. Both binary systems are exothermic at every investigated interior composition, with the pure-component endpoints fixed by definition at $\Delta H_{\mathrm{mix}} = 0$; all directly simulated states along the equal-Ce/Nd ternary path are likewise negative. The results therefore show strongly non-ideal, exothermic mixing over the sampled mixed-composition states. The binary minima are broad and occur at approximately $x(\mathrm{LnCl_3}) = 0.4$–0.5. At 1100 K, the minimum values are approximately $-11.24\ \mathrm{kJ\,mol^{-1}}$ for NaCl – $CeCl_3$ and $-11.71\ \mathrm{kJ\,mol^{-1}}$ for NaCl – $NdCl_3$, both near a trichloride fraction of 0.4. Along the equal-Ce/Nd ternary path, the minimum at the same temperature is approximately $-11.48\ \mathrm{kJ\,mol^{-1}}$ at a total trichloride fraction of 0.4. At 900 K, the Ce-containing binary and the ternary path instead exhibit a nearly flat minimum extending from approximately 0.4 to 0.5; the statistical uncertainties do not support interpreting this small displacement as a sharp composition transition.

The negative sign shows that the enthalpy of the mixed liquid is lower than the mole-fraction-weighted enthalpy of its pure liquid components. The microscopic origin is not a direct attractive bond between the positively charged Na and lanthanide cations. Rather, mixing redistributes chloride ions and creates energetically favourable, chloride-mediated unlike-cation environments while reorganising the lanthanide–chloride coordination network. This interpretation is supported by the PMF-derived MIVM inputs, but no single sign test on B_{12} or B_{21} is sufficient to determine the mixing enthalpy because the complete MIVM expression combines directional interaction, coordination

and molar-volume terms. The ε_{ij} values are therefore best interpreted as state-dependent effective PMF-well energies, rather than bare pair-potential parameters or isolated chemical-bond energies. The construction of the PMF-derived interaction parameters and the associated sensitivity treatment are documented in Section 4.6.2.

Early calorimetric studies of charge-asymmetric rare-earth chloride mixtures also reported exothermic mixing and commonly discussed the behaviour in terms of stabilised chloro-complex environments [20, 26]. Modern structural studies provide a less restrictive interpretation. In $LaCl_3$ – NaCl, Emerson et al. [34] showed that NaCl acts as a spacer salt and that the trivalent cation occupies an exchanging ensemble of coordination environments rather than one unique, long-lived complex. The present results are consistent with this picture: exothermicity arises from the collective redistribution of chloride, changes in local packing and polarisation, and the formation of chloride-mediated unlike environments, without requiring one discrete stoichiometric species to dominate the liquid.

The location of the minimum follows from the balance between the energetic benefit of unlike local environments and the number of such environments present in the mixture. For a binary system, the mixing enthalpy may be written as

$$\Delta H_{\mathrm{mix}} = x(1-x)\lambda(x), \tag{5.2}$$

where $x = x(\mathrm{LnCl_3})$ and $\lambda(x)$ is a composition-dependent interaction parameter. If λ were constant, the factor $x(1-x)$ would place the minimum at $x = 0.5$. The simulated curves are shifted toward the NaCl-rich side because the effective interaction parameter is more negative in that region. At very low lanthanide content, individual lanthanide-centred environments can be strongly stabilised by the surrounding NaCl-rich liquid, but too few trivalent centres are present for this local stabilisation to dominate the molar enthalpy. At high lanthanide content, the number of trivalent centres is large, but the liquid increasingly resembles the connected structure of the pure trichloride and the number of unlike Na–Ln environments decreases. Near $x(\mathrm{LnCl_3}) \approx 0.4$, NaCl remains the majority component while the lanthanide population and chloride-connected network are already extensive. This composition therefore maximises the product of the number of favourable unlike environments and their energetic benefit.

This interpretation is consistent with the structural crossover identified in Section 5.1. The rapid increase in polymeric lanthanide populations between total trichloride fractions of approximately 0.2 and 0.4 occurs in the same broad composition interval as the most exothermic mixing. The coincidence does not prove that polymerisation alone causes the enthalpy minimum, but it shows that the minimum appears where local chloride coordination and intermediate-range connectivity are changing most strongly. The position near 0.4 should consequently not be interpreted as proof of a liquid compound with a fixed $3\mathrm{NaCl} : 2\mathrm{LnCl_3}$ stoichiometry. It instead marks the optimum balance between dilution, chloride-mediated unlike ordering and recovery of the trichloride network.

Temperature has a smaller effect than composition. In NaCl – $CeCl_3$, the minimum becomes less negative from approximately $-12.28\ \mathrm{kJ\,mol^{-1}}$ at 900 K to $-11.09\ \mathrm{kJ\,mol^{-1}}$ at 1200 K. The ternary minimum changes from approximately -12.08 to $-11.28\ \mathrm{kJ\,mol^{-1}}$ over the same temperature interval. This weakening is consistent with thermal disorder reducing the persistence of composition-

specific local ordering. The NaCl – $NdCl_3$ minima vary more weakly, from approximately -12.05 to $-11.50\ \mathrm{kJ\ mol^{-1}}$, and the differences between 1000 and 1100 K are comparable with the statistical uncertainties. The Nd-containing system is therefore described as exhibiting weak temperature dependence, rather than a strictly monotonic change at every adjacent temperature.

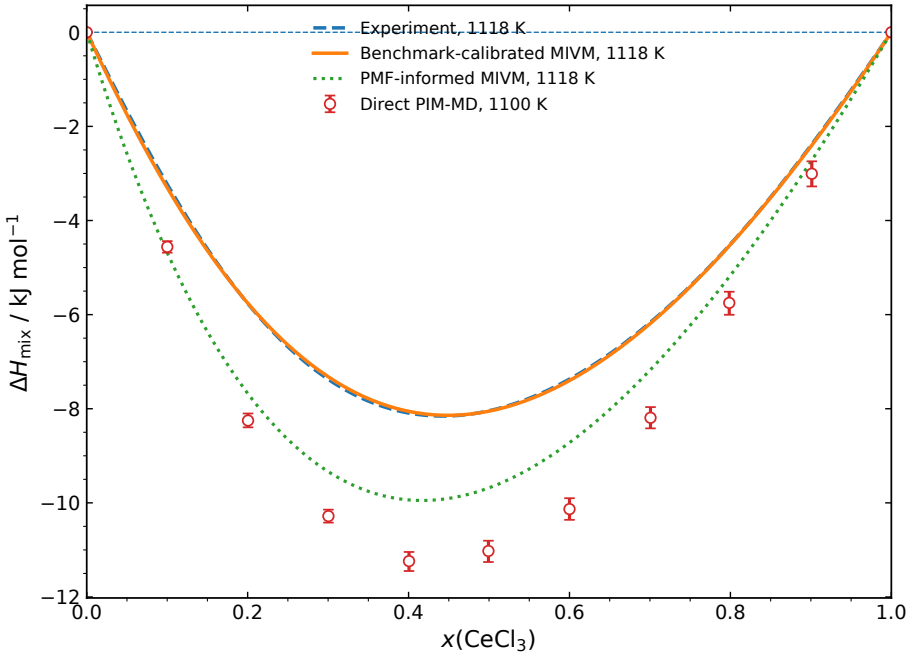

Figure 5.16. Mixing enthalpy of NaCl – $CeCl_3$. Direct PIM–MD values at 1100 K are compared with the calorimetric description of Papatheodorou and Kleppa [26] at 1118 K, the independently parameterised PMF-informed MIVM, and the benchmark-calibrated MIVM. The calibrated curve uses the experimental mixing enthalpy during parameter estimation and therefore represents a semi-empirical reproduction rather than an independent validation.

The direct PIM–MD calculations reproduce the negative sign and the broad intermediate-composition minimum observed experimentally, but systematically overpredict the magnitude of the exothermicity. For NaCl – $CeCl_3$, the 1100 K simulated minimum is approximately $-11.24\ \mathrm{kJ\ mol^{-1}}$, compared with an experimental minimum near $-8.16\ \mathrm{kJ\ mol^{-1}}$ at 1118 K. For NaCl – $NdCl_3$, Gaune-Escard et al. [20] summarize the broad experimental minimum as approximately $-5.7\ \mathrm{kJ\ mol^{-1}}$ near $x(\mathrm{NdCl_3}) = 0.4$, while the most negative individual point among the 16 tabulated measurements used in the present benchmark is $-6.74\ \mathrm{kJ\ mol^{-1}}$ at $x(\mathrm{NdCl_3}) = 0.499$. The simulated 1100 K minimum is approximately $-11.71\ \mathrm{kJ\ mol^{-1}}$. The temperature differences of 18 and 24 K are too small to explain discrepancies of this magnitude, particularly because the simulated temperature dependence is weak. The results therefore indicate systematic over-stabilisation of mixing by the direct simulation route, potentially arising from the force field, the pure-component reference enthalpies, or the reduction of a complex many-body liquid to finite sampled state points.

The PMF-informed MIVM provides an independent structure-to-thermodynamics test. Its parameters are obtained through the sequence

$$g_{ij}(r) \longrightarrow w_{ij}(r) = -RT \ln[g_{ij}(r)/g_{ij,\infty}] \longrightarrow \varepsilon_{ij} \longrightarrow B_{ij} \longrightarrow \Delta H_{\mathrm{mix}}. \tag{5.3}$$

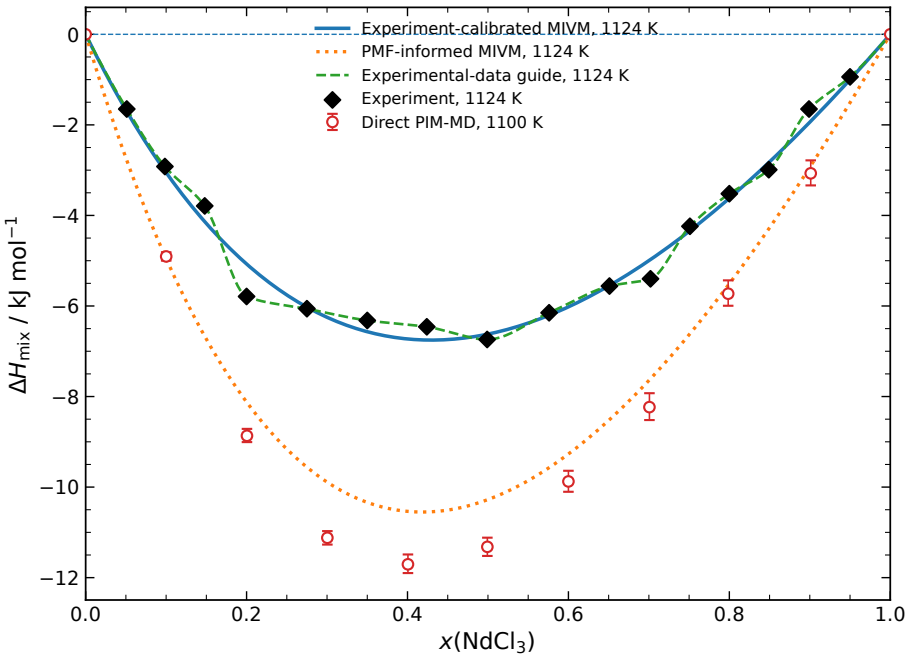

Figure 5.17. Mixing enthalpy of NaCl – $NdCl_3$. Direct PIM–MD values at 1100 K are compared with the 16 calorimetric measurements of Gaune-Escard et al. [20] at 1124 K, a shape-preserving guide through the experimental values, the PMF-informed MIVM, and the MIVM curve calibrated against the complete experimental dataset.

The conversion from the RDF to the PMF is a statistical-mechanical definition; the principal approximation is the subsequent replacement of the complete, composition-dependent PMF profile by a single value at its first minimum. A PMF is an effective free-energy profile for a selected pair in the environment of the surrounding liquid. It therefore contains averaged contributions from local packing, ionic ordering, many-body electronic polarisation, entropy and the remaining degrees of freedom of the melt. A single first-minimum value cannot retain the width of the PMF basin, competing coordination environments, longer-range correlations or the composition dependence of oligomeric and network structures.

The effect of this reduction is amplified by the exponential MIVM definition

$$B_{ij} = \exp\left[-\frac{\varepsilon_{ij} - \varepsilon_{jj}}{RT}\right]. \tag{5.4}$$

A relatively small error in either the unlike or like PMF energy therefore changes B_{ij} multiplicatively and can shift the magnitude and asymmetry of the complete mixing-enthalpy curve. The PMF-informed calculations capture the exothermic sign, general curvature and intermediate-composition minimum, but remain less exothermic than the direct PIM–MD results and do not reproduce the experimental magnitude consistently.

The benchmark-calibrated MIVM agrees more closely with calorimetry because its most sensitive interaction parameters are adjusted directly against the quantity being reproduced. In the present implementation, the PIM–MD-derived coordination numbers Z_i and molar volumes $V_{m,i}$ are retained, whereas B_{12} and B_{21} are fitted to the binary calorimetric mixing enthalpies. These fitted parameters act as effective quantities that absorb deficiencies associated with the simpli-

fied MIVM functional form, composition-dependent PMFs, many-body polarisation, imperfect first-shell reduction, finite RDF sampling and possible force-field errors. Goncharov et al. [72] recently reported the same distinction for a molten $LaCl_3$ – (LiCl – KCl) system: direct AIMD and PIM–MD mixing enthalpies did not reproduce calorimetry, whereas a hybrid MIVM formulation using structural information and experimentally benchmarked interaction parameters recovered the measured behaviour.

The superior agreement of the calibrated curves must consequently not be interpreted as evidence of greater independent predictive power. The PMF-informed MIVM is independently parameterised from atomistic structural and volumetric information and tests whether those descriptors alone are sufficient to predict the macroscopic mixing energetics. The benchmark-calibrated MIVM is a semi-empirical representation and is expected to reproduce the measurements used during its calibration. Presenting both models is nevertheless useful: their difference quantifies the effective correction required to reconcile the structure-based description with calorimetry. The same hybrid logic could be valuable for data-sparse actinide salts, but only after independent validation of parameter transferability; no actinide MIVM calculation is claimed in the present work.

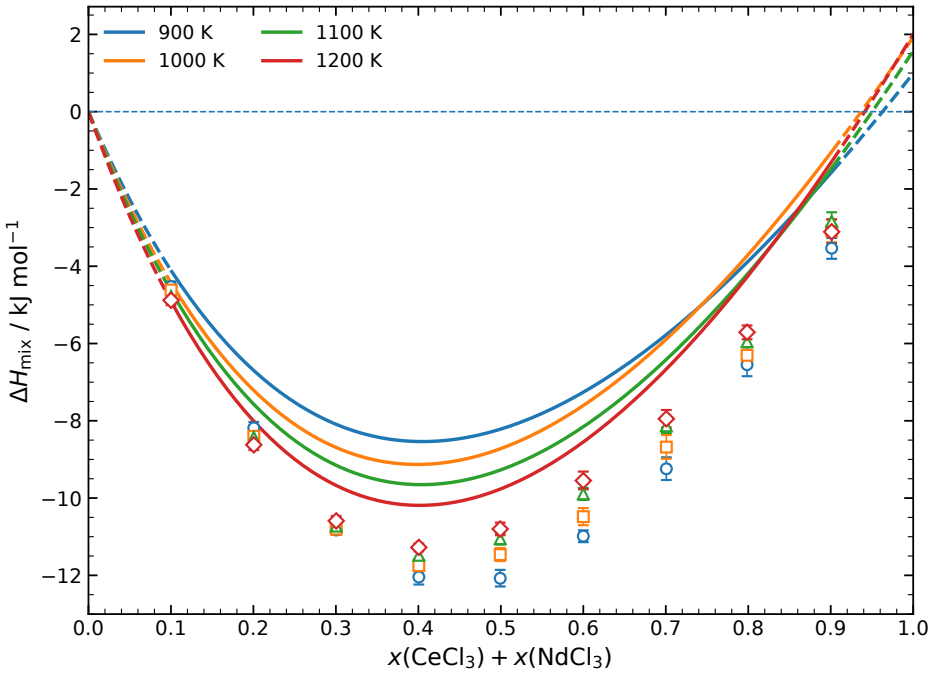

Figure 5.18. Direct PIM–MD and full three-component PMF-informed MIVM mixing enthalpies for NaCl – $CeCl_3$ – $NdCl_3$ along the equal-Ce/Nd composition path. Here, $x(LnCl_3) = x(CeCl_3) + x(NdCl_3)$ and $x(CeCl_3) = x(NdCl_3)$. Solid curves span the directly simulated interval, whereas dashed portions toward the pure-component limits are model extrapolations.

The ternary system follows the same overall composition dependence as the two binaries, and its direct PIM–MD values lie between the corresponding Ce- and Nd-containing binary trends. Within the present PIM–MD/MIVM model, this behaviour is consistent with Na–Ce and Na–Nd chloride-mediated environments providing the dominant binary-like contribution, while no large additional Ce–Nd stabilisation is resolved along the investigated path. The full three-component

PMF-informed MIVM reproduces the negative sign and broad minimum but, as in the binaries, underestimates the magnitude of the direct exothermicity.

No ternary calorimetric dataset was used in this work. The ternary treatment must therefore remain labelled PMF-informed rather than experimentally calibrated. In addition, the simulations cover only the equal-Ce/Nd section of the composition space and cannot establish the behaviour over the complete ternary triangle. The dashed end regions in Figure 5.18 are extrapolations of the MIVM model and must not be interpreted as additional simulated states. Within these limits, the ternary results indicate approximately binary-additive energetics along the investigated path and provide a consistent bridge between the binary calorimetric comparisons and the mixed-lanthanide structural analysis.

5.5 Thermal Conductivity

The thermal conductivity was evaluated using the structural-coherence model introduced in Chapter 4, in which the ability of the liquid to store thermal energy, the propagation speed of collective disturbances and the spatial extent of structural correlations are represented through $C_{p,\mathrm{vol}}$, v_s and ℓ_{sc}, respectively. The model links the RDF-derived coherence length to an effective energy-carrier mean free path and has recently been applied to dissociated, complex-forming and actinide-bearing molten salts [45]. Accordingly, the results below should be interpreted as physically informed model predictions rather than direct Green–Kubo evaluations of the heat current. This distinction is important because local complex formation and chemical disorder can modify thermal transport in multicomponent ionic liquids [88].

5.5.1 Binary Melts and Actinide Benchmarks

The calculated NaCl – $CeCl_3$ conductivities span approximately 0.218–$0.870\ \mathrm{W/(m\,K)}$ and show a strongly non-linear composition dependence, including a broad low-conductivity intermediate-composition region rather than a simple linear mixing response (Figure 5.19). At 900 K, adding only $x(\mathrm{CeCl_3}) = 0.10$ lowers the predicted conductivity from 0.870 to $0.355\ \mathrm{W/(m\,K)}$, and the minimum of $0.280\ \mathrm{W/(m\,K)}$ occurs at $x(\mathrm{CeCl_3}) = 0.20$. The minimum remains near 0.20 at 1000 K but shifts towards $x(\mathrm{CeCl_3}) = 0.40$ at 1100 and 1200 K. Beyond the minimum, the conductivity generally recovers towards the $CeCl_3$-rich endpoint. Most mixed compositions also display a negative temperature dependence, although the behaviour is not strictly monotonic at every state point.

The intermediate-composition minimum is not assigned to one rigid stoichiometric complex. Instead, it marks a balance between two structural limits. In the NaCl-rich region, the introduction of strongly coordinating Ce^{3+} centres rapidly disrupts the comparatively long-ranged collective environment of the carrier salt. At higher $CeCl_3$ content, chloride-sharing Ce-centred environments become sufficiently abundant for a more connected trichloride-like liquid to develop, allowing partial recovery of the structural coherence length. The location of the minimum therefore corresponds to the composition range in which the NaCl-like transport network has already been strongly disrupted but the Ce-rich network has not yet recovered comparable coherence. The shift of the minimum towards larger $x(\mathrm{CeCl_3})$ at higher temperature is consistent with stronger thermal disordering,

such that a larger trichloride population is required before the Ce-rich recovery becomes apparent. This is a structure-consistent interpretation rather than proof of a unique microscopic mechanism.

At $x(MCl_3) = 0.40$, NaCl – $CeCl_3$ follows the same negative temperature dependence as the NaCl – UCl_3 results supplied by Ter Veer et al. [84] (Figure 5.20). The Ce-containing values are higher than the U-containing benchmark by approximately 8.7–21.2% over 900–1200 K, with a mean absolute relative difference of 13.9%. This agreement supports trend-level thermal-transport similarity within the common PIM–MD/structural-coherence framework, but it does not establish absolute experimental accuracy.

Available measurements for molten $CeCl_3$ – NaCl provide a more demanding absolute test. Bobrova and Dokytovich [89] reported thermal conductivities for $CeCl_3$-alkali-chloride melts that increase with temperature, whereas the present SCM estimates are predominantly decreasing. The direct comparison is shown in Figure 5.20. At 1173 K, the calculated values are approximately 60–67% below the reported correlations at the intermediate experimental compositions and approximately 35% below the pure-$CeCl_3$ value. These discrepancies are much larger than the numerical post-processing sensitivity of the present workflow. The comparison therefore sets a clear boundary on the model: the SCM is useful here for relative composition and analogue trends, but the available NaCl – $CeCl_3$ measurements do not validate its absolute conductivity scale.

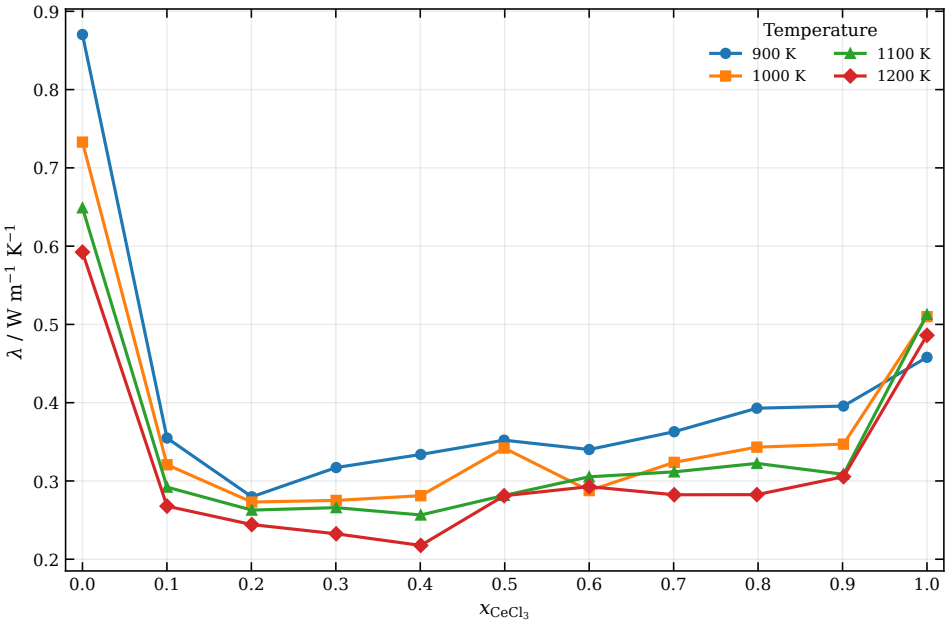

Figure 5.19. Predicted NaCl – $CeCl_3$ thermal conductivity at 900, 1000, 1100 and 1200 K from the structural-coherence model. The pure-NaCl points at 900 and 1000 K are metastable-liquid simulations below the experimental melting temperature. Connecting lines are guides to the eye.

The NaCl – $NdCl_3$ system exhibits the same broad response (Figure 5.21). The predicted values span 0.211–0.810 $W/(m\,K)$, with a sharp decrease on introducing $NdCl_3$, minima within $x(NdCl_3) = 0.20$–0.40, and recovery towards pure $NdCl_3$. The minimum occurs at 0.30, 0.40, 0.20 and 0.30 at 900, 1000, 1100 and 1200 K, respectively. The absence of a single fixed minimum composition shows that thermal conductivity is controlled by the product of several composition-dependent quantities rather than by one structural descriptor alone.

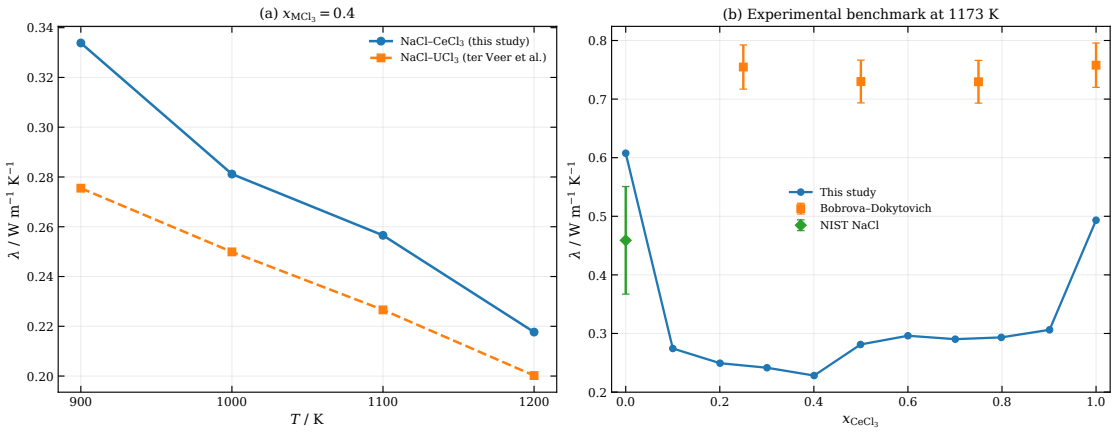

Figure 5.20. Validation of the structural-coherence thermal-conductivity estimates. Panel **(a)** compares the present NaCl – $CeCl_3$ calculation with the NaCl – UCl_3 PIM–MD/SCM benchmark of Ter Veer et al. [84] at $x(MCl_3) = 0.40$. Panel **(b)** compares the 1173 K composition dependence with the experimental NaCl – $CeCl_3$ data of Bobrova and Dokytovich [89]; the pure-NaCl reference point follows the recommended molten-NaCl correlation of Chliatzou et al. [90]. The experimental comparison is the principal absolute test of the SCM values in this thesis.

The component decomposition clarifies the dominant origin of the U-shaped binary trend. The composition-weighted coherence length decreases from about 6.0 Å in pure NaCl to approximately 2.8–3.0 Å over the intermediate composition range, before increasing to approximately 6.5 Å in pure $NdCl_3$. The volumetric heat capacity changes comparatively little, while the adiabatic sound velocity provides an additional, but less uniformly non-linear, contribution. The conductivity minimum therefore appears where the coherence of the NaCl-rich liquid has been lost and the connected Nd-rich environment has not yet fully developed. Supporting plots of $C_{p,\mathrm{vol}}$, v_s and ℓ_{sc}, together with the sensitivity analysis, are provided in the appendix. The heavier trivalent cations also contribute indirectly through the sound-speed factor: from $v_s = (\rho\kappa_S)^{-1/2}$, an increase in mass density tends to reduce v_s if the adiabatic compressibility does not compensate. This is not a standalone cation-mass law, because κ_S and local chemistry vary at the same time. In the present decomposition, the pronounced U-shaped composition response is therefore attributed primarily to the non-linear change in ℓ_{sc}, with v_s providing a secondary thermodynamic modulation. The interpretation is deliberately liquid-state based; the SCM does not require literal crystal phonons or a phonon-scattering mechanism.

At $x(MCl_3) = 0.40$, the Nd-containing predictions remain above the NaCl – $PuCl_3$ benchmark of Ter Veer et al. [84] but reproduce its negative temperature dependence (Figure 5.21b). The relative difference is approximately 8.5–17.5%, with a mean absolute relative difference of 12.0%. As for the Ce–U comparison, the agreement is therefore strongest at the level of temperature dependence and order of magnitude. It supports the use of $NdCl_3$ as a qualitative thermal-transport analogue for $PuCl_3$, while retaining a systematic positive bias in the predicted conductivity.

Same-system experimental evidence is available, but substantially sparser than for the Ce binary. Dokutovich et al. [25] measured the thermal conductivity of pure $NdCl_3$ and an equimolar $0.5NdCl_3 - 0.5NaCl$ melt, together with selected KCl- and CsCl-containing mixtures. The accessible published record establishes these measured state points and their temperature-dependent character, but does not provide a sufficiently detailed numerical table for a traceable composition-resolved

curve to be reconstructed here without introducing unverifiable digitisation. The experiment is therefore retained as a same-system validation anchor rather than converted into an artificial continuous benchmark.

This limitation also constrains how literally the exact positions of the predicted Nd conductivity minima should be interpreted. The broad intermediate-composition suppression and the coherence-length response are numerically robust to the production-window and RDF-smoothing tests in Section A.4, but the individual minimum at each temperature remains an SCM model prediction rather than an experimentally established stoichiometric feature.

5.5.2 Equal-Ce/Nd NaCl – $CeCl_3$ – $NdCl_3$ Path

Along the equal-Ce/Nd ternary path, $x(\mathrm{CeCl_3}) = x(\mathrm{NdCl_3})$, the predicted conductivity is both lower and substantially flatter than the complete binary curves, forming a broad low-conductivity response across the investigated composition path (Figure 5.22). Across the 36 simulated states, λ ranges from 0.192 to $0.339\ \mathrm{W/(m\,K)}$. At 1100 K, for example, the conductivity changes only from 0.268 at $x(\mathrm{LnCl_3}) = 0.10$ to $0.228\ \mathrm{W/(m\,K)}$ at $x(\mathrm{LnCl_3}) = 0.90$, with comparatively small intermediate variations. The predominantly negative temperature dependence is retained, but the strong trichloride-rich recovery observed in the binaries is absent.

This difference follows directly from the structural-coherence decomposition. The ternary coherence length remains within approximately 2.68–2.94 Å over the investigated path. For scale, the pure-NaCl binary endpoint provides a substantially longer-coherence reference of about 6 Å in the same analysis framework. The ternary coherence length itself increases only modestly with total lanthanide content and never approaches the values above 6 Å reached as the binary systems approach their pure trichloride endpoints. Simultaneous Ce and Nd populations therefore preserve a chemically heterogeneous chloride environment while the composition path never becomes a single-cation trichloride liquid. The accompanying decline in sound velocity at high $x(\mathrm{LnCl_3})$ then suppresses the recovery that would otherwise follow from the modest increase in ℓ_{sc}.

The ternary behaviour is consequently consistent with sustained disruption of collective energy-transfer pathways by mixed Ce- and Nd-centred coordination environments. This statement remains deliberately cautious. The statistical analysis shows that structural descriptors correlate with conductivity, but do not necessarily provide independent predictive power after temperature and curved composition dependence are controlled. The 900 K temporal-persistence analysis reported in Section 5.6.3 shows smoothly increasing bridge recurrence with total lanthanide content and no exceptional stabilisation of mixed Ce–Cl–Nd linkages. That dynamical evidence is consistent with a heterogeneous but labile network; it does not, however, identify a unique energy-transport mechanism because no heat-current correlation was evaluated. Moreover, no directly usable experimental thermal-conductivity dataset was identified for the target ternary system, so the prediction is validated only indirectly through the binary and actinide comparisons.

Taken together, the three systems show that adding a trivalent chloride strongly reduces the thermal conductivity of NaCl-rich melts, while the subsequent high-composition response depends on whether a coherent single-trichloride environment can develop. The binary systems display intermediate-composition minima followed by recovery towards their pure trichlorides. The equal-Ce/Nd ternary path retains short coherence lengths and therefore lacks an equivalent

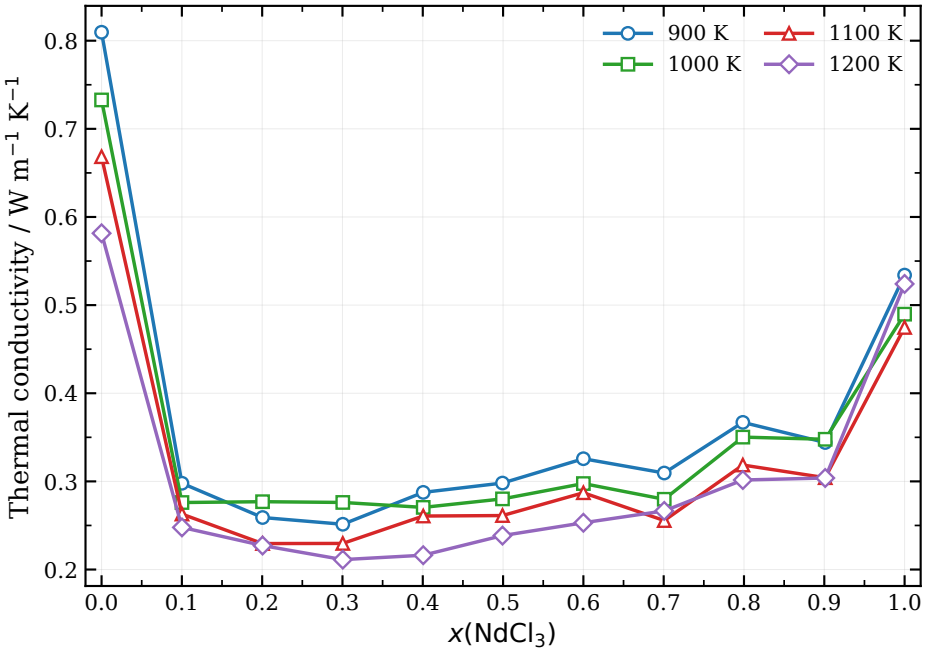

(a) Composition dependence of NaCl – $NdCl_3$.

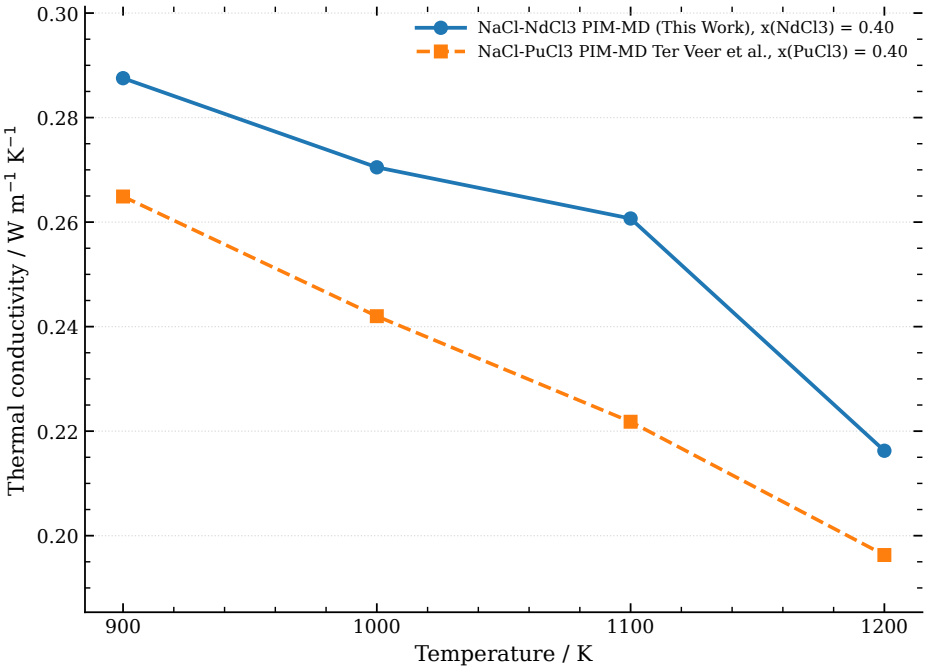

(b) Comparison with NaCl – $PuCl_3$ at $x(MCl_3) = 0.40$.

Figure 5.21. Predicted thermal conductivity of NaCl – $NdCl_3$. Panel **(a)** shows the composition dependence at 900, 1000, 1100 and 1200 K. Panel **(b)** compares the present NaCl – $NdCl_3$ results with the NaCl – $PuCl_3$ PIM–MD/SCM benchmark supplied by Ter Veer et al. [84] at $x(MCl_3) = 0.40$. Connecting lines are guides to the eye.

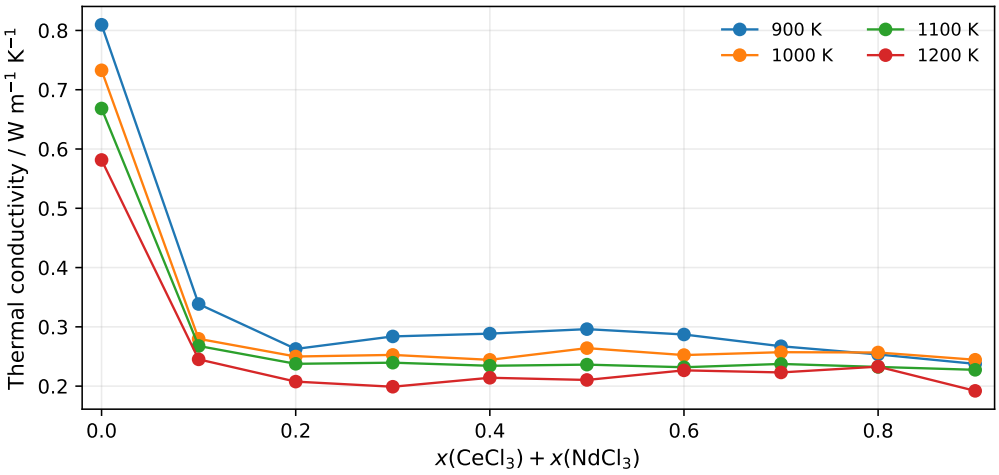

(a) SCM thermal conductivity.

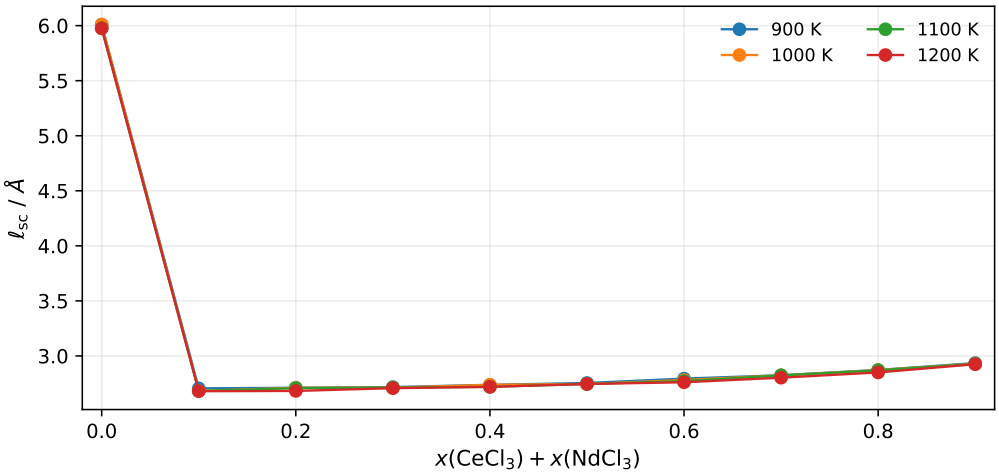

(b) Composition-weighted structural-coherence length.

Figure 5.22. Equal-Ce/Nd NaCl – $CeCl_3$ – $NdCl_3$ SCM response at 900, 1000, 1100 and 1200 K, augmented with the pure-NaCl endpoint from the NaCl – $NdCl_3$ SCM workflow as a scale reference. Panel **(a)** shows thermal conductivity and panel **(b)** shows ℓ_{sc}. The pure-NaCl 900 and 1000 K points are metastable-liquid simulations below the experimental melting temperature; the endpoint is included to quantify the coherence loss, not as an additional ternary simulation. Detailed numerical sensitivity is retained in Section A.4.

recovery. The Ce–U and Nd–Pu comparisons support relative simulant behaviour within the common modelling framework, but the substantial underprediction of the available NaCl – $CeCl_3$ measurements demonstrates that absolute accuracy remains model dependent. The conductivity results are therefore most defensibly used to compare composition trends, temperature responses and simulant behaviour, with the component decomposition and numerical sensitivity retained in the appendix.

5.6 Molten Salt Viscosity

The viscosity discussion is based exclusively on the final 5 ns production trajectories. Equilibrium Green–Kubo viscosity is particularly sensitive to slowly relaxing stress fluctuations, so a small formal spectral uncertainty does not by itself demonstrate trajectory convergence [64, 78]. The protocol in Section 4.7.4 therefore combines trajectory-length, shifted-window and spectral-cutoff tests. State points satisfying the primary criteria, or confirmed through the additional sensitivity checks, are treated as reportable and shown as ordinary points. State points for which convergence was not demonstrated remain provisional and are shown with crossed markers. The complete diagnostic classifications are retained in Section A.5.

5.6.1 Binary NaCl – $NdCl_3$

Five-Nanosecond Viscosity Trends

The corrected NaCl – $NdCl_3$ production dataset contains all 44 combinations of 11 compositions and four temperatures. Of these, 40 state points satisfy the adopted reporting protocol. Convergence was not demonstrated for $x(NdCl_3) = 0.30$ and 0.90 at 900 K, $x(NdCl_3) = 0.70$ at 1000 K, and pure $NdCl_3$ at 1100 K. The remaining states are reportable, including those confirmed through additional trajectory-window and spectral-sensitivity checks.

The complete four-temperature dataset shows a consistent macroscopic response: viscosity decreases with temperature and increases broadly as $NdCl_3$ replaces NaCl (Figure 5.23). At 900 K the viscosity increases from 1.513 ± 0.028 mPa s for pure NaCl to 9.113 ± 0.367 mPa s for pure $NdCl_3$. At 1000 K, the corrected dataset spans 1.387 ± 0.029–5.909 ± 0.207 mPa s, while at 1200 K the corresponding range is 0.923 ± 0.017–3.350 ± 0.101 mPa s. The stronger composition contrast at lower temperature is consistent with slower structural rearrangement in the more highly connected trichloride-rich liquid.

The corrected 1000 K series provides an important consistency check because it fills the only previously missing temperature slice. Six compositions required additional shifted-window analysis. The initially cutoff-sensitive $x(NdCl_3) = 0.60$ state was confirmed as stable by the shifted-window test, whereas $x(NdCl_3) = 0.70$ retained substantial time-window dependence and is therefore kept provisional. The other sensitivity-checked 1000 K states remain suitable for reporting. Thus the full four-temperature dataset supports the same broad composition and temperature trends without relying on interpolation of the corrected state points.

Small neighbouring decreases occur at a few compositions, but the accepted uncertainties and convergence checks do not support interpreting them as resolved local extrema. At 900 K, for example, the decrease from $x(NdCl_3) = 0.70$ to 0.80 is only 0.158 mPa s ($z = -0.47$), while the

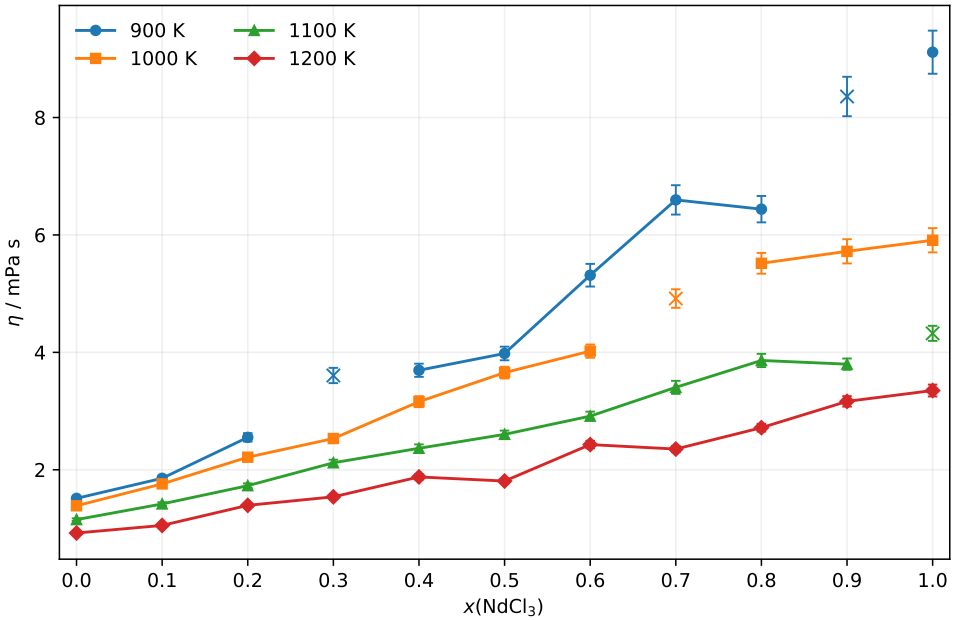

Figure 5.23. Composition dependence of the 5 ns NaCl – $NdCl_3$ shear viscosity at 900–1200 K. Error bars denote the reported SporTran uncertainty. Crossed markers identify the four provisional states for which convergence was not demonstrated. Lines connect only reportable values and are guides to the eye.

two small decreases at 1200 K remain below two combined standard uncertainties. The defensible result is therefore a broad composition-driven rise in viscosity rather than a sequence of established intermediate-composition maxima and minima.

Experimental Validation and Pu Benchmark

The available reference evidence was used at two distinct levels. The pure $NdCl_3$ endpoint was compared with the same-system experimental correlation of Potapov and Sato [65], whereas the mixture comparison with NaCl – $PuCl_3$ from Ter Veer et al. [66] tests simulant behaviour at the matched trichloride fraction $x(MCl_3) = 0.37$. The present NaCl – $NdCl_3$ values at $x = 0.37$ were obtained by the local interpolation in Equation (4.48); only temperatures for which both $x = 0.30$ and 0.40 states are reportable are included.

Table 5.2. Same-system experimental validation and matched-composition Pu benchmark for the 5 ns NaCl – $NdCl_3$ viscosity. The pure-$NdCl_3$ reference is the correlation of Potapov and Sato [65]; its 1000 K value is a short 25 K extrapolation below the reported measurement range. The $x = 0.37$ NaCl – $PuCl_3$ values are from Ter Veer et al. [66]. The relative difference is defined by Equation (4.50).

Benchmark	$x(MCl_3)$	T / K	η_{this} / mPa s	η_{ref} / mPa s	δ_η / %
Pure $NdCl_3$, experiment	1.00	1000	5.909 ± 0.207	6.271	−5.8
NaCl – $PuCl_3$, PIM-MD	0.37	1000	2.972 ± 0.068	4.412 ± 0.642	−32.6
NaCl – $PuCl_3$, PIM-MD	0.37	1100	2.292 ± 0.049	2.863 ± 0.393	−19.9
NaCl – $PuCl_3$, PIM-MD	0.37	1200	1.776 ± 0.033	2.362 ± 0.318	−24.8

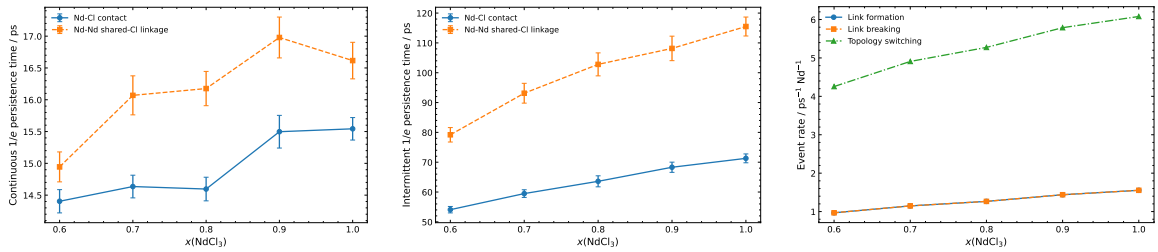

(a) Continuous $1/e$ persistence. **(b)** Intermittent $1/e$ persistence. **(c)** Linkage-event rates.

Figure 5.24. Composition dependence of the 900 K NaCl – $NdCl_3$ temporal descriptors for $x(NdCl_3) = 0.60$–1.00. Persistence error bars denote variability across nine sequential 0.5 ns windows and are not independent-replica uncertainties.

The reportable pure-$NdCl_3$ value at 1000 K is 5.8% below the short extrapolation of the experimental correlation. At 1100 K the simulation value would differ from the experimental correlation by only 2.1%, but that state is provisional and is therefore not used as primary validation evidence. These endpoint comparisons support the absolute viscosity scale of the Nd model but do not validate the complete binary composition dependence.

At $x(MCl_3) = 0.37$, the reportable Nd/Pu comparisons give relative differences of -32.6, -19.9 and -24.8% at 1000, 1100 and 1200 K, respectively, corresponding to a descriptive MARD of 25.8%. The lanthanide values are lower at all three retained temperatures. When the reported uncertainties of both datasets are combined, the 1000 K difference exceeds two combined standard uncertainties, whereas the 1100 and 1200 K differences do not. The result therefore supports broadly comparable temperature dependence but not quantitative Nd/Pu equivalence in viscosity at this composition.

Temporal Persistence of the Nd-Centred Network

The macroscopic viscosity trend is consistent with the progressive development of an Nd-centred, chloride-mediated network. Increasing $x(NdCl_3)$ changes the Nd–Cl coordination environment and increases the prevalence of shared-chloride Nd–Nd connections, linking the transport response to the connectivity trends discussed in Section 5.1. Similar relationships between first-shell dynamics, trivalent-cation network formation and shear relaxation have been identified in related alkali–trivalent halide mixtures [33].

Direct dynamical support was obtained from the dedicated 900 K analysis for $x(NdCl_3) = 0.60$–1.00. Each exact 5 ns trajectory was evaluated over nine sequential, non-overlapping 0.5 ns windows spanning 0.2–4.7 ns. The analysis quantified continuous and intermittent Nd–Cl contact persistence, Nd–Nd shared-chloride linkage persistence, topology-resolved lifetimes and linkage-event rates. These windows are blocks of one trajectory rather than independent replicas.

The uninterrupted lifetimes change only modestly: continuous Nd–Cl persistence increases from 14.40 to 15.54 ps and continuous Nd–Nd shared-chloride persistence from 14.94 to 16.62 ps between $x = 0.60$ and 1.00. The intermittent response is substantially stronger. Nd–Cl persistence increases from 54.08 to 71.29 ps and Nd–Nd shared-chloride persistence from 79.19 to 115.49 ps, corresponding to endpoint increases of approximately 31.8% and 45.8%. Simultaneously, the topology-switching rate rises from 4.255 to 6.079 $ps^{-1}\,Nd^{-1}$ while formation and breaking rates remain closely balanced.

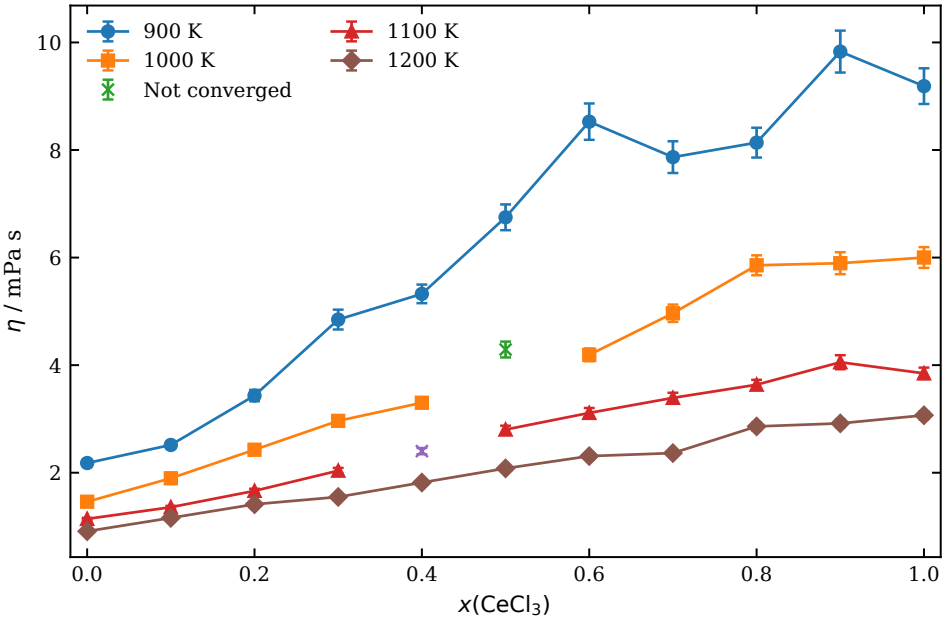

Figure 5.25. Composition dependence of the NaCl – $CeCl_3$ shear viscosity obtained from 5 ns trajectories at 900–1200 K. Error bars denote the reported SporTran uncertainty. Crossed markers identify the two provisional states for which convergence was not demonstrated. Lines connect only reportable values and are guides to the eye.

The combined picture is therefore not one of structural freezing. Nd-rich melts exhibit increasingly recurrent chloride-mediated connectivity over long times while retaining rapid local topological rearrangement. This behaviour is consistent with the broad viscosity increase, but it does not establish a unique causal relation between any individual persistence time and the Green–Kubo coefficient. Detailed window-level diagnostics and the finite-lag limitations are reported in Section A.5.2.

5.6.2 Binary NaCl – $CeCl_3$

Five-Nanosecond Viscosity Trends

The NaCl – $CeCl_3$ production dataset contains all 44 combinations of four temperatures and 11 compositions. Of these, 42 satisfy the adopted reporting protocol. Convergence was not demonstrated for $x(CeCl_3) = 0.50$ at 1000 K and $x(CeCl_3) = 0.40$ at 1100 K; all other states are reportable, including estimates confirmed through additional sensitivity checks.

Viscosity decreases monotonically with temperature at every composition and increases broadly with $CeCl_3$ content (Figure 5.25). At 900 K it rises from 2.180 ± 0.055 mPa s for pure NaCl to 9.188 ± 0.332 mPa s for pure $CeCl_3$; at 1200 K, the corresponding range narrows to 0.911 ± 0.014–3.068 ± 0.076 mPa s. Four neighbouring composition intervals show numerical decreases, but none reaches $|z| \geq 2$. They are therefore treated as unresolved local irregularities rather than established viscosity minima.

The Ce and Nd binaries share the same dominant temperature and composition responses, but their curves are not identical. At 900 K the Ce series lies above the Nd series at every matching composition, whereas the differences narrow and can change sign at higher temperature. This

reinforces the broader conclusion that the two lanthanides are useful comparative model systems but are not dynamically interchangeable merely because they have the same formal charge.

Experimental Validation and U Benchmark

The Ce-containing system was assessed in the same two-level manner. The pure $CeCl_3$ endpoint was compared with the same-system measurements of Potapov and Sato [65], while the matched-composition NaCl – UCl_3 PIM-MD results of Ter Veer et al. [66] test Ce/U simulant behaviour at $x(MCl_3) = 0.37$. As for the Nd/Pu comparison, the present $x = 0.37$ values were interpolated only when both bracketing lanthanide states were reportable.

Table 5.3. Same-system experimental validation and matched-composition U benchmark for the 5 ns NaCl – $CeCl_3$ viscosity. The pure-$CeCl_3$ reference at 1100 K is within the measurement range of Potapov and Sato [65]. The $x = 0.37$ NaCl – UCl_3 values are from Ter Veer et al. [66]. The 1100 K Ce/U comparison is omitted because the required $x(CeCl_3) = 0.40$ state is provisional.

Benchmark	$x(MCl_3)$	T / K	η_{this} / mPa s	η_{ref} / mPa s	δ_η / %
Pure $CeCl_3$, experiment	1.00	1100	3.847 ± 0.107	4.115	-6.5
NaCl – UCl_3, PIM-MD	0.37	900	5.182 ± 0.133	6.364 ± 0.908	-18.6
NaCl – UCl_3, PIM-MD	0.37	1000	3.200 ± 0.072	3.926 ± 1.062	-18.5
NaCl – UCl_3, PIM-MD	0.37	1200	1.737 ± 0.030	1.996 ± 0.549	-13.0

At the pure endpoint, the 1100 K simulation gives 3.847 ± 0.107 mPa s compared with 4.115 mPa s from the experimental correlation, a difference of only -6.5% at a temperature inside the measured range. This provides a direct same-system check of the Ce viscosity scale, while still not constituting validation of the entire binary composition curve.

At $x(MCl_3) = 0.37$, the Ce/U PIM-MD differences are -18.6, -18.5 and -13.0% at 900, 1000 and 1200 K, giving a descriptive MARD of 16.7%. All three differences remain within two combined standard uncertainties of the reported values. A further independent actinide check is provided by the 63:37 mol% NaCl – UCl_3 rolling-ball measurements of Termini et al. [68]. The three measurements clustered average 5.333 mPa s with a sample standard deviation of 0.178 mPa s, compared with the interpolated 900 K Ce value of 5.182 ± 0.133 mPa s, a difference of -2.8%. At the same composition and temperature scale, the Ter Veer et al. [66] U PIM-MD value is approximately 19.3% above the experimental mean. This comparison shows that part of the Ce/U PIM-MD difference also reflects uncertainty in the actinide model benchmark itself. The close experimental agreement at this single state is encouraging evidence for Ce as a U viscosity simulant, but it is not extrapolated to untested compositions.

Temporal Persistence of the Ce-Centred Network

A corresponding 900 K temporal analysis was performed for the Ce-rich range $x(CeCl_3) = 0.60$–1.00 using sequential 0.5 ns windows of the 5 ns trajectories. The continuous Ce–Cl contact persistence remains in a relatively narrow band of approximately 13.6–14.7 ps, while continuous Ce–Ce shared-chloride linkage persistence spans approximately 15.1–17.1 ps. Neither quantity increases monotonically with Ce content.

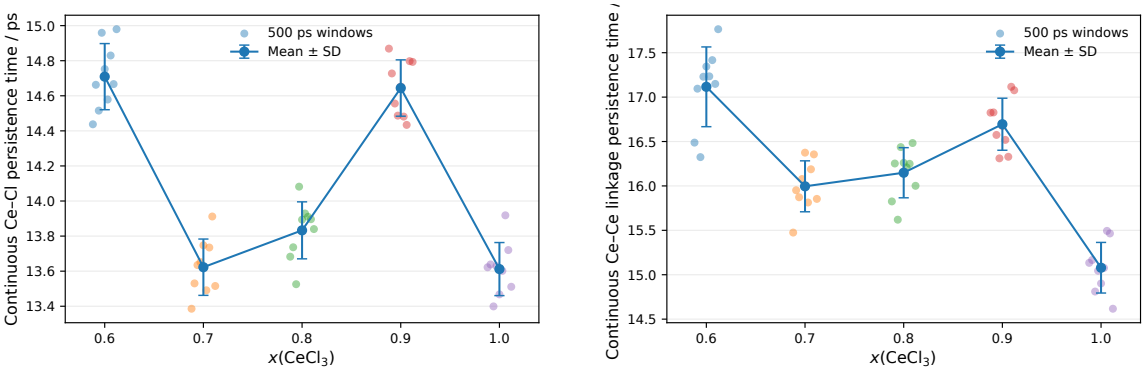

(a) Ce–Cl continuous persistence.

(b) Ce–Ce shared-chloride persistence.

Figure 5.26. Continuous persistence within the Ce-rich NaCl – $CeCl_3$ trajectories at 900 K. Points show the across-window means and error bars the corresponding within-trajectory variability. The windows are sequential portions of one trajectory and are not independent replicas.

This result complements the static connectivity analysis. The Ce-rich network is persistent on picosecond timescales, but the absence of a monotonic increase in these continuous lifetimes shows that the broad rise in viscosity cannot be reduced to a single local bond or linkage lifetime. Instead, the viscosity trend is consistent with the collective development of the connected network reported in Section 5.1, while the temporal data show that the network remains dynamically labile. This is also consistent with the unresolved nature of the small local viscosity decreases.

5.6.3 Equal-Ce/Nd NaCl – $CeCl_3$ – $NdCl_3$ Path

Five-Nanosecond Viscosity Along the Equal-Ce/Nd Path

The ternary calculations follow the equal-Ce/Nd path $x(CeCl_3) = x(NdCl_3)$, with $x(LnCl_3) = x(CeCl_3) + x(NdCl_3) = 0.10$–$0.90$. Nine compositions were simulated at each of the four temperatures. Of the 36 state points, 34 are reportable; convergence was not demonstrated only for $x(LnCl_3) = 0.50$ and 0.80 at 900 K.

Viscosity decreases monotonically with temperature at every composition and generally increases with total lanthanide-chloride content (Figure 5.27). Between $x(LnCl_3) = 0.10$ and 0.90, the viscosity increases by factors of 3.53, 3.12, 2.86 and 2.84 at 900, 1000, 1100 and 1200 K, respectively. The only numerical decrease occurs at 900 K between $x(LnCl_3) = 0.70$ and 0.80, where the change from 9.421 to $8.533\ \mathrm{mPa\,s}$ corresponds to $z = -1.77$ and the $x = 0.80$ endpoint is itself provisional. It is therefore not an established non-monotonic feature.

The completed 1000 K Nd dataset also removes the previous asymmetry in the binary–ternary comparison. Using the arithmetic mean of the matching Ce and Nd binary viscosities only as a descriptive reference, the mean absolute deviation of the ternary values over matching reportable state points is approximately 4.4% at 1000 K, compared with approximately 3.2% at 1100 K and 3.5% at 1200 K. At 900 K the corresponding deviation is larger, approximately 15.1%, including a ternary value 30.3% above the binary mean at $x(LnCl_3) = 0.70$. The low-temperature ternary curve therefore shows the largest departure from this simple binary reference, without implying a thermodynamic ideal-mixing law for viscosity.

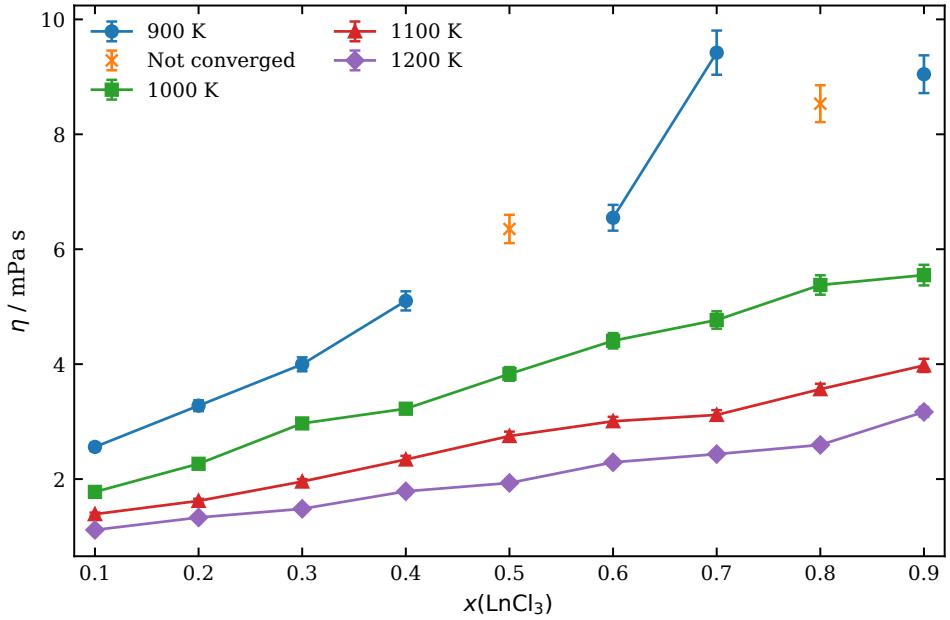

Figure 5.27. Composition dependence of the 5 ns NaCl – $CeCl_3$ – $NdCl_3$ viscosity along the equal-Ce/Nd path at 900–1200 K. Here, $x(\mathrm{LnCl_3}) = x(\mathrm{CeCl_3}) + x(\mathrm{NdCl_3})$ and $x(\mathrm{CeCl_3}) = x(\mathrm{NdCl_3})$. Error bars denote the reported SporTran uncertainty. Crossed markers denote the two provisional 900 K states.

Temporal Persistence of the Ternary Network

The ternary structural hypothesis was tested with the final time-resolved analysis of the 900 and 1000 K trajectories for $x(\mathrm{LnCl_3}) = 0.40$–$0.90$. Each 5 ns trajectory contains 1001 saved frames separated by approximately 5 ps. Temporal stability was assessed using five non-overlapping 1 ns blocks, and the persistence functions were integrated to a maximum lag of 500 ps. Continuous and intermittent Ce–Cl–Ce, Ce–Cl–Nd and Nd–Cl–Nd bridge persistence were evaluated using the accepted first-shell distance definitions. “Continuous” therefore means continuously present at the saved-frame resolution.

Across both temperatures, the three bridge classes vary smoothly with composition. The final block-resolved analysis does not identify a special persistence anomaly at $x(\mathrm{LnCl_3}) = 0.80$, so the unresolved 900 K viscosity decrease is not accompanied by a corresponding temporal-network signature. The mixed Ce–Cl–Nd bridge also remains comparable in persistence to the two like-cation bridge classes rather than showing exceptional stabilisation. The ternary liquid is therefore best described as one dynamically connected mixed network, with no evidence for a uniquely long-lived cooperative Ce–Nd bridge.

The five blocks belong to the same trajectory and are not independent replicas. Their variation quantifies within-trajectory temporal stability, and the finite-window integrals are treated as integrated persistence times rather than complete infinite-time lifetimes. These results provide structural support for the broad viscosity trend without assigning the macroscopic shear response to one bridge lifetime. Supporting protocol details are given in Section A.5.4.

5.6.4 Cross-System Synthesis

The final 5 ns campaign provides broad and internally consistent transport coverage across all three melts. Of 124 viscosity state points, 116 satisfy the adopted reporting protocol: 40 of 44 for NaCl – $NdCl_3$, 42 of 44 for NaCl – $CeCl_3$, and 34 of 36 along the ternary path. Across all three systems, viscosity decreases with temperature and increases broadly as trivalent chloride replaces NaCl; the comparatively small number of provisional points is retained explicitly rather than obscured by interpolation.

The structural and temporal analyses provide a consistent but qualified microscopic interpretation. Increasing trivalent-chloride content promotes shared-chloride connectivity and network formation, while the time-resolved analyses show that these networks remain dynamic. In the Nd-rich binary, intermittent recurrence strengthens markedly even as topology switching becomes faster. In the Ce-rich binary, continuous local persistence stays within a relatively narrow range rather than increasing monotonically. In the ternary, mixed Ce–Cl–Nd bridges have persistence comparable to the two like-cation bridges and show no special anomaly at the provisional 900 K viscosity dip. Together these observations support a network-relaxation interpretation of the broad viscosity trends without implying that a single RDF feature, coordination number or linkage lifetime uniquely determines viscosity.

The external comparisons add a property-specific validation layer to this numerical result. The reportable pure-$CeCl_3$ and pure-$NdCl_3$ reference comparisons differ from the corresponding experimental correlations by about 6% in magnitude, while the matched $x(\mathrm{MCl_3}) = 0.37$ actinide comparison is closer for Ce/U than for Nd/Pu over the retained temperatures: the descriptive MARD is 16.7% for Ce/U and 25.8% for Nd/Pu. The additional published 63:37 mol% NaCl – UCl_3 measurement near 901 K is within 2.8% of the interpolated 900 K Ce result. These comparisons do not establish universal surrogacy, but they show that the lanthanide systems reproduce the viscosity scale and thermal response of relevant actinide salts to a useful, property-dependent degree.

Four of the eight provisional viscosity states occur at 900 K. This clustering is consistent with the phase-state context rather than being attributable only to the spectral estimator. The NaCl–rare-earth phase-diagram comparisons presented by Alders et al. [17] show that at 900 K the equilibrium single-liquid field spans only part of the binary composition range. Some low-temperature states, particularly on the trichloride-rich side, therefore have a reduced thermal margin to the liquidus or represent metastable-liquid extensions and may relax more slowly. Proximity to the liquidus cannot explain every provisional point, however, and the viscosity analysis itself does not constitute evidence of crystallisation. It is treated as a plausible physical contributor to the greater low-temperature convergence sensitivity.

The completed four-temperature Nd dataset also makes the viscosity comparison substantially more balanced than in the earlier draft. Remaining limitations are now local rather than dataset-wide: eight of the 124 state points remain provisional, the actinide viscosity benchmark is restricted to one mixture composition, the dedicated temporal analyses cover selected temperature and composition ranges, and the within-trajectory windows or blocks are not independent replicas. These qualifications constrain the precision of the mechanistic interpretation but leave the dominant temperature, composition and cross-system trends well supported.

6

Conclusions and Recommendations

6.1 Conclusions

This thesis establishes an internally consistent atomistic description of molten NaCl – $CeCl_3$, NaCl – $NdCl_3$ and the equal-Ce/Nd path through NaCl – $CeCl_3$ – $NdCl_3$ using Polarizable Ion Model molecular dynamics. Its principal contribution is the systematic comparison of thermophysical, thermodynamic, structural and transport responses over a common 900–1200 K grid, supported by explicit convergence tests and a property-specific assessment of lanthanide–actinide analogy. The resulting dataset resolves clear composition–structure–property trends while also identifying where model or reference limitations remain. The research questions posed in Section 1.4 are answered below.

RQ1: Composition- and temperature-dependent property behaviour

Both binary melts show systematic and physically consistent bulk-property trends. Density increases as $CeCl_3$ or $NdCl_3$ replaces NaCl and decreases with temperature, while molar volume increases with trichloride content and thermal expansion. Heat capacity also increases smoothly with trichloride fraction, from approximately 72.4 $\mathrm{J\,mol^{-1}\,K^{-1}}$ for NaCl to approximately 141 $\mathrm{J\,mol^{-1}\,K^{-1}}$ for the pure rare-earth trichlorides. Viscosity decreases with temperature and increases broadly with trichloride content. The structural-coherence thermal-conductivity model instead predicts a pronounced composition minimum in the two binaries, followed by recovery towards the pure trichlorides.

The binaries are not ideal mixtures. Excess molar volume changes sign between the NaCl-rich and trichloride-rich regions, excess heat capacity changes from slightly negative to positive values, and direct PIM-MD mixing enthalpies are negative throughout the investigated interior composition range. At 1100 K, the direct mixing-enthalpy minima occur near a trichloride fraction of 0.4 and are approximately $-11.24\ \mathrm{kJ\,mol^{-1}}$ for NaCl – $CeCl_3$ and $-11.71\ \mathrm{kJ\,mol^{-1}}$ for NaCl – $NdCl_3$. These

excess quantities provide clearer evidence of non-ideality than the smooth total density, molar-volume and heat-capacity curves.

RQ2: Evolution of microscopic liquid structure

The simulations show a hierarchical structural response to increasing trichloride content. Ce- and Nd-centred chloride first shells remain distinct, consistent with their different ionic sizes and the lanthanide contraction. Their coordination-number distributions are broad rather than fixed at one integer value. As the rare-earth concentration increases, chloride sharing becomes more common, isolated or finite coordination environments merge, and the rare-earth substructure develops into an extensively connected network. The mean first-shell coordination number approaches a plateau before network connectivity stops evolving, demonstrating that local coordination and intermediate-range topology are related but non-equivalent descriptors.

Along the equal-Ce/Nd ternary path, separate Ce–Cl and Nd–Cl first shells are retained while Ce–Ce, Ce–Nd and Nd–Nd connections become part of one mixed chloride-mediated network. The ternary therefore does not behave as two spatially independent binary subnetworks. At representative 1100 K states, the Ce–Ce:Ce–Nd:Nd–Nd linkage fractions remain within 1.40 percentage points of the 25:50:25 random-pair expectation, providing no evidence for a strong preferential Ce–Nd association. Mixed Ce–Cl–Nd bridges are a normal constituent of the connected structure. In the final block-resolved temporal analysis at 900 and 1000 K, their persistence remains comparable to the like-cation bridges and no composition-specific anomaly is identified at $x(\mathrm{LnCl_3}) = 0.80$.

RQ3: Microscopic interpretation of macroscopic trends

The strongest structure–property relation is the composition-driven change from relatively isolated trivalent coordination environments in NaCl-rich melts to a connected chloride-sharing network at higher trichloride content. This structural crossover occurs in the same broad composition region as several non-linear macroscopic responses, including the mixing-enthalpy minimum and the onset of strong viscosity growth. The correspondence supports a common physical interpretation based on chloride redistribution, increasing rare-earth connectivity and more collective structural rearrangement. It does not justify assigning a macroscopic property to one RDF peak, one average coordination number or one linkage class.

The time-resolved viscosity analyses make this distinction more precise. In Nd-rich NaCl – $NdCl_3$ at 900 K, intermittent Nd–Cl persistence increases from 54.08 to 71.29 ps between $x(\mathrm{NdCl_3}) = 0.60$ and 1.00, while intermittent Nd–Nd shared-chloride persistence increases from 79.19 to 115.49 ps. At the same time, the topology-switching rate increases from 4.255 to $6.079\ \mathrm{ps^{-1}\,Nd^{-1}}$. The Nd-centred network therefore becomes more recurrent on longer timescales while remaining locally labile. In the Ce-rich binary, continuous Ce–Cl and Ce–Ce persistence remains within relatively narrow picosecond ranges rather than increasing monotonically with composition, again indicating a connected but dynamically rearranging liquid. The ternary analysis provides a complementary result: the mixed Ce–Cl–Nd bridge is not exceptionally long lived relative to the two like-cation bridge classes. Together these observations support a network-relaxation interpretation of the broad viscosity trends without claiming that one persistence time uniquely determines the Green–Kubo coefficient.

For thermal transport, the structural-coherence decomposition attributes the binary minima mainly to a loss of coherence length when trivalent cations are first introduced into the NaCl-rich liquid, followed by recovery as a single-trichloride-like environment develops. The equal-Ce/Nd ternary path retains shorter coherence lengths and lacks the same high-composition recovery. This mechanism is physically consistent with the structural data, but remains a model interpretation because the microscopic heat-current correlation was not calculated.

RQ4: Agreement with reference evidence and model limitations

PIM-MD performs best for several equilibrium and structural trends. The binary density and molar-volume calculations follow the available same-system reference descriptions closely, while the heat-capacity curves are very close to the supplied actinide PIM-MD benchmarks: the root-mean-square differences are approximately $0.67\ \mathrm{J\,mol^{-1}\,K^{-1}}$ for the Ce/U comparison and $0.98\ \mathrm{J\,mol^{-1}\,K^{-1}}$ for Nd/Pu. The structural simulations also reproduce the expected Ce–Cl/Nd–Cl distinction and the composition-driven development of shared-chloride networks.

The strongest systematic model discrepancy occurs in mixing enthalpy. The direct simulations reproduce the exothermic sign and broad intermediate- composition minimum observed calorimetrically but predict substantially more negative values. The 1100 K NaCl – $NdCl_3$ minimum of approximately $-11.71\ \mathrm{kJ\,mol^{-1}}$, for example, is considerably more exothermic than the experimental broad minimum reported near $-5.7\ \mathrm{kJ\,mol^{-1}}$. The independently parameterised PMF-informed MIVM preserves the sign and general curvature but does not eliminate the magnitude discrepancy. By contrast, the binary benchmark-calibrated MIVM reproduces the calorimetric curves more closely because its directional interaction parameters are fitted to those data; this improvement is therefore semi-empirical rather than an independent validation. The defensible conclusion is that the atomistic model captures the form of non-ideal mixing more reliably than its absolute energetic strength, while the calibrated MIVM quantifies the effective correction needed to recover experiment.

The structural-coherence thermal-conductivity calculation has an even clearer boundary of validity. It reproduces useful relative trends and gives Ce/U and Nd/Pu comparisons of similar order, but direct comparison with the NaCl – $CeCl_3$ measurements of Bobrova and Dokytovich [89] shows underprediction of approximately 60–67% at representative intermediate compositions near 1173 K. The binary minima are dominated in the model decomposition by the loss of structural coherence length, while the sound-speed term supplies a secondary thermodynamic modulation. These conductivities must consequently be treated as model-derived trend estimates rather than validated absolute predictions.

The viscosity campaign provides both a strong numerical result and targeted external validation. The final analysis uses exact 5 ns production trajectories throughout and combines trajectory-length, shifted-window and spectral- sensitivity tests before a state is accepted for reporting. This protocol yields 40 reportable states out of 44 for NaCl – $NdCl_3$, 42 of 44 for NaCl – $CeCl_3$, and 34 of 36 along the ternary path, so 116 of 124 state points are supported for quantitative reporting. At the pure endpoints, the reportable 1100 K $CeCl_3$ viscosity differs from the experimental correlation of Potapov and Sato [65] by -6.5%, while the reportable 1000 K $NdCl_3$ value is -5.8% below a short 25 K extrapolation of the corresponding correlation. In addition, the interpolated 900 K

NaCl – $CeCl_3$ viscosity at $x(CeCl_3) = 0.37$ is only 2.8% below the published 63:37 mol% NaCl – UCl_3 rolling-ball measurement near 901 K reported by Termini et al. [68]. These checks strengthen the absolute transport scale while leaving the broad-composition binary and ternary curves primarily as converged model predictions.

RQ5: Property-specific lanthanide–actinide simulant behaviour

The present results support a firmer but explicitly property-specific answer: lanthanide trichlorides can serve as experimentally accessible simulants for actinide trichlorides, but they are not universally interchangeable substitutes. Nd provides a particularly close representation of Pu at the level of average metal–chloride coordination: the composition-dependent Nd and Pu curves are nearly coincident in the supplied PIM-MD comparison, although the Nd-rich shared-chloride network remains somewhat more corner dominated. Ce shows a larger offset from U in average coordination number but a close endmember balance among corner-, edge- and face/higher-order sharing. Both analogue pairs also reproduce similar broad excess-volume and heat-capacity trends.

Viscosity reinforces the property dependence rather than reproducing the same ranking as local structure. At the matched composition $x(MCl_3) = 0.37$, the retained Ce/U comparisons with Ter Veer et al. [66] have a descriptive MARD of 16.7%, compared with 25.8% for Nd/Pu. The published 63:37 mol% NaCl – UCl_3 rolling-ball result of Termini et al. [68] is also within 2.8% of the interpolated 900 K Ce value. Thus Ce is the closer viscosity analogue to U for this particular benchmark composition, even though Nd is the closer Pu analogue for average first-shell coordination. The structural-coherence Ce/U and Nd/Pu thermal-conductivity comparisons show similar temperature responses within the common modelling framework, but the failure to reproduce available Ce experiments prevents those analogue comparisons from being promoted to absolute validation. Surrogate selection must therefore be made for the target property, composition and temperature, and for structure even the length scale of interest.

RQ6: Behaviour of the equal-Ce/Nd ternary path

The ternary path is neither a completely independent new liquid regime nor a trivial ideal interpolation of the two binaries. Its total density, molar volume and heat capacity evolve smoothly between the binary limits, and its direct mixing enthalpy lies between the corresponding Ce- and Nd-containing trends. No large additional energetic stabilisation attributable uniquely to the simultaneous presence of Ce and Nd is resolved along the investigated path.

More sensitive quantities reveal additional ternary effects. The direct excess molar volume differs more strongly from the binary-derived Redlich–Kister–Muggianu representation than the total molar volume does, and the structural-coherence thermal conductivity remains flatter and lower than the full binary curves. Structurally, the melt forms one mixed Ce/Nd network. The species-resolved linkage fractions are approximately consistent with stochastic Ce/Nd pairing, and the final block-resolved temporal analysis finds the Ce–Cl–Nd bridge persistence comparable to the two like-cation bridge classes rather than exceptionally stabilised. The available evidence therefore does not support a special cooperative mixed-cation linkage as the origin of the ternary response. The scientifically defensible result is that mixed Ce and Nd environments modify sensitive

excess and transport quantities while remaining broadly compatible with a continuously evolving, dynamically labile shared-chloride network.

Taken together, the results answer the overarching research question positively but selectively: Ce- and Nd-based chloride melts are defensible non-radioactive simulant systems for targeted actinide-relevant measurements and model development, provided that the surrogate is chosen for the property of interest rather than assumed to be universally equivalent. The strongest support is obtained for volumetric behaviour, heat capacity, local/network structure and the converged viscosity trends, for which the new experimental and matched-composition actinide comparisons also support the transport scale. The energetic and thermal-conductivity discrepancies identify the properties for which force-field or post-processing refinement is still required. This property-resolved conclusion provides a more useful basis for future molten- salt modelling than unqualified one-to-one replacement of an actinide by a lanthanide.

6.2 Limitations

The principal limitations define the transferability of these conclusions. First, the 2000-ion cell size was selected as a physics–cost compromise and was not subjected to a separate finite-size scaling study. This leaves a finite-size contribution to the uncertainty of long-wavelength and transport properties, although the consistent cell size across systems supports relative comparisons.

Second, the PIM is a fixed-valence classical model. It includes induced polarisation but not explicit charge transfer, redox chemistry or electronic state changes. The Ce–Nd cross interaction in the ternary is additionally an interpolated modelling choice rather than a parameter fitted to direct ternary data. Smooth behaviour and binary-limit consistency support its use along the investigated path, but they do not constitute an independent validation of the cross interaction.

Third, several 900 K rare-earth-rich simulations correspond to homogeneous liquid trajectories with a small or negative equilibrium margin to the liquidus. Phase-diagram comparisons presented by Alders et al. [17] show that the equilibrium single-liquid region at 900 K spans only part of the relevant binary composition range. These states therefore provide near-liquidus or metastable-liquid property extensions and should not be interpreted as phase-stability predictions. The concentration of several provisional viscosity points at 900 K is consistent with slower relaxation near this phase boundary, but it is not evidence of crystallisation and does not explain every convergence-sensitive state. The thesis does not construct a new phase diagram or perform a CALPHAD assessment.

Fourth, experimental validation is property dependent. The binary volumetric and mixing-enthalpy evidence is substantially stronger than broad-composition viscosity evidence. The viscosity validation added here consists of pure $CeCl_3$/$NdCl_3$ endpoint measurements and a published 63:37 mol% NaCl – UCl_3 actinide measurement, while the wider Ce/U and Nd/Pu PIM-MD comparison is restricted to $x(MCl_3) = 0.37$. No direct thermophysical or transport dataset was located for the target ternary path. Consequently, the ternary results remain predictions constrained by binary evidence and internal consistency rather than directly validated measurements.

Fifth, thermal conductivity was obtained from the structural-coherence model because a validated microscopic heat-current series was not available. The large discrepancy with the NaCl – $CeCl_3$ measurements shows that this post-processing route introduces model uncertainty larger than

its numerical window sensitivity. The conductivity trends remain useful for relative structure–transport comparison, but their absolute values should not be used as experimentally validated design data.

Sixth, the viscosity coverage is broad but not complete in a statistical sense. Eight of the 124 final 5 ns state points remain provisional because convergence was not demonstrated: four in $NaCl-NdCl_3$, two in $NaCl-CeCl_3$ and two along the ternary path. The dedicated temporal analyses also cover selected composition and temperature ranges rather than every state point. Their windows or blocks are portions of single trajectories and are therefore within-trajectory stability diagnostics rather than independent replicas. In the Nd temporal dataset, the associated coordination audit additionally shows a systematic 0.15–0.19 offset from the accepted RDF reference. These qualifications restrict the precision of the mechanistic interpretation but do not alter the dominant, converged temperature and composition trends. Although trajectory-length and spectral-estimator sensitivities were assessed extensively, the 5 fs stress-sampling interval was not independently tested against finer output intervals. A future 1–2–5 fs comparison would provide a direct sampling-frequency sensitivity test.

Finally, Redlich–Kister, Muggianu, MIVM and structural-coherence quantities are post-processing models rather than additional MD observations. Their interpolated extrema, extrapolated regions and fitted parameters inherit model form uncertainty in addition to MD sampling uncertainty. The thesis therefore treats direct state-point simulations as the primary evidence and uses these models to organise, interpolate or interpret that evidence within their tested domains.

6.3 Recommendations

The highest-priority continuation is now independent replication of a small number of representative viscosity states, with emphasis on compositions that retain the greatest window sensitivity. Such replicas would provide a direct estimate of between-run variability and test whether the present within-trajectory convergence diagnostics are conservative. A focused stress-output sensitivity test at 1, 2 and 5 fs intervals would complement that replication without requiring a new broad state-point campaign.

A second priority is targeted validation of the most consequential model uncertainties. Direct measurements of viscosity for finite-composition $NaCl-CeCl_3$ and $NaCl-NdCl_3$, and thermophysical measurements along at least part of the $NaCl-CeCl_3-NdCl_3$ path, would provide much stronger tests than further comparison with related systems. For mixing enthalpy, additional high-quality calorimetry would help distinguish force-field over-stabilisation from reference-state and model-reduction effects.

For thermal conductivity, a dedicated microscopic heat-current implementation for the polarizable multicomponent potential should be formulated and validated before direct Green–Kubo calculations are attempted. Comparison of that route with the structural-coherence estimates and with experiment would separate deficiencies of the PIM from deficiencies of the coherence model.

The ternary model should also be extended beyond the equal-Ce/Nd line. A limited but strategically selected two-dimensional composition design would be more informative than simply increasing the number of points along the same pseudo-binary path. This extension should include

the NaCl-free $CeCl_3$ – $NdCl_3$ edge, particularly the 50:50 Ce/Nd composition, because that state is not contained in the present dataset and cannot be inferred as a new MD result from the equal-Ce/Nd path. Compositions near the onset of network polymerisation, the strongest excess-volume deviations and the low-temperature transport crossover should receive priority. Species-resolved temporal persistence at multiple temperatures would then test whether the recurrent, labile network behaviour identified at 900 K is general or restricted to the Nd-rich low-temperature regime.

Finally, the Ce–Nd cross interaction should be tested directly against first-principles forces or energies for mixed Ce/Nd chloride configurations. Such a calculation would address a genuine model-transferability uncertainty without expanding the thesis into unrelated methodology. Together with a small finite-size study for representative transport states, this would provide the most direct route from the present internally consistent dataset towards a more predictive model of multicomponent actinide-relevant chloride melts.

References

[1] L. Clarke, Y.-M. Wei, A. De La Vega Navarro, A. Garg, A. N. Hahmann, S. Khennas, I. M. L. Azevedo, A. L"oschel, A. K. Singh, L. Steg, G. Strbac and K. Wada. 'Energy Systems'. In: *Climate Change 2022: Mitigation of Climate Change. Contribution of Working Group III to the Sixth Assessment Report of the Intergovernmental Panel on Climate Change*. Ed. by P. R. Shukla, J. Skea, R. Slade, A. Al Khourdajie, R. van Diemen, D. McCollum, M. Pathak, S. Some, P. Vyas, R. Fradera, M. Belkacemi, A. Hasija, G. Lisboa, S. Luz and J. Malley. Cambridge, UK and New York, NY, USA: Cambridge University Press, 2022. DOI: 10.1017/9781009157926.008.

[2] International Energy Agency. *Global Energy Review 2025*. Report. Paris: International Energy Agency, 24th Mar. 2025. URL: https://www.iea.org/reports/global-energy-review-2025 (visited on 07/08/2026).

[3] International Energy Agency. *The Path to a New Era for Nuclear Energy*. International Energy Agency. 2025. URL: https://www.iea.org/reports/the-path-to-a-new-era-for-nuclear-energy (visited on 18/07/2026).

[4] Generation IV International Forum. *Molten Salt Reactors (MSR)*. Undated webpage; year assigned from the accessed version. Generation IV International Forum. 2026. URL: https://www.gen-4.org/generation-iv-criteria-and-technologies/molten-salt-reactors-msr (visited on 18/07/2026).

[5] J. C. Gehin and J. J. Powers. 'Liquid Fuel Molten Salt Reactors for Thorium Utilization'. In: *Nuclear Technology* 194.2 (2016), pp. 152–161. DOI: 10.13182/NT15-124.

[6] International Atomic Energy Agency. *Status of Molten Salt Reactor Technology*. Tech. rep. Technical Reports Series No. 489. Vienna: International Atomic Energy Agency, 2021. URL: https://www.iaea.org/publications/14998/status-of-molten-salt-reactor-technology (visited on 18/07/2026).

[7] Oak Ridge National Laboratory. *History: Molten Salt Reactor*. Undated webpage; year assigned from the accessed version. Oak Ridge National Laboratory. 2026. URL: https://www.ornl.gov/molten-salt-reactor/history (visited on 18/07/2026).

[8] J. Smith et al. *An Assessment of a 2500 MWe Molten Chloride Salt Fast Reactor*. Tech. rep. AEEW-R 956. United Kingdom Atomic Energy Authority, Atomic Energy Establishment Winfrith, 1974. URL: https://moltensalt.org/references/static/downloads/pdf/AEEW-R956.pdf (visited on 18/07/2026).

[9] M. Taube. *Fast Reactors Using Molten Chloride Salts as Fuel*. Tech. rep. EIR-332. Swiss Federal Institute for Reactor Research, 1978. URL: https://moltensalt.org/references/static/downloads/pdf/EIR-332.pdf (visited on 18/07/2026).

[10] D. E. Holcomb, G. F. Flanagan, B. W. Patton, J. C. Gehin, R. L. Howard and T. J. Harrison. *Fast Spectrum Molten Salt Reactor Options*. Tech. rep. ORNL/TM-2011/105. Oak Ridge National Laboratory, 2011. DOI: 10.2172/1018987.

[11] U.S. Department of Energy, Office of Nuclear Energy. *Idaho National Lab Creates First Batch of Fuel for World's First Fast Spectrum Molten Salt Reactor Experiment*. U.S. Department of Energy. 3rd Dec. 2025. URL: https://www.energy.gov/ne/articles/idaho-national-lab-creates-first-batch-fuel-worlds-first-fast-spectrum-molten-salt (visited on 18/07/2026).

[12] U.S. Department of Energy, Office of Nuclear Energy. *DOE Releases Final Environmental Assessment for Molten Chloride Reactor Experiment*. U.S. Department of Energy. 1st Aug. 2023. URL: https://www.energy.gov/ne/articles/doe-releases-final-environmental-assessment-molten-chloride-reactor-experiment (visited on 18/07/2026).

[13] M. A. Rose and D. Ezell. *Molten Salt Reactor Fuel Cycle Chemistry Workshop Report*. Tech. rep. Argonne National Laboratory, 2023. DOI: 10.2172/2311167.

[14] H. Matsuura, S. Watanabe, T. Sakamoto, T. Kanuma, K. Naoi, M. Hatcho, N. Kitamura, H. Akatsuka, A. K. Adya, T. Honma, T. Uruga and N. Umesaki. 'Short-Range Structure of Molten CeCl3 and NdCl3 Determined by XAFS'. In: *Journal of Alloys and Compounds* 408 (2006). Published in the combined volumes 408–412, pp. 80–83. DOI: 10.1016/j.jallcom.2005.04.157.

[15] K. Goloviznina, M.-C. Notarangelo, J. Tranchida, E. Bourasseau and M. Salanne. 'DFT-Based Polarizable Ion Models for Molten Rare-Earth Chlorides: From Lanthanum to Europium'. In: *The Journal of Physical Chemistry B* 129.3 (2025), pp. 1016–1025. DOI: 10.1021/acs.jpcb.4c07931.

[16] K. Goloviznina and M. Salanne. 'What Is a Good Simulant for Plutonium(III) in Molten Chloride Salts?' In: *The Journal of Physical Chemistry B* 129.30 (2025), pp. 7826–7830. DOI: 10.1021/acs.jpcb.5c03702.

[17] D. C. Alders, A. Sacristán-Civera, M. Wolff, E. Capelli, E. L. Bright, C. Hennig, R. J. M. Konings and A. L. Smith. 'Simulant Chemistry for Uranium and Plutonium Molten Fuel Salts: Crystallographic Investigation and Thermodynamic Modelling Assessment of the NaCl–RECl3 and NaCl–MgCl2–RECl3 (RE = Ce, Nd) Systems'. In: *Dalton Transactions* 54.44 (2025), pp. 16475–16491. DOI: 10.1039/D5DT01486G.

[18] J. Mochinaga and K. Igarashi. 'Densities and Molar Volumes of Molten Binary PrCl3–KCl, PrCl3–NaCl, PrCl3–CaCl2, NdCl3–KCl, NdCl3–NaCl, NdCl3–CaCl2 Systems'. In: *Bulletin of the Chemical Society of Japan* 48.2 (1975), pp. 713–714. DOI: 10.1246/bcsj.48.713.

[19] T. Sato, Y. Okamoto and T. Ogawa. 'Density Measurement of Molten NdCl3–NaCl and NdCl3–KCl Systems by Gamma Ray Attenuation'. In: *Journal of Nuclear Science and Technology* 39.sup3 (2002), pp. 635–637. DOI: 10.1080/00223131.2002.10875548.

[20] M. Gaune-Escard, A. Bogacz, L. Rycerz and W. Szczepaniak. 'Calorimetric Investigation of NdCl3–MCl Liquid Mixtures, Where M = Na, K, Rb, Cs'. In: *Thermochimica Acta* 236 (1994), pp. 67–80. DOI: 10.1016/0040-6031(94)80256-4.

[21] F. Dienstbach and R. Blachnik. 'Mischungsenthalpien von geschmolzenen Alkalihalogenid-Lanthanoidenhalogenidsystemen'. In: *Zeitschrift für anorganische und allgemeine Chemie* 412.2 (1975), pp. 97–109. DOI: 10.1002/zaac.19754120202.

[22] K. Igarashi, M. Kosaka, Y. Iwadate, T. Hattori and J. Mochinaga. 'Phase Diagrams of LiCl–NdCl3, NaCl–NdCl3, and CaCl2–NdCl3 Systems'. In: *Denki Kagaku Oyobi Kogyo Butsuri Kagaku* 58.5 (1990), pp. 469–470. DOI: 10.5796/kogyobutsurikagaku.58.469.

[23] A. M. Potapov, L. Rycerz and M. Gaune-Escard. 'Electrical Conductivity of Melts Containing Rare-Earth Halides. I. MCl–NdCl3 (M = Li, Na, K, Rb, Cs)'. In: *Zeitschrift für Naturforschung A* 62.7–8 (2007), pp. 431–440. DOI: 10.1515/zna-2007-7-813.

[24] M. Zabłocka-Malicka and W. Szczepaniak. 'Internal Mobility of Ln3+ Ions in the KCl–LnCl3 and NaCl–NdCl3 Systems. A Single Coefficient Correlation Model'. In: *Journal of Molecular Liquids* 137.1–3 (2008), pp. 36–42. DOI: 10.1016/j.molliq.2007.03.004.

[25] V. N. Dokutovich, E. S. Filatov, V. A. Khokhlov and V. I. Minchenko. 'Thermal Conductivity of NdCl3–MCl (M = Na, K, Cs) Melts'. In: *Russian Metallurgy (Metally)* (2011), pp. 114–117. DOI: 10.1134/S0036029511020054.

[26] G. N. Papatheodorou and O. J. Kleppa. 'Thermodynamic Studies of Binary Charge-Unsymmetrical Fused-Salt Systems: Cerium(III) Chloride–Alkali Chloride Mixtures'. In: *The Journal of Physical Chemistry* 78.2 (1974), pp. 178–181. DOI: 10.1021/j100595a018.

[27] H. J. Seifert, J. Sandrock and G. Thiel. 'Thermochemical Studies on the Systems ACl/CeCl3 (A = Na–Cs)'. In: *Journal of Thermal Analysis* 31 (1986), pp. 1309–1318. DOI: 10.1007/BF01914643.

[28] H. Seifert. 'Ternary Chlorides of the Trivalent Early Lanthanides: Phase Diagrams, Crystal Structures and Thermodynamic Properties'. In: *Journal of Thermal Analysis and Calorimetry* 67.3 (2002), pp. 789–826. DOI: 10.1023/A:1014341829611.

[29] K. O. Bobrova and V. N. Dokutovich. 'Thermal Conductivity of Molten Mixtures of the CeCl3–MCl Systems (M = Li, Na, K, Cs)'. In: *Rasplavy* 3 (2023), pp. 287–297. DOI: 10.31857/S0235010623030027.

[30] M. Salanne and P. A. Madden. 'Polarization effects in ionic solids and melts'. In: *Molecular Physics* 109.19 (2011), pp. 2299–2315. DOI: 10.1080/00268976.2011.617523.

[31] Y. Iwadate. 'Structures and Properties of Rare-Earth Molten Salts'. In: *Handbook on the Physics and Chemistry of Rare Earths*. Ed. by J.-C. G. Bünzli and V. K. Pecharsky. Vol. 44. Elsevier, 2014. Chap. 260, pp. 87–168. DOI: 10.1016/B978-0-444-62711-7.00260-7.

[32] E. S. Sooby, A. T. Nelson, J. T. White and P. M. McIntyre. 'Measurements of the Liquidus Surface and Solidus Transitions of the NaCl–UCl3 and NaCl–UCl3–CeCl3 Phase Diagrams'. In: *Journal of Nuclear Materials* 466 (2015), pp. 280–285. DOI: 10.1016/j.jnucmat.2015.07.050.

[33] D. Corradini, P. A. Madden and M. Salanne. 'Coordination Numbers and Physical Properties in Molten Salts and Their Mixtures'. In: *Faraday Discussions* 190 (2016), pp. 471–486. DOI: 10.1039/C5FD00223K.

[34] M. S. Emerson, S. Sharma, S. Roy, V. S. Bryantsev, A. S. Ivanov, R. Gakhar, M. E. Woods, L. C. Gallington, S. Dai, D. S. Maltsev and C. J. Margulis. 'Complete Description of the LaCl3–NaCl Melt Structure and the Concept of a Spacer Salt That Causes Structural Heterogeneity'. In: *Journal of the American Chemical Society* 144.47 (2022), pp. 21751–21762. DOI: 10.1021/jacs.2c09987.

[35] P. A. Madden and M. Wilson. '"Covalent" Effects in "Ionic" Systems'. In: *Chemical Society Reviews* 25 (1996), pp. 339–350. DOI: 10.1039/CS9962500339.

[36] International Union of Pure and Applied Chemistry. *Polarizability*. Compendium of Chemical Terminology (the Gold Book), 5th ed. 2025. DOI: 10.1351/goldbook.P04711. URL: https://goldbook.iupac.org/terms/view/P04711 (visited on 07/08/2026).

[37] R. D. Shannon. 'Revised Effective Ionic Radii and Systematic Studies of Interatomic Distances in Halides and Chalcogenides'. In: *Acta Crystallographica Section A* 32.5 (1976), pp. 751–767. DOI: 10.1107/S0567739476001551.

[38] J.-P. Hansen and I. R. McDonald. *Theory of Simple Liquids: With Applications to Soft Matter*. 4th ed. Oxford: Academic Press, 2013.

[39] International Union of Pure and Applied Chemistry. *Heat Capacity*. Compendium of Chemical Terminology (the Gold Book), 5th ed. 2025. DOI: 10.1351/goldbook.H02753.

[40] International Union of Pure and Applied Chemistry. *Enthalpy*. Compendium of Chemical Terminology (the Gold Book), 5th ed. 2025. DOI: 10.1351/goldbook.E02141.

[41] F. Hutchinson, A. J. Rowley, M. K. Walters, M. Wilson, P. A. Madden, J. C. Wasse and P. S. Salmon. 'Structure of Molten MCl3 Systems from a Polarizable Ion Simulation Model'. In: *The Journal of Chemical Physics* 111.5 (1999), pp. 2028–2037. DOI: 10.1063/1.479471.

[42] J. C. Wasse and P. S. Salmon. 'Structure of Molten Trivalent Metal Chlorides Studied by Using Neutron Diffraction: The Systems TbCl3, YCl3, HoCl3 and ErCl3'. In: *Journal of Physics: Condensed Matter* 11.47 (1999), pp. 9293–9302. DOI: 10.1088/0953-8984/11/47/313.

[43] N. Galamba, C. A. N. de Castro and J. F. Ely. 'Molecular Dynamics Simulation of the Shear Viscosity of Molten Alkali Halides'. In: *The Journal of Physical Chemistry B* 108.11 (2004), pp. 3658–3662. DOI: 10.1021/jp036234x.

[44] N. Galamba, C. A. N. de Castro and J. F. Ely. 'Thermal Conductivity of Molten Alkali Halides from Equilibrium Molecular Dynamics Simulations'. In: *The Journal of Chemical Physics* 120.18 (2004), pp. 8676–8682. DOI: 10.1063/1.1691735.

[45] J. Numbers, I. Walker, T. Hamm, N. Termini, A. Birri and T. Munro. 'Structural Coherence Model for Predicting Molten Salt Thermal Conductivity Informed by the Pair Distribution Function'. In: *Journal of Molecular Liquids* 452 (2026), p. 129502. DOI: 10.1016/j.molliq.2026.129502.

[46] G. J. Janz. *Thermodynamic and Transport Properties for Molten Salts: Correlation Equations for Critically Evaluated Density, Surface Tension, Electrical Conductance, and Viscosity Data*. Vol. 17. Journal of Physical and Chemical Reference Data Supplement 2. Washington, DC: American Chemical Society and American Institute of Physics for the National Bureau of Standards, 1988. 309 pp.

[47] F. N. Fritsch and R. E. Carlson. 'Monotone Piecewise Cubic Interpolation'. In: *SIAM Journal on Numerical Analysis* 17.2 (1980), pp. 238–246. DOI: 10.1137/0717021.

[48] M. P. Allen and D. J. Tildesley. *Computer Simulation of Liquids*. 2nd ed. Oxford University Press, 2017. DOI: 10.1093/oso/9780198803195.001.0001.

[49] N. Michaud-Agrawal, E. J. Denning, T. B. Woolf and O. Beckstein. 'MDAnalysis: A Toolkit for the Analysis of Molecular Dynamics Simulations'. In: *Journal of Computational Chemistry* 32.10 (2011), pp. 2319–2327. DOI: 10.1002/jcc.21787.

[50] R. J. Gowers, M. Linke, J. Barnoud, T. J. E. Reddy, M. N. Melo, S. L. Seyler, D. L. Dotson, J. Domański, S. Buchoux, I. M. Kenney and O. Beckstein. 'MDAnalysis: A Python Package for the Rapid Analysis of Molecular Dynamics Simulations'. In: *Proceedings of the 15th Python in Science Conference*. Ed. by S. Benthall and S. Rostrup. Austin, Texas: SciPy, 2016, pp. 98–105. DOI: 10.25080/Majora-629e541a-00e.

[51] Y. Okamoto, S. Suzuki, H. Shiwaku, A. Ikeda-Ohno, T. Yaita and P. A. Madden. 'Local Coordination about La^{3+} in Molten $LaCl_3$ and Its Mixtures with Alkali Chlorides'. In: *The Journal of Physical Chemistry A* 114.13 (2010), pp. 4664–4671. DOI: 10.1021/jp910637p.

[52] A. A. Hagberg, D. A. Schult and P. J. Swart. 'Exploring Network Structure, Dynamics, and Function Using NetworkX'. In: *Proceedings of the 7th Python in Science Conference (SciPy 2008)*. Ed. by G. Varoquaux, T. Vaught and J. Millman. Pasadena, California, USA, Aug. 2008, pp. 11–15. DOI: 10.25080/TCWV9851.

[53] B. Borah, M. S. Emerson, S. Roy, J. J. Ferrari, K. W. Chapman, L. C. Gallington, D. Dhakal, E. M. Kim, P. W. Halstenberg, S. Dai, S. K. Gill, J. F. Wishart and C. J. Margulis. 'La^{3+} Networks and Speciation in the Molten State: Impact of Spacer Salt Selection on Structural Heterogeneity'. In: *Journal of the American Chemical Society* 148.12 (2026), pp. 12476–12480. DOI: 10.1021/jacs.5c22776.

[54] B. Li, S. Dai and D.-E. Jiang. 'First-Principles Molecular Dynamics Simulations of UCl_n–NaCl ($n = 3, 4$) Molten Salts'. In: *ACS Applied Energy Materials* 2.3 (2019), pp. 2122–2128. DOI: 10.1021/acsaem.8b02157.

[55] R. Kubo, M. Yokota and S. Nakajima. 'Statistical-Mechanical Theory of Irreversible Processes. II. Response to Thermal Disturbance'. In: *Journal of the Physical Society of Japan* 12.11 (1957), pp. 1203–1211. DOI: 10.1143/JPSJ.12.1203.

[56] Z. Fan, L. F. C. Pereira, H.-Q. Wang, J.-C. Zheng, D. Donadio and A. Harju. 'Force and Heat Current Formulas for Many-Body Potentials in Molecular Dynamics Simulations with Applications to Thermal Conductivity Calculations'. In: *Physical Review B* 92.9 (2015), p. 094301. DOI: 10.1103/PhysRevB.92.094301.

[57] B. Cheng and D. Frenkel. 'Computing the Heat Conductivity of Fluids from Density Fluctuations'. In: *Physical Review Letters* 125.13 (2020), p. 130602. DOI: 10.1103/PhysRevLett.125.130602.

[58] H. Flyvbjerg and H. G. Petersen. 'Error Estimates on Averages of Correlated Data'. In: *The Journal of Chemical Physics* 91.1 (1989), pp. 461–466. DOI: 10.1063/1.457480.

[59] A. Savitzky and M. J. E. Golay. 'Smoothing and Differentiation of Data by Simplified Least Squares Procedures'. In: *Analytical Chemistry* 36.8 (1964), pp. 1627–1639. DOI: 10.1021/ac60214a047.

[60] R. P. Futrelle and D. J. McGinty. 'Calculation of Spectra and Correlation Functions from Molecular Dynamics Data Using the Fast Fourier Transform'. In: *Chemical Physics Letters* 12.2 (1971), pp. 285–287. DOI: 10.1016/0009-2614(71)85065-0.

[61] L. de Sousa Oliveira and P. A. Greaney. 'Method to Manage Integration Error in the Green–Kubo Method'. In: *Physical Review E* 95.2 (2017), p. 023308. DOI: 10.1103/PhysRevE.95.023308.

[62] R. E. Jones and K. K. Mandadapu. 'Adaptive Green–Kubo Estimates of Transport Coefficients from Molecular Dynamics Based on Robust Error Analysis'. In: *The Journal of Chemical Physics* 136.15 (2012), p. 154102. DOI: 10.1063/1.3700344.

[63] L. Ercole, A. Marcolongo and S. Baroni. 'Accurate Thermal Conductivities from Optimally Short Molecular Dynamics Simulations'. In: *Scientific Reports* 7 (2017), p. 15835. DOI: 10.1038/s41598-017-15843-2.

[64] L. Ercole, R. Bertossa, S. Bisacchi and S. Baroni. 'SporTran: A Code to Estimate Transport Coefficients from the Cepstral Analysis of Multivariate Current Time Series'. In: *Computer Physics Communications* 280 (2022), p. 108470. DOI: 10.1016/j.cpc.2022.108470.

[65] A. Potapov and Y. Sato. 'Viscosity of Molten Rare Earth Metal Trichlorides II. Cerium Subgroup'. In: *Zeitschrift für Naturforschung A* 66 (2011), pp. 649–655. DOI: 10.5560/ZNA.2011-0016.

[66] N. T. H. ter Veer, D. C. Alders, A. L. Smith and R. J. M. Konings. 'Shear-Viscosity Results for Molten NaCl–UCl3 and NaCl–PuCl3 from Polarizable-Ion Molecular Dynamics'. Unpublished data supplied by N. T. H. ter Veer; $x(\mathrm{AnCl_3}) = 0.37$. 2026.

[67] B. N. Taylor and C. E. Kuyatt. *Guidelines for Evaluating and Expressing the Uncertainty of NIST Measurement Results*. Tech. rep. NIST Technical Note 1297. National Institute of Standards and Technology, 1993. DOI: 10.6028/NIST.TN.1297.

[68] N. Termini, A. Birri, B. Smith, R. Chesser, J. Numbers, K. Garland, E. Wilgocki, C. Gray and V. Glezakou. *FY24 Progress Report on Viscosity and Thermal Conductivity Measurements of Nuclear Industry Relevant Chloride Salts: An Experimental and Computational Study*. Tech. rep. ORNL/TM-2024/3650. Oak Ridge National Laboratory, 2024. DOI: 10.2172/2477502.

[69] O. Redlich and A. T. Kister. 'Algebraic Representation of Thermodynamic Properties and the Classification of Solutions'. In: *Industrial & Engineering Chemistry* 40.2 (1948), pp. 345–348. DOI: 10.1021/ie50458a036.

[70] C. M. Hurvich and C.-L. Tsai. 'Regression and Time Series Model Selection in Small Samples'. In: *Biometrika* 76.2 (1989), pp. 297–307. DOI: 10.1093/biomet/76.2.297.

[71] M. Stone. 'Cross-Validatory Choice and Assessment of Statistical Predictions'. In: *Journal of the Royal Statistical Society: Series B (Methodological)* 36.2 (1974), pp. 111–133. DOI: 10.1111/j.2517-6161.1974.tb00994.x.

[72] V. G. Goncharov, W. Smith, J. Li, J. A. Eakin, E. D. Reinhart, J. Boncella, L. D. Gibson, V. S. Bryantsev, R. Gong, S.-L. Shang, Z.-K. Liu, H. Xu, A. Clark and X. Guo. 'A Hybrid Calorimetry–Simulation Model of Mixing Enthalpy for Molten Salt'. In: *Communications Chemistry* 8.1, 300 (7th Oct. 2025). DOI: 10.1038/s42004-025-01688-8.

[73] D.-P. Tao. 'A New Model of Thermodynamics of Liquid Mixtures and Its Application to Liquid Alloys'. In: *Thermochimica Acta* 363.1–2 (2000), pp. 105–113. DOI: 10.1016/S0040-6031(00)00603-1.

[74] J. D. Chodera. 'A Simple Method for Automated Equilibration Detection in Molecular Simulations'. In: *Journal of Chemical Theory and Computation* 12.4 (2016), pp. 1799–1805. DOI: 10.1021/acs.jctc.5b00784.

[75] B. Efron. 'Bootstrap Methods: Another Look at the Jackknife'. In: *The Annals of Statistics* 7.1 (1979), pp. 1–26. DOI: 10.1214/aos/1176344552.

[76] A. Grossfield, P. N. Patrone, D. R. Roe, A. J. Schultz, D. Siderius and D. M. Zuckerman. 'Best Practices for Quantification of Uncertainty and Sampling Quality in Molecular Simulations [Article v1.0]'. In: *Living Journal of Computational Molecular Science* 1.1 (2018), p. 5067. DOI: 10.33011/livecoms.1.1.5067.

[77] NIST/SEMATECH. *NIST/SEMATECH e-Handbook of Statistical Methods*. National Institute of Standards and Technology. Accessed: 2026-07-31. 2012. URL: https://www.itl.nist.gov/div898/handbook/.

[78] E. J. Maginn, R. A. Messerly, D. J. Carlson, D. R. Roe and J. R. Elliot. 'Best Practices for Computing Transport Properties 1. Self-Diffusivity and Viscosity from Equilibrium Molecular Dynamics'. In: *Living Journal of Computational Molecular Science* 1.1 (2018), p. 6324. DOI: 10.33011/livecoms.1.1.6324.

[79] N. T. H. ter Veer, D. C. Alders, A. L. Smith and R. J. M. Konings. 'Structural Results for Molten NaCl–UCl3, NaCl–PuCl3 and NaCl–UCl3–PuCl3 from Polarizable-Ion Molecular Dynamics'. Unpublished data supplied by N. T. H. ter Veer. 2026.

[80] B. Li, S. Dai and D.-e. Jiang. 'Molecular Dynamics Simulations of Structural and Transport Properties of Molten NaCl–UCl3 Using the Polarizable-Ion Model'. In: *Journal of Molecular Liquids* 299 (2020), p. 112184. DOI: 10.1016/j.molliq.2019.112184.

[81] G. I. L. van Oudenaren, J. A. Ocádiz-Flores and A. L. Smith. 'Coupled Structural–Thermodynamic Modelling of the Molten Salt System NaCl–UCl3'. In: *Journal of Molecular Liquids* 342 (2021), p. 117470. DOI: 10.1016/j.molliq.2021.117470.

[82] G. Pireddu, A. Salcedo, H. Sauzet, S. Delpech, D. Lambertin and T. Kooyman. 'Polarizable Force Fields for the Structural and Thermophysical Properties of Molten Actinide Chlorides'. In: *Journal of Nuclear Materials* 612 (2025), p. 155822. DOI: 10.1016/j.jnucmat.2025.155822.

[83] M. C. Notarangelo, J. Tranchida, K. Goloviznina, M. Romanova, E. Bourasseau and M. Salanne. 'Atomistic Investigation of Thermophysical Properties of Actinide Chlorides-Based Molten Salts via Ab Initio Molecular Dynamics and the Polarizable Ion Model'. In: *The Journal of Physical Chemistry B* 130 (2026), pp. 814–828. DOI: 10.1021/acs.jpcb.5c06559.

[84] N. T. H. ter Veer, D. C. Alders, A. L. Smith and R. J. M. Konings. 'Thermal-Conductivity Results for Molten NaCl–UCl3 and NaCl–PuCl3 from Polarizable-Ion Molecular Dynamics'. Unpublished data supplied by N. T. H. ter Veer. 2026.

[85] A. H. Birri, R. C. Gallagher, C. Agca, J. W. McMurray and N. D. Bull Ezell. 'Application of the Redlich–Kister Expansion for Estimating the Density of Molten Fluoride Psuedo-Ternary Salt Systems of Nuclear Industry Interest'. In: *Chemical Engineering Science* 260 (2022), p. 117954. DOI: 10.1016/j.ces.2022.117954.

[86] M. A. Rose, L. D. Gardner, T. T. Lichtenstein, S. A. Thomas and E. Wu. *Property Measurements of NaCl–UCl3 and NaCl–KCl–UCl3 Molten Salts*. Tech. rep. ANL/CFCT-22/45 Rev. 1. Argonne, Illinois, USA: Argonne National Laboratory, 26th May 2023. DOI: 10.2172/1985295.

[87] N. Termini, A. Birri, S. Henderson and N. D. B. Ezell. *An Overview of the Molten Salt Thermal Properties Database–Thermophysical, Version 2.1.1 (MSTDB-TP v.2.1.1)*. Tech. rep. ORNL/TM-2023/2955. Oak Ridge, Tennessee, USA: Oak Ridge National Laboratory, July 2023. DOI: 10.2172/1988348.

[88] A. E. Gheribi, A. T. Phan, H. Yang, R. C. Gallagher and P. Chartrand. 'The Role of the Local Structure on the Thermal Transport within Dissociated and Complexed Molten Salt Mixtures'. In: *Journal of Molecular Liquids* 408 (2024), p. 125239. DOI: 10.1016/j.molliq.2024.125239.

[89] K. O. Bobrova and V. N. Dokytovich. 'Thermal Conductivity of CeCl3–MCl (M = Li, Na, K, Cs) Molten Mixtures'. In: *Russian Metallurgy (Metally)* 2023.8 (2023), pp. 1018–1024. DOI: 10.1134/S0036029523080037.

[90] C. D. Chliatzou, M. J. Assael, K. D. Antoniadis, M. L. Huber and W. A. Wakeham. 'Reference Correlations for the Thermal Conductivity of 13 Inorganic Molten Salts'. In: *Journal of Physical and Chemical Reference Data* 47.3 (2018), p. 033104. DOI: 10.1063/1.5052343.

A

Supplementary Simulation Information

A.1 Supporting Structural Results

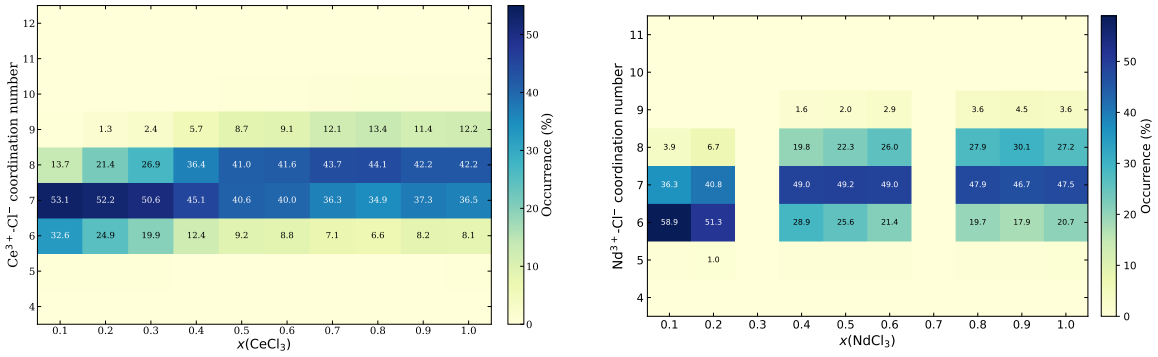

(a) $NaCl - CeCl_3$.

(b) $NaCl - NdCl_3$.

Figure A.1. Binary metal–chloride coordination-number distributions at 1100 K. Cell values denote percentage occurrence.

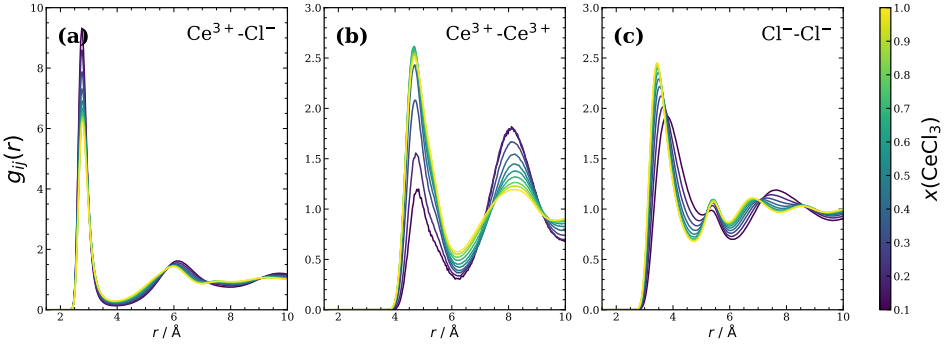

(a) $NaCl - CeCl_3$.

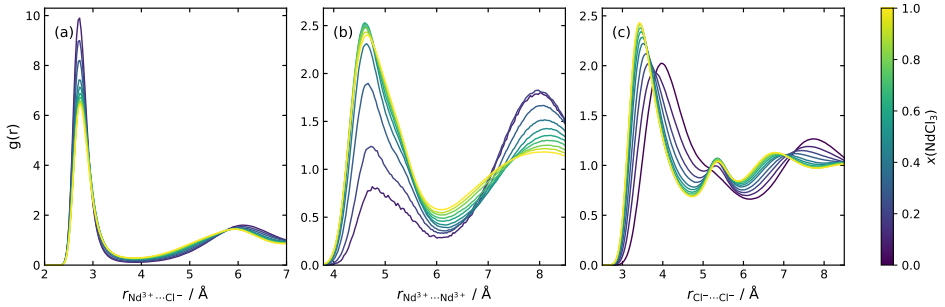

(b) $NaCl - NdCl_3$.

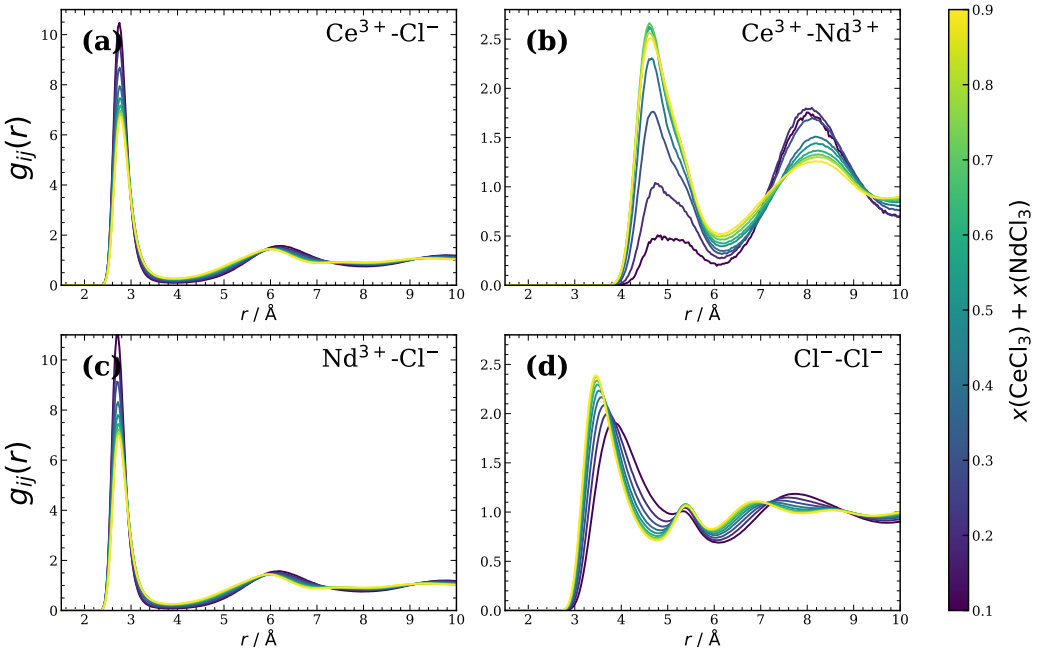

(c) Equal-Ce/Nd $NaCl - CeCl_3 - NdCl_3$ path.

Figure A.2. Supporting composition-dependent RDFs at 900 K. These low- temperature results provide the structural extreme complementary to the 1100 K comparison in the main text.

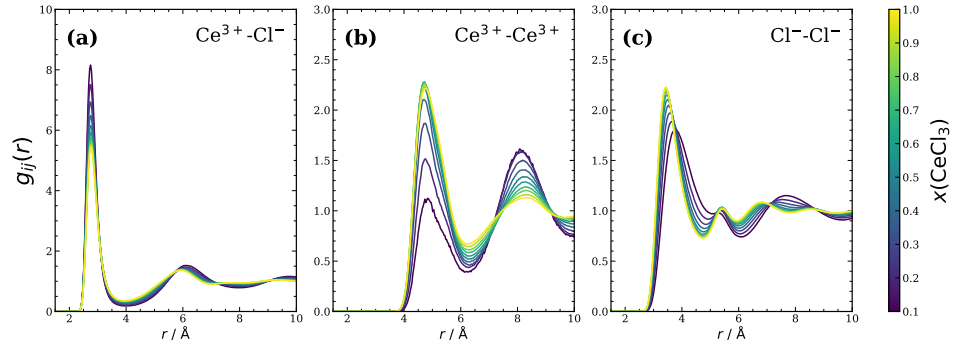

(a) NaCl – $CeCl_3$.

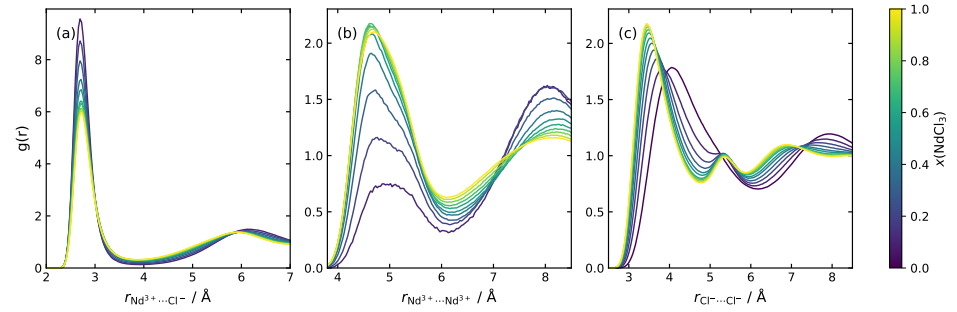

(b) NaCl – $NdCl_3$.

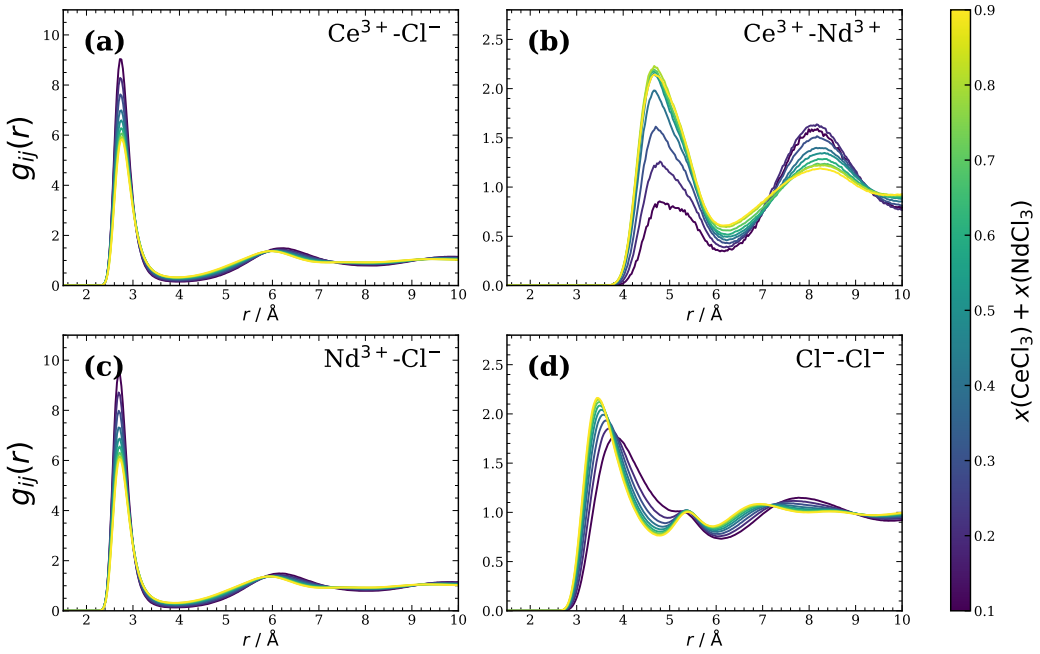

(c) Equal-Ce/Nd NaCl – $CeCl_3$ – $NdCl_3$ path.

Figure A.3. Supporting composition-dependent RDFs at 1200 K. Together with Figure A.2, these data show the low- and high-temperature structural limits of the investigated range.

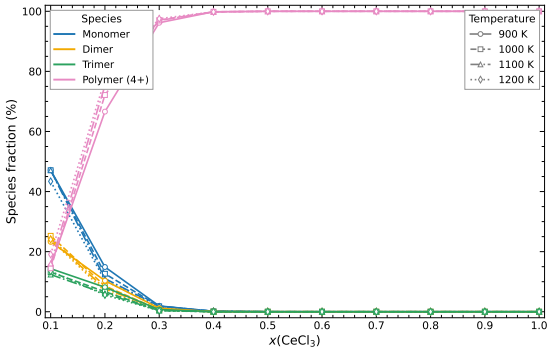

(a) $NaCl - CeCl_3$ cluster speciation.

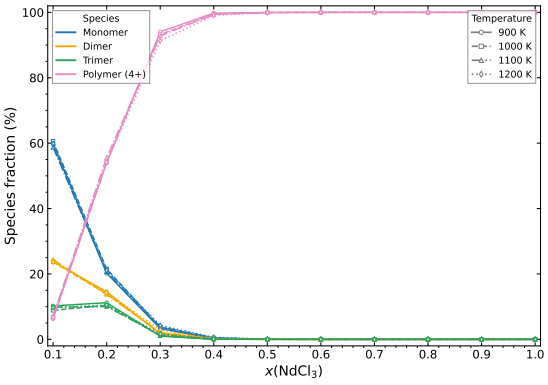

(b) $NaCl - NdCl_3$ cluster speciation.

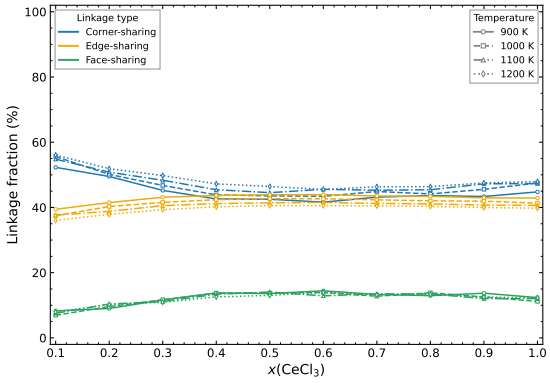

(c) $NaCl - CeCl_3$ linkage fractions.

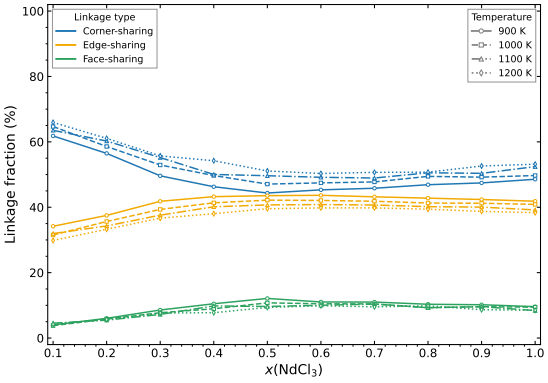

(d) $NaCl - NdCl_3$ linkage fractions.

Figure A.4. Supporting binary cluster-size and shared-chloride connectivity results over 900–1200 K.

A.2 NPT Window and Volume-Property Verification

The density, molar-volume and excess-molar-volume datasets were all calculated from defined late-time portions of the NPT trajectories. The workflows were developed at different stages of the project, so the verification was matched to the analysis actually used rather than rewritten as an artificially identical procedure. This preserves the methodological sequence of an initial operational choice followed by progressively stronger statistical diagnostics.

Table A.1. Verified production-window and uncertainty treatment for density, molar volume and excess molar volume.

System	Production interval	State-point assessment	Excess-volume representation
NaCl – $NdCl_3$	State-specific retained start, constrained to leave at least 250 ps	Statistical inefficiency, effective sample size, residual-trend, alternative-cutoff, split-half and block checks; all 44 states passed	Shared-endpoint covariance propagated to GLS; order checked with AICc and leave-one-composition-out prediction
NaCl – $CeCl_3$	First 1000 saved box records removed uniformly	Direct instantaneous-density averaging and reported trajectory variability over the prescribed common interval	Predefined three-coefficient unweighted Redlich–Kister description
Equal-Ce/Nd ternary path	First 10% removed uniformly	Mean volume and density evaluated over the prescribed common interval; conventional state-point standard error retained	Fixed-order ordinary-least-squares binary descriptions with symmetric Muggianu interpolation

For the Nd workflow, density was evaluated as the direct mean of $m_{\mathrm{cell}}/V(t)$, and molar volume as the direct mean of $N_{\mathrm{A}}V(t)/N_{\mathrm{salt}}$ over the same retained samples. The independent reconstruction M_{mix}/ρ differed from the direct molar-volume average by at most 0.0096%, providing a numerical consistency check. The state-point standard error used for inverse-variance weighting was $s_j = \max(s_{\mathrm{ACF}}, s_{\mathrm{block}})$.

For the Ce and ternary workflows, fixed family-wide windows were applied to all temperatures and compositions. These analyses do not claim the full state-specific correlation-aware diagnostic suite used for Nd; instead, the uniform rule prevents post hoc selection of favourable regions and records the uncertainty estimator actually used by each verified notebook. Consequently, all three datasets are statistically assessed, while the depth of the assessment is reported transparently.

A.3 Heat-Capacity Window Verification

The retained enthalpy interval was selected separately for each simulation family because the archived time series and the observed equilibration behaviour differed. Ordinary least squares using production-average temperatures was the primary estimator. Inverse-variance weighted fits, nominal thermostat temperatures, quadratic fits and leave-one-temperature-out linear fits were used only as sensitivity diagnostics.

Table A.2. Heat-capacity production windows and the evidence supporting their use.

System	Retained interval	Verification
$NaCl - CeCl_3$	Final 50%	All 44 states passed the final-window checks; the largest shift between final-50% and final-60% estimates was 0.999 combined standard errors
$NaCl - NdCl_3$	Final 60%	Candidate retained fractions of 40, 50, 60 and 70% were examined; final 60% was the earliest common interval for which all 44 states satisfied the adopted checks
Equal-Ce/Nd ternary path	Final 60%	Compared with final 50% and an automatic correlation-aware retained start; maximum shifts were 0.903 reference standard errors and 1.637 automatic-window standard errors, with none exceeding two

The ternary archive did not contain a separate temperature time series. Production-average temperatures were therefore reconstructed from the saved kinetic energy using the same degrees-of-freedom convention throughout the analysis. This distinction is retained explicitly because nominal thermostat temperatures and realised production-average temperatures are not identical statistical inputs.

A.4 Thermal-Conductivity Sensitivity Verification

The structural-coherence workflow was initially established for NaCl – $CeCl_3$ using a uniform 20% discard. The final binary workflow applied the same operational choice to all 44 Ce and all 44 Nd state points, leaving 8001 of 10001 saved NPT records per state. As the analysis was extended to NaCl – $NdCl_3$ and the equal-Ce/Nd ternary path, the workflow was refined by repeating the thermophysical post-processing after discarding 10, 20, 30 and 40% of each trajectory and by testing 4, 5, 8 and 10 contiguous blocks for the fluctuation-derived isothermal compressibility.

Table A.3. Maximum relative variation of selected thermal-conductivity inputs across the tested discard fractions, measured relative to the primary 20% result.

Quantity	Ternary maximum	NaCl – $NdCl_3$ maximum
Density	0.114%	0.162%
Molar volume	0.114%	0.162%
C_p	0.357%	0.314%
α_V	1.47%	1.97%
v_s	6.30%	9.90%
κ_T	12.23%	15.28%

The small changes in density, molar volume, heat capacity and thermal expansion show that the main thermophysical trends are insensitive to the precise retained fraction. The larger response of κ_T and the derived sound speed is expected for a fluctuation-based estimator and was retained as a diagnostic rather than hidden. The full 10–40% numerical comparison was performed for the Nd and ternary workflows; the Ce workflow is described as the initial operational application of the common 20% convention and is not assigned sensitivity values that were not separately calculated.

The RDF contribution was also tested using the unsmoothed distributions and Savitzky–Golay windows of 11, 21 and 31 points. The maximum range in the composition-weighted coherence length was approximately 3.00% for the ternary system and 5.97% for NaCl – $NdCl_3$. These checks confirm that the reported structural-coherence trends do not arise from one arbitrary smoothing window. As a scale reference for the main-text interpretation, the pure-NaCl endpoint has a coherence length of about 6 Å in this workflow, whereas the intermediate binary region is typically about 2.8–3.0 Å and the investigated equal-Ce/Nd ternary states remain within approximately 2.68–2.94 Å. This comparison is used only to illustrate the magnitude of the coherence loss; it is not an independent validation of the SCM transport coefficient.

A.5 Supporting Viscosity Analyses

A.5.1 Five-Nanosecond NaCl – $NdCl_3$ Convergence Diagnostics

The final NaCl – $NdCl_3$ production dataset contains 44 state points over 900, 1000, 1100 and 1200 K. The primary viscosity estimate at each state is the complete 5 ns SporTran result at $\mathrm{TSKIP} = 12$. Convergence was assessed using cumulative 3, 4 and 5 ns estimates at $\mathrm{TSKIP} = 11$, 12 and 13, followed by shifted-window diagnostics for states requiring additional checks. The resulting classification contains 40 reportable states and four Review states: 900 K at $x(\mathrm{NdCl_3}) = 0.30$ and 0.90, 1000 K at $x(\mathrm{NdCl_3}) = 0.70$, and 1100 K at $x(\mathrm{NdCl_3}) = 1.00$.

The corrected 1000 K slice was independently processed using the same methodology. All 11 state points completed, all 99 trajectory-length/TSKIP calculations passed numerically, and all 33 independently recomputed 5 ns values reproduced the preceding dense-scan results. Six states then underwent targeted shifted-window analysis using the 0–3, 1–4, 2–5, 0–4 and 1–5 ns windows at $\mathrm{TSKIP} = 11$, 12 and 13. All 90 calculations completed and all 36 prefix-reproduction checks passed. The $x(\mathrm{NdCl_3}) = 0.60$ state was confirmed stable, while $x(\mathrm{NdCl_3}) = 0.70$ retained a 16.1% controlling window-sensitivity metric and therefore remains non-converged. The remaining sensitivity-checked states are retained as reportable with their detailed classification recorded in the table below.

Table A.4. NaCl–$NdCl_3$ 5 ns viscosity values and reporting status over the complete 900–1200 K dataset. Pass and Caution states are reportable; Review states are retained as non-converged provisional values.

T / K	$x(\mathrm{NdCl_3})$	η / mPa s	$u(\eta)$ / mPa s	Status
900	0.0	1.513	0.028	Pass
900	0.1	1.855	0.042	Pass
900	0.2	2.552	0.072	Pass
900	0.3	3.606	0.130	Review
900	0.4	3.695	0.112	Pass
900	0.5	3.981	0.116	Caution
900	0.6	5.314	0.193	Caution
900	0.7	6.597	0.250	Pass
900	0.8	6.439	0.225	Caution
900	0.9	8.358	0.336	Review
900	1.0	9.113	0.367	Pass
1000	0.0	1.387	0.029	Pass
1000	0.1	1.760	0.038	Pass
1000	0.2	2.214	0.057	Caution
1000	0.3	2.532	0.065	Pass
1000	0.4	3.160	0.094	Pass
1000	0.5	3.655	0.100	Caution
1000	0.6	4.021	0.113	Pass
1000	0.7	4.917	0.158	Review

Continued on next page

Table A.4. NaCl–$NdCl_3$ 5 ns viscosity values and reporting status over the complete 900–1200 K dataset. Pass and Caution states are reportable; Review states are retained as non-converged provisional values. (continued)

T / K	$x(NdCl_3)$	η / mPa s	$u(\eta)$ / mPa s	Status
1000	0.8	5.517	0.177	Pass
1000	0.9	5.721	0.206	Caution
1000	1.0	5.909	0.207	Caution
1100	0.0	1.151	0.022	Pass
1100	0.1	1.418	0.029	Pass
1100	0.2	1.729	0.039	Pass
1100	0.3	2.119	0.053	Pass
1100	0.4	2.366	0.066	Pass
1100	0.5	2.603	0.064	Pass
1100	0.6	2.914	0.076	Pass
1100	0.7	3.404	0.111	Pass
1100	0.8	3.862	0.113	Pass
1100	0.9	3.799	0.096	Pass
1100	1.0	4.324	0.128	Review
1200	0.0	0.923	0.017	Pass
1200	0.1	1.052	0.018	Pass
1200	0.2	1.394	0.029	Pass
1200	0.3	1.539	0.032	Pass
1200	0.4	1.878	0.044	Pass
1200	0.5	1.808	0.040	Pass
1200	0.6	2.429	0.064	Pass
1200	0.7	2.353	0.053	Pass
1200	0.8	2.717	0.066	Pass
1200	0.9	3.165	0.089	Pass
1200	1.0	3.350	0.101	Pass

A.5.2 NaCl–$NdCl_3$ Temporal-Persistence Verification at 900 K

A dedicated temporal analysis was performed for the five Nd-rich compositions $x(NdCl_3) = 0.60$–1.00 at 900 K. Each exact 5 ns trajectory was evaluated over nine sequential, non-overlapping 0.5 ns windows spanning 0.2–4.7 ns. The primary persistence metrics and topology populations are listed in Table A.5. Values are means across the nine windows; the windows are blocks of one trajectory and are not independent replicas.

Table A.5. Composition-resolved 900 K NaCl – $NdCl_3$ temporal-persistence results. Persistence values are $1/e$ times in ps. The topology-switching rate is in $\mathrm{ps}^{-1}\,\mathrm{Nd}^{-1}$. Corner, edge and face columns are percentages among linked Nd–Nd pairs.

$x(\mathrm{NdCl_3})$	Nd–Cl cont.	Nd–Cl int.	Nd–Nd cont.	Nd–Nd int.	Switch rate	Corner / %	Edge / %	Face / %
0.60	14.404	54.081	14.944	79.190	4.255	45.883	43.792	10.325
0.70	14.635	59.476	16.069	93.127	4.909	46.161	43.419	10.420
0.80	14.596	63.592	16.176	102.800	5.274	47.369	42.986	9.645
0.90	15.498	68.306	16.979	108.151	5.788	47.811	42.562	9.627
1.00	15.543	71.290	16.616	115.493	6.079	48.977	42.032	8.991

All continuous and intermittent $1/e$ crossings were reached within the 250 ps maximum lag. The uninterrupted Nd–Cl and any-link Nd–Nd persistence increase by approximately 7.9% and 11.2% between $x = 0.60$ and 1.00, respectively, whereas the corresponding intermittent increases are approximately 31.8% and 45.8%. The topology-switching rate simultaneously increases by approximately 42.9%. These trends support an increasingly recurrent but dynamically labile Nd-centred network.

All 225 continuous persistence integrals reached the adopted convergence condition, whereas only 46 of the 225 intermittent integrals did so within 250 ps; the remaining 179 are finite-lag partial integrals. The main Results discussion therefore uses the fully reached $1/e$ persistence times rather than treating the partial integrals as infinite-time lifetimes. The window-resolved mean Nd–Cl coordination numbers also differ from the accepted RDF reference by approximately 0.15–0.19 at every composition; these temporal CN values are therefore not used as an independent absolute coordination benchmark.

A.5.3 Five-Nanosecond NaCl – $CeCl_3$ Convergence and Temporal-Persistence Coverage

The complete NaCl – $CeCl_3$ viscosity dataset contains 44 state points, of which 42 are reportable. The two Review states exhibit different forms of residual sensitivity. At 1000 K and $x(CeCl_3) = 0.50$, the complete 5 ns estimate increases markedly relative to the shorter trajectory prefixes. At 1100 K and $x(CeCl_3) = 0.40$, the complete trajectory is locally spectral-cutoff stable but the long contiguous windows are not mutually consistent.

Table A.6. NaCl–$CeCl_3$ 5 ns viscosity values and reporting status. Pass and Caution states are reportable; Review states are retained as non-converged provisional values.

T / K	$x(CeCl_3)$	η / mPa s	$u(\eta)$ / mPa s	Status
900	0.0	2.180	0.055	Pass
900	0.1	2.516	0.061	Pass
900	0.2	3.434	0.106	Caution
900	0.3	4.847	0.184	Caution
900	0.4	5.325	0.173	Pass
900	0.5	6.749	0.240	Pass
900	0.6	8.527	0.338	Pass
900	0.7	7.868	0.295	Caution
900	0.8	8.137	0.277	Pass
900	0.9	9.830	0.390	Caution
900	1.0	9.188	0.332	Pass
1000	0.0	1.461	0.031	Pass
1000	0.1	1.897	0.042	Pass
1000	0.2	2.427	0.065	Pass
1000	0.3	2.964	0.089	Caution
1000	0.4	3.301	0.095	Pass

Continued on next page

Table A.6. NaCl–$CeCl_3$ 5 ns viscosity values and reporting status. Pass and Caution states are reportable; Review states are retained as non-converged provisional values. (continued)

T / K	$x(CeCl_3)$	η / mPa s	$u(\eta)$ / mPa s	Status
1000	0.5	4.291	0.147	Review
1000	0.6	4.191	0.119	Pass
1000	0.7	4.965	0.161	Pass
1000	0.8	5.857	0.185	Pass
1000	0.9	5.896	0.204	Caution
1000	1.0	6.001	0.193	Pass
1100	0.0	1.141	0.019	Pass
1100	0.1	1.359	0.025	Pass
1100	0.2	1.662	0.039	Pass
1100	0.3	2.038	0.053	Pass
1100	0.4	2.401	0.058	Review
1100	0.5	2.802	0.072	Pass
1100	0.6	3.112	0.092	Pass
1100	0.7	3.392	0.095	Pass
1100	0.8	3.636	0.091	Pass
1100	0.9	4.054	0.131	Caution
1100	1.0	3.847	0.107	Pass
1200	0.0	0.911	0.014	Pass
1200	0.1	1.160	0.027	Caution
1200	0.2	1.413	0.035	Caution
1200	0.3	1.549	0.035	Pass
1200	0.4	1.817	0.040	Caution
1200	0.5	2.081	0.049	Pass
1200	0.6	2.309	0.059	Pass
1200	0.7	2.365	0.053	Pass
1200	0.8	2.860	0.073	Pass
1200	0.9	2.917	0.072	Pass
1200	1.0	3.068	0.076	Pass

The Ce-rich temporal analysis covers $x(CeCl_3) = 0.60$–1.00 at 900 K using sequential 0.5 ns windows from the 5 ns trajectories. Continuous Ce–Cl contact persistence lies between approximately 13.6 and 14.7 ps, while continuous Ce–Ce shared-chloride linkage persistence lies between approximately 15.1 and 17.1 ps. The composition dependence is not monotonic, which supports use of these quantities as dynamical descriptors rather than as a single-parameter explanation of viscosity. The main-text persistence figure reports the across-window means and within-trajectory variability.

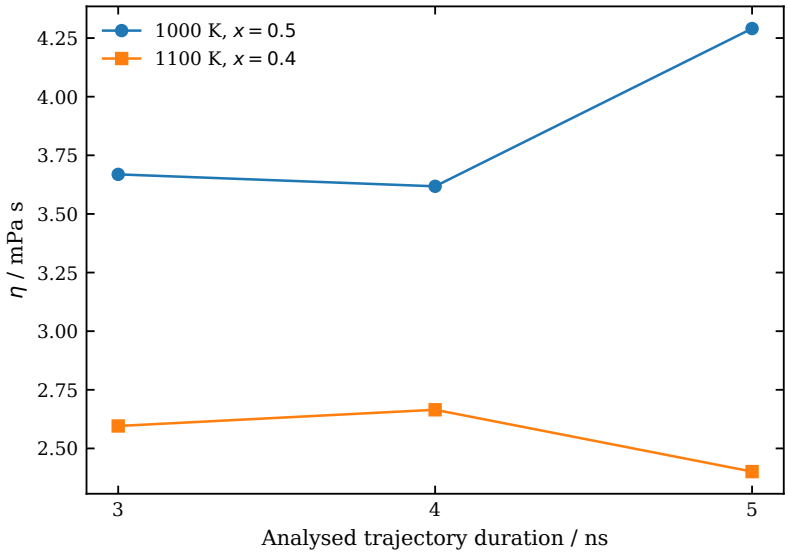

Figure A.5. Viscosity estimates obtained from the first 3, 4 and 5 ns of the two NaCl – $CeCl_3$ trajectories classified as Review. The values are retained as provisional estimates but are not treated as converged results.

A.5.4 Five-Nanosecond Ternary Viscosity and Persistence Coverage

The ternary viscosity table uses $x(\mathrm{LnCl_3}) = x(\mathrm{CeCl_3}) + x(\mathrm{NdCl_3})$ along the equal-Ce/Nd path. The four Caution states are convergence-acceptable but retain moderate finite-trajectory sensitivity. The two 900 K Review states are provisional.

Table A.7. NaCl–$CeCl_3$–$NdCl_3$ 5 ns viscosity values along the equal-Ce/Nd path. Pass and Caution states are reportable; Review states are retained as non-converged provisional values.

T / K	$x(\mathrm{NaCl})$	$x(\mathrm{CeCl_3})$	$x(\mathrm{NdCl_3})$	η / mPa s	$u(\eta)$ / mPa s	Status
900	0.90	0.05	0.05	2.560	0.068	Pass
900	0.80	0.10	0.10	3.277	0.093	Pass
900	0.70	0.15	0.15	3.997	0.122	Pass
900	0.60	0.20	0.20	5.101	0.167	Pass
900	0.50	0.25	0.25	6.353	0.247	Review
900	0.40	0.30	0.30	6.548	0.225	Pass
900	0.30	0.35	0.35	9.421	0.385	Pass
900	0.20	0.40	0.40	8.533	0.321	Review
900	0.10	0.45	0.45	9.045	0.329	Pass
1000	0.90	0.05	0.05	1.777	0.038	Pass
1000	0.80	0.10	0.10	2.266	0.057	Pass
1000	0.70	0.15	0.15	2.969	0.087	Pass
1000	0.60	0.20	0.20	3.224	0.089	Pass
1000	0.50	0.25	0.25	3.830	0.118	Pass
1000	0.40	0.30	0.30	4.407	0.134	Pass
1000	0.30	0.35	0.35	4.768	0.151	Caution

Continued on next page

Table A.7. NaCl–$CeCl_3$–$NdCl_3$ 5 ns viscosity values along the equal-Ce/Nd path. Pass and Caution states are reportable; Review states are retained as non-converged provisional values. (continued)

T / K	$x(\mathrm{NaCl})$	$x(\mathrm{CeCl_3})$	$x(\mathrm{NdCl_3})$	η / mPa s	$u(\eta)$ / mPa s	Status
1000	0.20	0.40	0.40	5.378	0.169	Pass
1000	0.10	0.45	0.45	5.550	0.180	Pass
1100	0.90	0.05	0.05	1.390	0.027	Pass
1100	0.80	0.10	0.10	1.621	0.037	Pass
1100	0.70	0.15	0.15	1.957	0.043	Pass
1100	0.60	0.20	0.20	2.341	0.064	Caution
1100	0.50	0.25	0.25	2.749	0.077	Caution
1100	0.40	0.30	0.30	3.006	0.077	Pass
1100	0.30	0.35	0.35	3.117	0.083	Pass
1100	0.20	0.40	0.40	3.565	0.095	Pass
1100	0.10	0.45	0.45	3.978	0.115	Pass
1200	0.90	0.05	0.05	1.115	0.022	Pass
1200	0.80	0.10	0.10	1.331	0.032	Pass
1200	0.70	0.15	0.15	1.483	0.028	Pass
1200	0.60	0.20	0.20	1.787	0.043	Pass
1200	0.50	0.25	0.25	1.933	0.040	Pass
1200	0.40	0.30	0.30	2.292	0.057	Pass
1200	0.30	0.35	0.35	2.435	0.054	Caution
1200	0.20	0.40	0.40	2.594	0.058	Pass
1200	0.10	0.45	0.45	3.169	0.086	Pass

The final temporal-persistence analysis covers 900 and 1000 K for $x(\mathrm{LnCl_3}) = 0.40$–0.90. Each trajectory contains 1001 saved frames with a frame spacing of approximately 5 ps. Temporal stability was assessed using five non-overlapping 1 ns blocks, with persistence functions integrated to a maximum lag of 500 ps. Continuous and intermittent Ce–Cl–Ce, Ce–Cl–Nd and Nd–Cl–Nd bridge persistence were evaluated using the accepted first-shell distance definitions. Continuous persistence is continuous at the saved-frame resolution; a short break and reformation between adjacent 5 ps frames cannot be detected. The five blocks belong to one trajectory and are not independent replicas.

The final analysis shows smooth composition dependence at both temperatures, with no composition-specific temporal anomaly at $x(\mathrm{LnCl_3}) = 0.80$ and no exceptional stabilisation of the mixed Ce–Cl–Nd bridge relative to the two like-cation bridge classes. Finite-window integrals are therefore reported, where used, as integrated persistence times rather than complete infinite-time lifetimes. These conclusions are used as association-level structural evidence and not as proof of a unique causal mechanism for viscosity.